Title
Optogenetic Dissection of Cell Types and Circuits in Mouse Visual Cortex

Permalink
https://escholarship.org/uc/item/8gr6f25z

Author
Kyubwa, Espoir Magu

Publication Date
2016

Peer reviewed|Thesis/dissertation

UNIVERSITY OF CALIFORNIA, SAN DIEGO

Optogenetic dissection of cell types and circuits in mouse visual cortex

A dissertation submitted in partial satisfaction of the requirements for the degree of
Doctor of Philosophy

in

Bioengineering

by

Espoir Magu Kyubwa

Committee in charge:

      Professor Gert Cauwenberghs, Chair
      Professor Edward M. Callaway, Co-Chair
      Professor Todd P. Coleman
      Professor David Kleinfeld
      Professor Gabriel A. Silva

2016

The Dissertation of Espoir Magu Kyubwa is approved, and it is acceptable in quality and form for publication on microfilm and electronically:

_____

_____

_____

_____
Co-Chair

_____
Chair

University of California, San Diego

2016

DEDICATION

YA TATE
Masuzo Adolphine Kyubwa
November 11, 1946 – April 19, 2014

ASANTE KWA KUNIONESHA THAMANI YA ELIMU
KONGWA BWENENE
Thank you for being my inspiration

TABLE OF CONTENTS

LIST OF FIGURES

LIST OF TABLES

ACKNOWLEDGEMENTS

I would also like to thank my wife Esther for her love and support. She has suspended her studies to raise our son Emmanuel during the last six months. To my brother Amani, thank you for being my best friend. I would like to thank my parents; Delphin and Bitisho, for nurturing my scientific curiosity at an early age and for encouraging me to set higher goals at every step of my academic career. A special thank you to my late grandmother and first teacher, Adolphine, for introducing me to academia and allowing me to shadow her in her science classrooms in Butole, Zaire. Her passion for teaching and mentoring others was contagious.

Chapter 2, in full, is a manuscript in preparation as: Espoir M. Kyubwa, and Edward M. Callaway. "Intrinsic properties and local connectivity of vasoactive intestinal peptide expressing inhibitory interneuron subtypes in mouse visual cortex" The dissertation author is the principle author of the paper.

Appendix A in full is an article published in *Neuron* (December 2015), Kim Euiseok J., Ashley L. Juavinett, Espoir M. Kyubwa, Matthew W. Jacobs, and Edward M. Callaway. 2015. "Three Types of Cortical Layer 5 Neurons That Differ in Brain-

Wide Connectivity and Function." *Neuron* 88 (6): 1253–67. The dissertation author was the third author of this work. The dissertation author performed all *in vitro* electrophysiology experiments and analysis and wrote portion of the manuscript concerning *in vitro* electrophysiology. The full article and supplemental materials are included in Appendix A for completeness. *In vitro* electrophysiology data are shown in Figure A.2(C, D), Figure SA.3 and Table SA.1 (Kim et al. 2015; Appendix A).

VITA

2018   M.D., expected, School of Medicine
                    University of California, San Diego, CA

2016   Ph.D., Bioengineering
                    University of California, San Diego, CA

2009   B.S., Bioengineering: Pre-medical
                    University of California, San Diego, CA

AWARDS

Howard Hughes Medical Institute, Gilliam Fellowship for Advanced Study, 2010-16
Kavli Institute for Brain and Mind, Innovative Research Grant, 2015

PUBLICATIONS

Euiseok J. Kim, Ashley L. Juavinett, **Espoir M. Kyubwa**, Matthew W. Jacobs and Edward M. Callaway. Genetic Targeting Reveals Three Types of Cortical L5 Neurons that Differ in Brain-Wide Connectivity and Function**.** Neuron. 2015 December 2015.

Hwang J, **Kyubwa EM,** Bae WC, Bugbee WD, Masuda K, Sah RL: *In vitro* calcification of immature bovine articular cartilage: formation of a functional zone of calcified cartilage. *Cartilage* Cartilage. 2010 Oct; 1(4): 287–297.

Abstracts for presentation
Espoir M. Kyubwa, Josh Z. Huang, Edward M. Callaway. Connectivity of Vasoactive Intestinal Peptide expressing inhibitory interneuron in mouse visual cortex. Program No. 598.02. Neuroscience 2015 Abstracts. Chicago IL: Society for Neuroscience, 2015.

Kyubwa EM, Hwang J, Chen AC, Sah RL: Maturation-associated increase in the intrinsic fracture toughness of the osteochondral interface. *Trans Orthop Res Soc* 35:1727, 2010.

FIELDS OF STUDY

Major Field of Study: Bioengineering (Computational Neuroscience)

        Studies in Systems Neuroscience
        Professor Edward M. Callaway

        Studies in Computational Neuroscience
        Professor Gert Cauwenberghs, David Kleinfeld, and Gabriel Silva

ABSTRACT OF THE DISSERTATION

Optogenetic dissection of cell types and circuits in mouse visual cortex

by

Espoir Magu Kyubwa

Doctor of Philosophy in Bioengineering

University of California, San Diego, 2016

Professor Gert Cauwenberghs, Chair
Professor Edward Callaway, Co-Chair

While many observations make it clear that cell types and specificity of connections matter, we still lack a mechanistic understanding of how cell types and their specific pattern of connectivity might contribute uniquely to cortical computations. To understand the contributions of cell types and circuits in mouse visual cortex we have taken advantage of multi-feature Boolean logical expression of

light sensitive cationic channel (channelrhodopsin-ChR2) and whole cell dual patch recordings in living brain slices. Using these tools, we have identified unique electrophysiology and connectivity patterns of vasoactive intestinal peptide (VIP) expressing interneuron subtypes (Chapter 2). We have also introduced methods that will enable single cell resolution mapping of inhibitory inputs in the future (Chapter 3). Finally in Appendix A, we identified three layer 5 pyramidal cell types in mouse visual cortex based on intrinsic electrophysiology, visual responses, and long range connectivity. Better understanding of highly specific cell types and circuits in mouse models will help us better classify and treat psychiatric disorders in humans where inhibitory circuit dysfunctions have been implicated.

CHAPTER 1:

Introduction

One of the challenges of understanding the function of the brain is the enormous complexity and diversity by which the brain implements cell types and circuits for specialized function and behavior. Although inhibitory GABAergic interneurons only account for 20% of all cortical neurons, they play a major role in increasing the computational power of cortical circuits (Tamamaki et al. 2003; Wilson et al. 2012). Understanding the connectivity and function of inhibitory cortical neurons is central to obtaining a mechanistic understanding of how cortical microcircuits interact to generate perception and behavior. Studies have identified dozens of distinct inhibitory cell types, each with unique morphology, chemical properties, intrinsic electrophysiological properties, and connection specificity (Kawaguchi and Kubota 1997; Kawaguchi and Kondo 2002; Yoshimura and Callaway 2005; Xu et al. 2006; DeFelipe et al. 2013; Pfeffer et al. 2013; Jiang et al. 2015). Untangling the complex yet specialized function and connectivity of these diverse cortical inhibitory cells has been the focus of intense research for the past three decades.

In addition, there is growing evidence from animal models and human studies implicating inhibitory circuit dysfunction in psychiatric diseases such as autism and schizophrenia (Curley and Lewis 2012; Zikopoulos and Barbas 2013; Lewis 2014). In the face of this evidence, National Institute of Mental Health (NIMH) has begun to classify psychiatric disorders based on cell type and circuit dysfunction in the new Research Domain Criteria (RDoC) diagnostic system rather than using symptomology classification in the Diagnostic and Statistical Manual of Mental Disorders (DSM) (T.

Insel et al. 2010; T. R. Insel and Cuthbert 2015; Kozak and Cuthbert 2016). The major body of work presented in this dissertation takes advantage of newly emerging intersectional optogenetic tools to study cell type specific connectivity with fine genetic specificity.

Classification of inhibitory cell type

Cell types can be classified based on molecular marker expression, discharge properties, or axonic/dendritic arborization pattern. Classification based on expression of molecular markers, has provided the strongest tool in which genetic approaches may be used to investigate cell type specific circuits (Luo et al. 2008; Huang 2014; Taniguchi 2014). Three non-overlapping molecular markers parvalbumin (PV), somatostatin (SOM), and serotonin receptor 5H-hydroxyltryptamine 3a (5HT3aR) have been found to account for 100 % of all cortical interneurons (Xu et al. 2010; Rudy et al. 2011) (Figure 1.1).

The most common group of inhibitory cells (PV+), which accounts for 40% of interneurons, can be subdivided into basket cells and chandelier cells based on axonal arborization pattern (Figure 1.2). Basket cells innervate soma and proximal dendrites of excitatory neurons while chandelier cells contact the initial segments providing strong shutting inhibition to postsynaptic cells. Cortical SOM+ cells, which account for 30% of all interneurons, are more heterogeneous in their morphology and discharge properties than PV+ interneurons (Wang et al. 2004; Ma et al. 2006). X98 SOM+ cells extend their axons to layer 1 innervating distal dendrites and fire low-threshold calcium spikes. While X94 SOM+ cells innervate layer 4 cells and discharge quasi-fast spiking stuttering action potentials (Ma et al. 2006; H. Xu et al. 2013). The
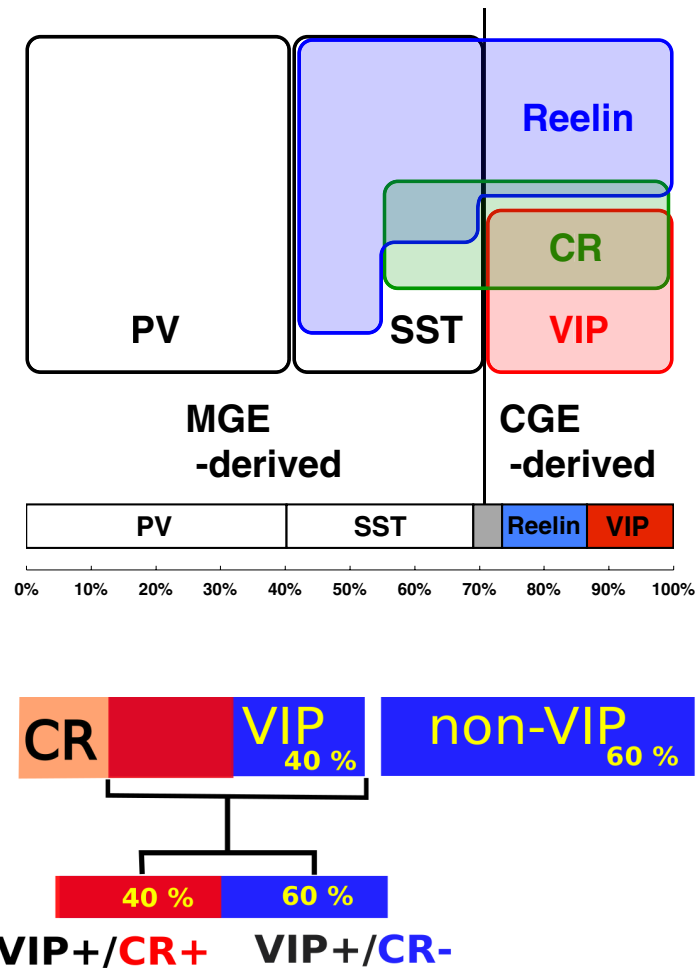
Figure 1.1. Schematic of molecular expression profile of GABAergic interneurons, PV, parvalbumin; SST=SOM, somatostatin; VIP, vasoactive intestinal polypeptide; CR, calretinin; Reelin; MGE, medial ganglionic eminent; CGE, caudal ganglionic eminent. Proportion of cells is indicated PV (40%), SOM (30%), CGE (5HT3a= Gray, Reelin and VIP interneurons, 30%). Bottom panel shows the subdivisions of 5HT3a interneurons, VIP-negative (60%), VIP-positive (40%). VIP-positive can be further subdivided into CR-positive (40-50%), CR-negative (50-60%). 30% of SOM coexpress CR and 33 % of CR coexpress SOM. (Miyoshi et al. 2010; X. Xu, Roby, and Callaway 2010; Rudy et al. 2011).

third group of SOM+ cell type, marked in the "GIN" (GFP in interneuron) transgenic mouse line (Oliva et al. 2000), exhibit intermediate properties (Ma et al. 2006). In mice, a subset of martinotti cells has been shown to express both SOM and the calcium buffering protein calretinin (CR)(Xu et al. 2006). Multiple studies across different cortical areas have implicated PV+ interneurons in gain control (Atallah et al. 2012; Wilson et al. 2012; Moore and Wehr 2013), and SOM+ interneurons in the suppression of lateral and feedback connections (Adesnik and Scanziani 2010; Nienborg et al. 2013). Unlike the medial ganglionic eminence (MGE) derived PV+ and SOM+ interneurons, the caudal ganglionic eminence (CGE) derived 5HT3a interneurons remain poorly defined (Figure 1.1). About 40% of 5Ht3a interneurons co-express the neuropeptide vasoactive intestinal peptide (VIP) and a majority of the remaining 5Ht3a cells are late spiking neurogliaform (NGF) cells expressing Reelin (Miyoshi et al. 2010; S Lee et al. 2010) (Figure 1.1, Figure 1.2). VIP+ cells have been the most studied group of the 5Ht3a interneurons due to the availability of Cre-transgenic mouse lines (Taniguchi et al. 2011). There are nearly nine electrophysiological distinct subtypes of VIP+ interneurons, co-expressing multiple molecular markers and exhibiting distinct morphological phenotypes (Porter et al. 1998; X. Xu, Roby, and Callaway 2010; Miyoshi et al. 2010; S Lee et al. 2010). The major subgroup of VIP cells includes irregular spiking (IS) bitufted/bipolar neurons with vertically orientated axons that can extend from layer 2/3 down to layer 5. Irregular spiking bitufted neurons account for more than 50% of VIP neurons and have been found to express calretinin (CR) (Porter et al. 1998; Miyoshi et al. 2010). The second largest VIP+ subgroup does not coexpress CR and these neurons have been
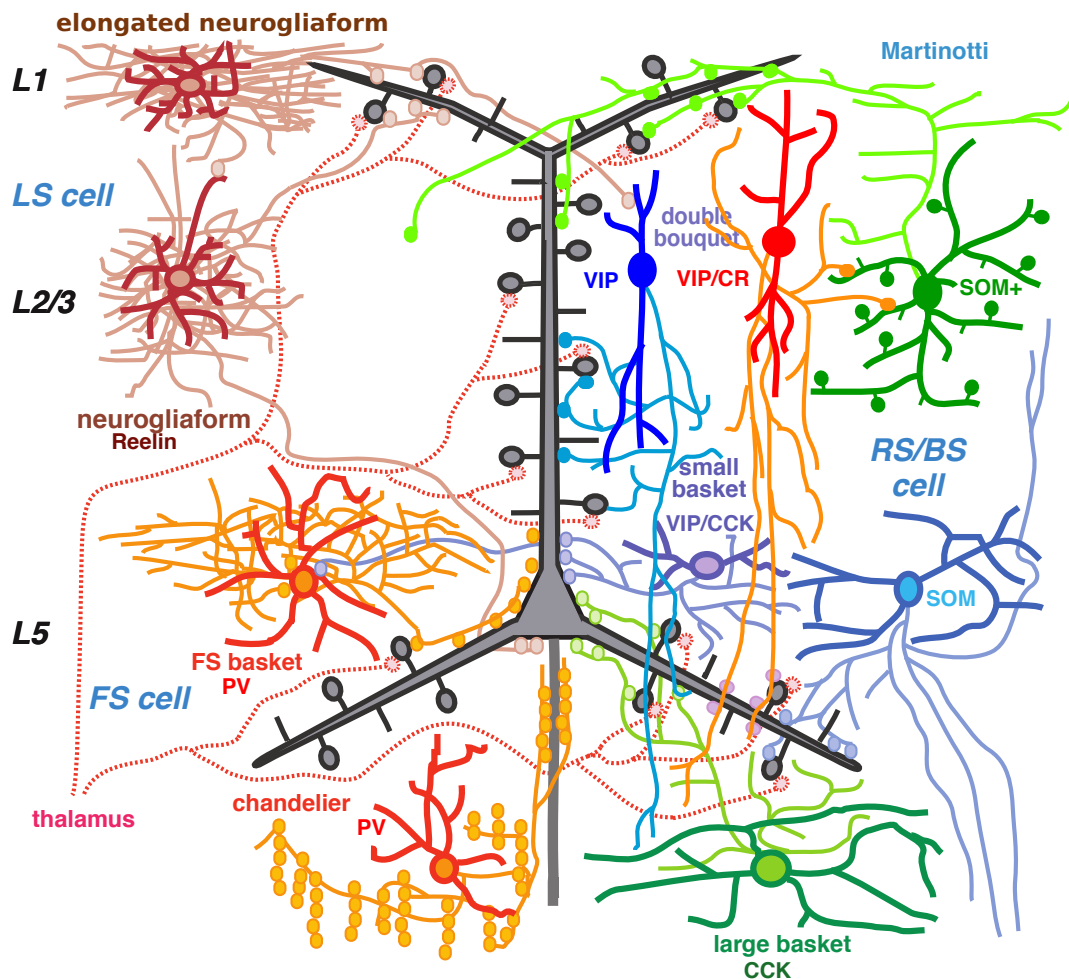
Figure 1.2. Diagram of cortical microcircuit in sensory cortex with inhibitory interneuron subtypes and layer 5 pyramidal neuron. Thalamo-cortical fibers are shown in dotted lines. FS, fast spiking; RS/BS, regular/burst spiking; LS, late spiking; SOM, somatostatin; CR, calretinin; VIP, vasoactive intestinal polypeptide; CCK, cholecystokinin; PV, parvalbumin; IS, irregular spiking (modified from Kubota 2014).

shown to fire burst-like action potentials coined as rapid adapting (Butt et al. 2005), fast-adapting (S Lee et al. 2010; Miyoshi et al. 2010), or irregular spiking type 2 (IS2) (Porter et al. 1998). These cells exhibit bipolar/tripolar dendritic morphology with their axons arborizing extensively locally and vertically. There are also bursting non-adapting 2 (bNA2) bipolar VIP cells and delayed non-fast-spiking 3 (dNFS3) cells that are less prevalent. Despite this diversity, many studies investigating the function and connectivity of inhibitory cells continue to treat VIP interneurons as a homogenous population despite overwhelming evidence that suggests otherwise. In order to reveal the connectivity and function of this diverse cell population with very high cell type specificity, there is a need for a multi pronged approach.

Species differences in VIP interneuron subpopulation

In order to translate data accumulated from rodent models to primates, we must understand species variation amongst cell type classification and function. For example, it is known that primates have a greater proportion of inhibitory cells (20-29%) compared to rodents (15-16%)(Džaja et al. 2014; Barinka et al. 2015). This 30-50% increase in proportion of inhibitory cells in primate is principally due to the increase in the number of CR positive cells, which is increased 5 fold more in layer 2/3 (Džaja et al. 2014). Furthermore, in *Macaca fascicularis* monkey, 80% of VIP interneurons colocalize with CR and form peri-cellular baskets around GABAergic cells in layer 2/3 (Gabbott and Bacon 1997). Meskenaite found that CR-immunoreactive axons in monkey make 80% of their connections onto GABAergic cells and 20% of pyramidal cells in the superficial layer 2/3. While in layer 5, the ratio is reversed, suggesting that "CR immunoreactive neurons appear to have a dual

function of disinhibiting superficial layer neurons and inhibiting pyramidal output neurons in the deep layers" (Meskenaite 1997). In rat layer 2/3, inhibitory cells received 68% of the CR+ terminals and of those, ≥50% innervated other CR+ neurons (Gonchar and Burkhalter 1999). Similar to monkeys, this ratio is reversed in the deep layers. In mice, bipolar CR positive cells connected unto multipolar CR cells with 76.4% rate of connectivity (13/17 pairs) and onto layer 2/3 pyramids with 11.6% connectivity rate (7 of 60) (Caputi et al. 2009). This data suggest that CR bipolar cells likely inhibit multipolar CR+/SOM+ cells in superficial layers more than pyramidal cells. It was later found using Cre-lines expressing blue light sensitive cationic channel (channelrhodopsin-ChR2) selectively in VIP cells that VIP interneurons inhibit SOM+ cells much more strongly than pyramidal cells in layer 2/3 (Pfeffer et al. 2013; Pi et al. 2013a; Soohyun Lee et al. 2013; Pi et al. 2013b; Fu et al. 2015).

From these observations it is clear that use of either VIP-Cre or CR-Cre lines does not provide clear insight into the connectivity of specific cell groups. Expressing ChR2 in all CR positive cells in mice will facilitate activation of both VIP+/CR+ and SOM/CR+ neurons; 2 distinct types. On the other hand use of VIP-Cre mice will lead to expression in both CR+ and CR- cells. However, if ChR2 is restricted exclusively to VIP cells that co-express CR, one may be able to implicate the CR+ subset in disinhibition of layer 2/3 via SOM cells as expected from earlier primate and rat EM studies. This remains an open question in the community.

Function of VIP interneuron in sensory processing

In the past decade there has been rapidly accumulating evidence implicating VIP interneurons in higher order sensory processing, whereby long range lateral

connections from higher cortices recruit VIP interneurons during behaviorally relevant tasks in somatosensory cortex (Lee et al. 2013), visual cortex (Fu et al. 2014; Zhang et al. 2014; Wall et al. 2016) and auditory cortex (Pi et al. 2013a). For example, motor cortex influences somatosensory processing by directly activating VIP interneurons in the somatosensory cortex, which in turn disinhibit pyramidal cells through the inhibition of SOM+ cells (Soohyun Lee et al. 2013). It has also been demonstrated that top down modulation of sensory processing in the visual cortex is mediated by disinhibitory circuits involving VIP and SOM interneurons (Pinto et al. 2013; Alitto and Dan 2013; Zhang et al. 2014; Fu et al. 2014; A. M. Lee et al. 2014).

In addition to releasing GABA, VIP interneurons also release vasoactive intestinal peptide, which has been shown to stimulate glycogenolysis in astrocytes and increase local blood flow by increasing intracellular cyclic adenosine monophosphate (cAMP) (Magistretti et al. 1981; Magistretti 1986; Magistretti 1990). Although VIP peptides play an important role in modulating local energy use in the brain, many studies have instead focused on using VIP expression as a molecular marker to identify a subset of 5Ht3a interneurons as described in Chapter 2.

CHAPTER 2:

Intrinsic properties and local connectivity of vasoactive intestinal peptide expressing inhibitory interneuron subtypes in mouse visual cortex

ABSTRACT

Inhibitory GABAergic interneurons, although small in number, play a major role in increasing the computational power of cortical circuits. Distinct non-overlapping interneuron populations, expressing markers including Parvalbumin (PV), Somatostatin (SOM), Vasoactive Intestinal Peptide (VIP), and Calretinin (CR) can be targeted using transgenic mouse lines. Only about 40% of VIP cells co-express CR (VIP+/CR+) leaving open the possibility that VIP+/CR+ cells might differ from VIP+/CR- neurons in their connectivity and function. To address this question, we take advantage of Flp and Cre driver mouse lines and an intersectional, subtractive adeno-associated virus (AAV) that expresses ChR2 under the control of Flipase and Cre recombinase. We performed in vitro slice whole-cell patch recordings simultaneously in SOM+ inhibitory cells and pyramidal cells during full field optical stimulation of ChR2. VIP interneuron subtypes differ in their intrinsic action potential discharge patterns and their connections to SOM+ interneurons in layer 2/3 of mouse visual cortex. As previously reported for VIP cells, photostimulation of VIP+/CR+ cells evoked inhibitory postsynaptic currents that were much larger in SOM cells than pyramidal cells. In contrast, photostimulation of VIP+/CR- cells evoked stronger responses in pyramidal cells than SOM+ cells. These results suggest that VIP

interneurons are a heterogeneous population that can be separated by expression of CR.

INTRODUCTION

Behavioral states such as alertness and attention can differentially modulate cortical inhibitory cells to increase the computational power of sensory cortical processing (Reynolds and Heeger 2009; Niell and Stryker 2010). The availability of mouse lines that express Cre-recombinase in three major, non-overlapping groups parvalbumin (PV+), somatostain (SOM+), and vasoactive intestinal peptide (VIP+) have allowed for detailed studies of connectivity and function of cortical inhibitory cells (Rudy et al. 2011; Taniguchi et al. 2011). Numerous studies in somatosensory cortex, auditory cortex and visual cortex have implicated VIP+ inhibitory cortical neurons in state-dependent regulation of cortical function whereby VIP+ cells mediate dis-inhibition of layer 2/3 pyramidal neurons by selectively inhibiting SOM+ interneurons (Pfeffer et al. 2013; Pi et al. 2013; Lee et al. 2013; Fu et al. 2014; Zhang et al. 2014). However, VIP+ inhibitory cortical neurons are known to be a diverse population with varying firing properties, and co-expression of calretinin (CR), cholecystokinin (CCK) and Choline Acytransferase (ChAT) (Porter et al. 1998; Xu et al. 2010; Miyoshi et al. 2010; Lee et al. 2010; Prönneke et al. 2015).

Previous studies in primates and rodents have suggested that bipolar calretinin (CR) expressing inhibitory cells, which are a subset of VIP+ cells in rodent, likely participate in the selective inhibition of putative SOM+ cells (Meskenaite 1997; Gonchar and Burkhalter 1999; Caputi et al. 2009). Although mouse visual cortex has 47% of VIP cells co-expressing CR (VIP+/CR+), overlap between CR and SOM in

mice have led to an emphasis on VIP cells rather than CR (Xu et al. 2006; Xu et al. 2010; Rudy et al. 2011). It remains unclear whether VIP+/CR+ cells might differ from VIP+/CR- neurons in connectivity or function.

To address this question, we parsed out the VIP population into two groups by taking advantage of Flp and Cre mouse lines, and an intersectional/subtractive adeno-associated virus (AAV) that expresses ChR2 under the control of Flippase and Cre recombinase (Fenno et al. 2014). We found that the VIP+/CR+ and VIP+/CR- cells differ in their action potential discharge irregularity and their connections to SOM+ cells.

METHODS AND PROCEDURES

Transgenic mice

All animal use and procedures were in accordance with protocols approved by the Salk Institute Institute Animal Care and Use Committee. The GIN (GFP-expressing interneuron) transgenic mouse line, which expresses green fluorescent protein (GFP) in subset of somatostatin-positive (SOM+) cortical interneurons under the control of glutamic acid decarboxylase 67 (GAD67) promoter, was obtained from the Jackson Laboratory (https://www.jax.org/strain/003718; Oliva et al. 2000). VIP-Flp knock-in mice, provided by Josh Huang at Cold Spring Harbor Laboratory (Cold Spring Harbor, NY), were crossed with CR-Cre mice (https://www.jax.org/strain/010774;Taniguchi et al. 2011) and GIN mice to produce a triple transgenic mouse line (VIP-Flp:CR-Cre:GIN) that expresses Cre, Flp and GFP in CR+, VIP+ and SOM+ interneurons respectively.

Histology and image analysis

To determine the proportion and cortical laminar distribution of VIP-positive (VIP+) interneuron subtypes (expressing CR+ vs. CR-), we crossed Ai14 (Cre-dependent expression of tdTomato) reporter mice from Jackson Laboratory (https://www.jax.org/strain/007914), with VIP-Cre driver line (https://www.jax.org/strain/010908;Taniguchi et al. 2011).

Ai14: VIP-Cre mice (P40-60) were deeply anesthetized with Euthasol (100 mg/kg, intraperitoneally), and transcardially perfused with 0.1M phosphate-buffered saline (PBS, pH 7.2-7.4, 40-50ml, 4°C) followed by 100mL of 4% paraformaldehyde fixative (PFA, in 0.1M PBS, 4°C). Brains were then removed and fixed in 4% PFA and 30% sucrose (in 0.1M PBS) solution at 4°C for 24 hours). Post-fixation, brains were transferred to 30% sucrose in PBS and allowed to equilibrate for 48 hours. 50 μm coronal sections were prepared on a freezing microtome. In order to identify calretinin-positive (CR+) cells that colocalized with VIP, sections were incubated in rabbit anti-calretinin (1:1000, Swant, 7697) primary antibodies for 24 hours at 4°C in PBS containing 0.5% normal donkey serum (Chemicon, S30-100ML) and 0.1% Triton-X 100 (Triton-X (EMS, #22142).   Sections were rinsed three times with 0.1% triton-x/PBS at room temperature, followed by incubation in donkey anti-rabbit Alexa-488 (1:500, Jackson ImmunoResearch, 711-545-152) secondary antibody for 4 hours. Sections were counterstained with a 10μM 4,6-diamidino-2-phenylindole (DAPI, Sigma, D-9542) in 0.1M PBS for 20 minutes and mounted on slides with mounting medium containing polyvinyl-alcohol/2.5% 1,4-diazabicyclo[2.2.2]octane (PVA-DABCO). Sections through the primary visual cortex (V1) were imaged at 10x magnification with an Olympus BX-63 upright fluorescent microscope equipped with

an Olympus XM10 digital camera. For each color channel, 7-11 z-planes were acquired and processed in Olympus Cellsens software (Olympus, Waltham, MA). Cells were then marked in transparent image layers in Pixelmator (Pixelmator, Vilnius, Lithuania) based on cortical layer borders defined by density of nuclear DAPI staining. Individual marked image layers were analyzed in ImageJ (NIH) software using the 'particle-analysis' plugin.

Virus preparation

To selectively restrict ChR2 to subpopulation of VIP-positive (VIP+) cells, we used adeno-associated virus (AAV) serotype DJ that expresses ChR2YFP fusion protein under the control of Flippase and Cre recombinase (Fenno et al. 2014). AAV-DJ-nEF–(Flp NOT Cre)-ChR2YFP-WPRE (1.43 x 10^13 GC/ml) and AAV-DJ-nEF-(Cre AND Flp)-ChR2YFP-WPRE (2.40 x 10^13 GC/ml) were produced by the Salk Institute GT3 Core facility. The vector plasmid pAAV-hnEF-Cre-off/Flp-on-ChR2-EYFP (https://www.addgene.org/55649) and pAAV-nEF-Cre-on/Flp-on-ChR2-EYFP (https://www.addgene.org/556444) were provided by Karl Deisseroth (Stanford, CA). AAV8-nEF–FlpDIO-tdTomato (4.68 x 10^14 GC/ml) produced by the Salk Institute GT3 Core facility, was generated by Euiseok Kim (Salk Institute, San Diego, CA).

Animal surgery for virus injection

For expression of ChR2 in VIP+/CR+, VIP-Flp:CR-Cre:GIN mice were co-injected with a 1:1 mixture of AAV-(Cre AND Flp)-ChR2YFP and AAV-FlpDIO-tdTomato at postnatal day 21-40 in the V1 cortex (Figure 2.2A). Prior to surgery, mice were given a cocktail of 100 mg/kg of ketamine and 10 mg/kg xylazine intraperitoneally for anesthesia and mounted in a stereotax (David Kopf Instruments

Model 940 series, Tujunga, CA). Following a two-millimeter diameter craniotomy, virus was injected at coordinates: 3.5 mm rostral, 2.5 mm lateral relative to bregma at three different depth, 0.3 mm, 0.45mm, and 0.55 mm ventral from the pia. We injected 300nl of virus per depth using picospritzer pressure injections (General Valve Corp, Fairfield, NJ). Mice were allowed to recover at 37^oC until ambulatory and given ibuprofen in water for 3 weeks for pain control.

Slice preparation for electrophysiology

Preparation for harvesting acute coronal brain slices is described in (Kim et al. 2015; Appendix A). Briefly, mice (P30-70) were deeply anesthetized with Euthasol (100 mg/kg, intraperitoneally), and transcardially perfused with cold (0-4°C) sucrose artificial cerebral spinal fluid (ACSF) containing (in mM) 87 NaCl, 2.5 KCl, 26 $NaHCO_3$, 1.25 NaH_2PO_4, 1 $MgSO_4$, 10 D-(+)-glucose, 75 Sucrose, 2 $CaCl_2$. Coronal (300 μm thick) sections from the primary visual cortex were cut in ice-cold sucrose ACSF bubbling with 95% O_2/5% CO_2 with a vibrotome (VF-300 Compresstome^{TM}, Precisionary Instruments, Greenville, NC). Slices were allowed to recover in a custom, fine nylon net chamber at 34°C ACSF for 30 minutes, followed by one hour recovery at room temperature in sucrose ACSF bubbling with 95% O_2/5% CO_2. For adult (P50-70) mice, slice preparation was performed as described in (Jiang et al. 2015). Following deep anesthesia, mouse brains were dissected and removed in cold (0−4 °C) NMDG solution containing (in mM) 93 N-Methly-D-Glucamine, 93 HCl, 2.5 KCl, 1.2 NaH_2PO_4, 30 $NaHCO_3$, 20 HEPES, 25 glucose, 5 sodium ascorbate, 2 Thiourea, 3 sodium pyruvate, 10 $MgSO_4$ and 0.5 $CaCl_2$, pH 7.35, bubbled with 95% O_2/5% CO_2. Coronal sections (300 μm thick) were incubated in NMDG solution at 36°C for 10-15

minutes and allowed to recover for one hour at room temperature in physiological solution containing (nM) 125 NaCl, 2.5 KCl, 1.25 NaH_2PO_4, 25 $NaHCO_3$, 1 $MgCl_2$, 25 mM glucose and 2 $CaCl_2$, pH 7.4 bubbled with 95% O_2/5% CO_2.

Basic electrophysiology

Slices were submerged in a custom designed chamber containing recording ACSF with (in mM) 125 NaCl, 2.5 KCl, 25 $NaHCO_3$, 1.25 KH_2PO_4, 1 $MgSO_4$, 20 D-(+)-glucose, 2 $CaCl_2$ and excitatory synaptic blockers (in μM): 50 DL-2-amino-5-phosphonopentanoic acid (DL-AP5, Tocris Bioscience), 20 6-cyano-7-nitroquinoxaline-2,3-dione disodium (CNQX, Tocris Bioscience) as described in (Kim et al. 2015; Appendix A). For adult animals (P50-70), recording was conducted in "physiological" ACSF described above also containing the same synaptic blockers. The recording ACSF was oxygenated with 95% O_2/5% CO_2 and temperature was maintained at 35°C (Temperature controller TC-344B, Warner Instruments LLC, Hamden, CT). Slices were stabilized in the recording chamber with custom designed fine nylon strings attached to a platinum ring. The chamber was continuously infused with oxygenated ACSF at 2-3 ml per minutes with peristaltic pumps (Dyna-max, RP-1, RAININ). Borosilicate glass recording electrode (3-5 MΩ, 0.86 mm inner diameter, 1.5 mm outer diameter), was filled with intracellular solution containing (in mM) 130 K-gluconate, 7 KCl, 0.5 EGTA, 5 Tris-Phosphocreatine, 4 Mg-ATP, 0.3 Na-GTP, 10 HEPES, and 0.3% biocytin (pH 7.3). All patch recordings were performed under visual control using differential interference contrast (DIC) optics and epifluorescent Olympus BX-50WI microscope and Retiga 2000R camera (Qimaging). Recordings were made using a MultiClamp 700B amplifier (Molecular Devices) digitized at 10

kHz and filtered at 4 kHz. Signal was acquired with open-source software *Ephus* (http://www.ephus.org; Suter 2010), and analyzed off-line with custom MATLAB (The Mathworks, Natick, MA) script.

Intrinsic electrophysiology

For intrinsic electrophysiology characterization of VIP+/CR+ and VIP+/CR- cells, we performed current-clamp whole recording in cells expressing ChR2YFP under the control of (Cre AND Flp) cassette, or (Flp NOT Cre) cassette respectively. Since SOM does not co-express with VIP in mouse visual cortex (Xu et al. 2010; Rudy et al. 2011), ChR2YFP+ cells were identified by expression of both red (VIP-tdTomato) and green (YFP) marker (Figure 2.2B) and by presences of robust photo-activation. Input-resistance was calculated as the slope of the regression line fitted to the voltage-current curve using current -50 pA current steps (-50pA to -200 pA, 1 sec duration). To describe the unique spiking characteristics of VIP+ interneurons, we calculated local variation of interspike-interval (LV of ISI) as a function of current injection. Pulse trains were evoked by a one-second duration current step injection (18 pA to 150 pA, 4 pA current steps) and (50 pA to 150pA in 50 pA steps). To compare differences in the degree of spiking irregularities between the VIP+ subtypes, we calculated the local variation of interspike intervals defined as (Shinomoto et al. 2003),

$$Lv = \frac{1}{(n-1)} \sum_{i=1}^{n-1} \frac{3(ISI_i - ISI_{i+1})^2}{(ISI_i + ISI_{i+1})^2}$$

where n is the total number of interspike-intervals (ISI) in a spike train and (ISI_i) is the ith interspike-interval in the sequence. Neurons with independent exponentially

distributed ISI (Poisson-like spiking pattern) yield LV values close to 1 and more regularly spiking neurons yield low LV (<1). Additionally, neurons with burst spiking pattern are associated with large LV (>1). LV values have been found to be robust to fluctuating firing rate (Shinomoto et al. 2005) and in classifying irregularly spiking cells (Shinomoto, Shima, and Tanji 2003; Shinomoto, Miura, and Koyama 2005; Shinomoto et al. 2005; Ardid et al. 2015).

Photostimulation

We performed all photostimulation recording in somatostatin-positive cells while simultaneously recording from a nearby (within 50 μm distance) referenced pyramidal cell. This approach controlled for variability in the level of ChR2 expression, number of infected neurons, and tissue health across animals and tissue slices (Pfeffer et al. 2013). Since the emission spectrum of GFP and YFP overlap, we identified somatostatin-positive (SOM+) cells in VIP-Flp:CR-Cre:GIN mice co-injected with AAV-FlpDIO-tdTomato, and AAV-(intersectional/subtractive)-ChR2YFP as GFP-positive/tdTomato-negative cells. Furthermore, SOM+ cells were not activated by photostimulation. Pyramidal cells were identified under DIC optics based on the triangular somata morphology and regular spiking pattern (Kim et al. 2015; Appendix A). Inhibitory postsynaptic currents (IPSCs) were recorded at a holding potential of ~0 mV with a reversal potential of -60 mV (Figure S2.1A).

A collimated light source from an X-Cite halogen (EXPO) lamp was passed through the epiflourescence path and delivered through a 40x, 0.8 numerical aperture (NA) water immersion lens to provide full-field photo-activation of ChR2 expressing interneurons. Light was passed through a 470/40 nm filter (Chroma, VT) and power

adjusted with a neutral density (ND) filter such that a 4 ms pulse, controlled through an electronic shutter (Uniblitz T132; Vincent, Rochester, NY), produced a single action potential in a ChR2 expressing interneurons (Figure S2.1B). Photostimulation temporal dynamics and relative light power were acquired and recorded for each stimulation sequence with photodiode. To assess for depolarization-induced suppression of inhibition, I recorded from a postsynaptic pyramidal cell at -70mV while photostimulating ChR2 expressing cells with a 4 msec laser pulse at 5 Hz for 5 seconds to measure IPSC at baseline. We then measured IPSC after depolarizing the postsynaptic cell to 0 mV for 2 seconds to assess if there is a reduction in the amplitude of IPSC. Excitatory currents were blocked with (10 uM CNQX and 20 uM AP-5) and we recorded IPSC post-dsi for 18 minutes as shown in CCK+ cell photostimulation in Figure 3.6.

RESULTS

Subpopulation of VIP-expressing interneurons co-express CR

To study the co-expression pattern of CR in a VIP-expressing population, we stained for CR in VIP-Cre/tdTomato mouse line and analyzed the layer distribution (layer 2/3, layer 4 and layer 5/6) of double-labeled cells in primary visual cortex (V1) (Figure 2.1). In agreement with previous studies (Gonchar et al. 2007; Xu et al. 2010; Lee et al. 2010), CR was expressed in VIP neurons (38%, 261/680) (Figure 2.1, Table S2.1). Majority of VIP+/CR+ cells (63%, 176/280) and total VIP interneurons (73%, 494/680) reside in layer 2/3 (Figure 2.1C, Table S2.1).

Intersectional targeting of ChR2 to the VIP subpopulation

To quantify the efficiency of viral infection, we counted double-labeled cells in post-fixed brain slices from VIP-Flp:CR-Cre:GIN mice injected with AAV-Flp NOT-Cre-ChR2-YFP. Since there is no overlap in expression of SOM and VIP in mouse cortex (X. Xu, Roby, and Callaway 2006), all green, tdTomato-negative cells are SOM+, tdTomato-positive cells (yellow in double-exposure panels) are ChR2YFP positive VIP+/CR- cells. The remaining tdTomato cells were predominantly VIP+/CR+ neurons in which the presence of Cre prevented ChR2YFP expression. From this calculation, we found that 18.2%, (30/165) of VIP+ cells infected with AAV-FlpDIO-tdTomato expressed ChR2YFP (Figure 2.2). By normalizing the proportion of cells infected (18%) with the proportion of VIP+/CR- cells, we can estimate virus efficiency.
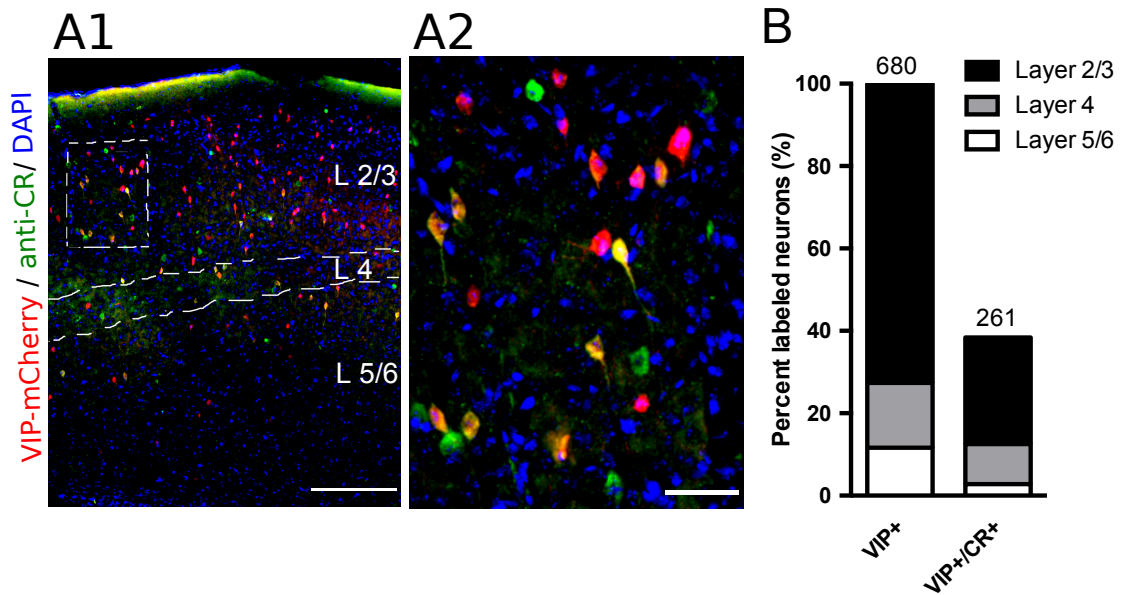
Figure 2.1. Proportion of VIP+/CR+ cells in mouse visual cortex (A) Immunoflourescent image of coronal section from mouse visual cortex of vasoactive intestinal peptide (VIP) Cre-driver line crossed with a ROSA-tdTomato reporter line and stained for CR marker (green). Cortical layer borders shown as dashed lines in A1 were determined from DAPI (blue) staining. **(A2)** higher magnification image of selected region shows VIP+/CR+ double labeled (yellow) cells and VIP+ cells labeled in pink. **(B)** Laminar distribution and proportion of VIP+ and VIP+ colocalized with CR marker in adult (postnatal days 30-60) mouse. Total number of cells counted is shown above the histogram. Scales: 150 μm (A1), 35 μm (A2).
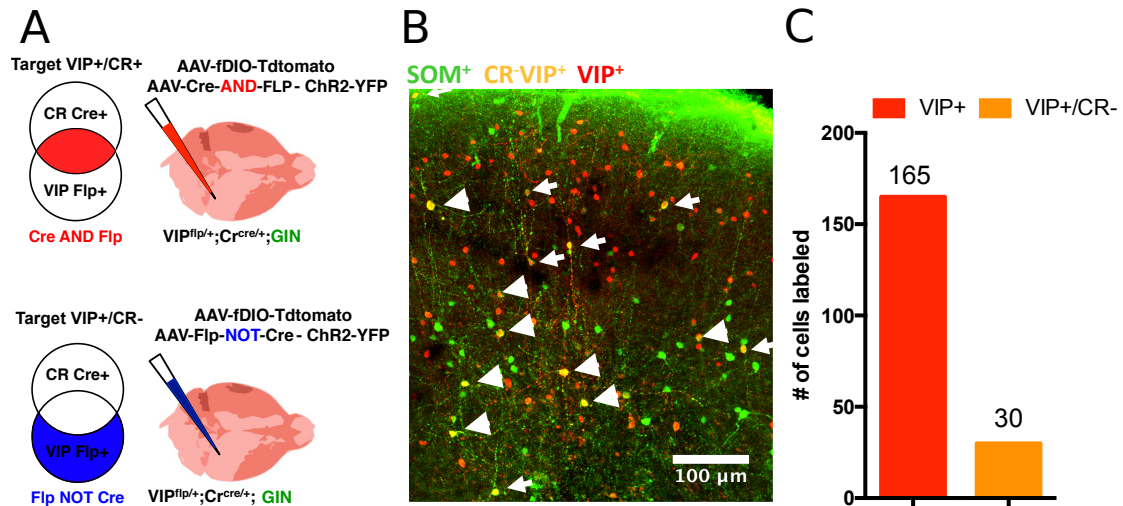
Figure 2.2. Intersectional targeting of VIP+/CR+ versus VIP+/CR- inhibitory cortical neurons. (A) Schematic diagram of the experimental design showing VIP+/CR+ or VIP+/CR- neurons (red and green respectively) will express ChR2YFP by combinatorial recombinase expression from "Cre AND Flp" or "Flp NOT Cre" cassettes, respectively. **(B)** Confocal micrograph of V1 coronal from VIP-Flp:CR-cre:GIN triple transgenic mouse line injected with AAV-Flp NOT Cre-ChR2YFP (expression in VIP+/CR- cells) and AAV-FlpDIO-tdTomato (expression in VIP+ cells). Double immunoflourescent staining (yellow) denotes VIP+/CR-, expressing both tdTomato and ChR2-YFP. VIP+/CR- cell population contains a mixture of multipolar (large arrowheads) bipolar (small arrows) cells. **(C)** Quantification of infected neurons expression of tdTomato in VIP cells and ChR2YFP in VIP+/CR-cells (3 sections, two animals).

If we assume that the CR antibody labeled all CR+ cells, we can attribute all VIP+ cells that were not labeled with CR antibody in the immunohistochemistry study to represent the proportion of VIP+/CR- cells (62%, 419/680). By taking the percent of cells infected (18%) with the virus and dividing by the propotion of VIP+/CR-, we estimated the efficiency of the (Flp NOT Cre) virus to target VIP+/CR- to be a modest ~30 % (18/62). This value also assumes that the tropism for inhibitory cells between AAV serotype 8 and AAV serotype DJ are similar.

VIP interneuron subtypes differ in the degree of spiking irregularity

All basic electrophysiology parameters measured, input resistance (VIP+/CR+, 195 ±567 MΩ; VIP+/CR-, 263 ±78 MΩ ,) , AP amplitude (VIP+/CR+, 48± 5 mV, n=4; VIP+/CR+, 46± 4 mV, n=5), AP maximum rate of rise (VIP+/CR+, 154 ± 26 mV/sec mV/sec, n=4; 129 ± 14 mV/sec, n=5), and AP maximum rate of fall (VIP+/CR+, -91 ±17mV/sec, n=4; VIP+/CR-, -64 ± 11 mV/sec, n=5) were not statistically different (Table 2.1). Interestingly, VIP+/CR+ neurons fired more regular spiking pulse train with increasing current injection, while VIP+/CR- neurons fired more irregularly spiking pulse train with increasing current amplitude (Figure 2.3A/B). To quantify this observation we took the log of the ratio of local variation at high current and low currents. In summary, the mean log ratios indicate that VIP+/CR+ (VIP+/CR+, -0.7080 ± 0.2631, n=4) cells can be distinguished from VIP+/CR-, (0.3661 ± 0.3289, n=4, mean±SEM) by observing the variation in spiking pattern during current injection (Figure 2.3C).
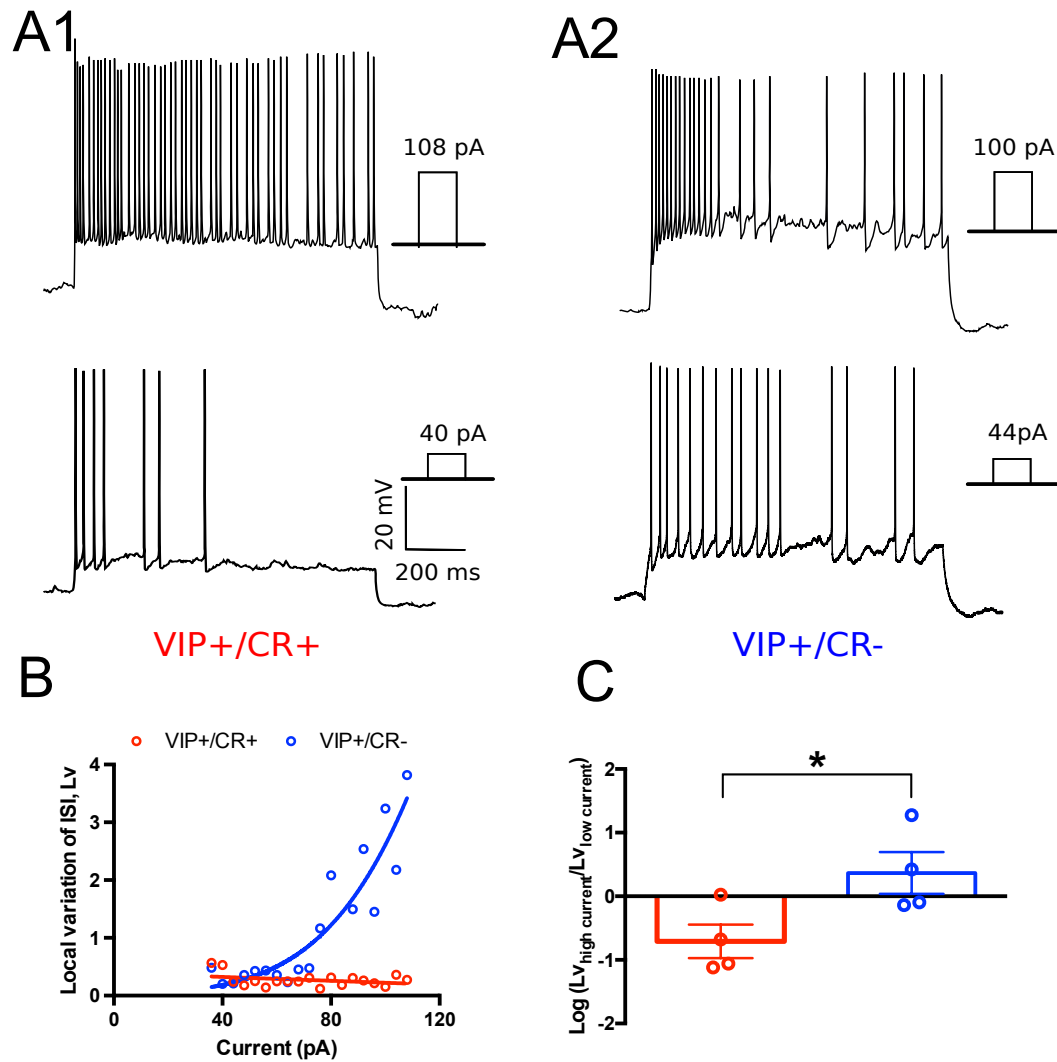
Figure 2.3.Local variation in irregular spiking pattern between VIP+/CR+ and VIP+/CR- cells. (A) Example spike trains for VIP+/CR+ cells in (A1) and VIP+/CR-cells in A2 at low and high current injection. Note the change in spike irregularity between the two current injections, CR+ cells become more regular spiking and CR-become more irregular spiking/bursting (B) Example local variation as a function of current amplitude (-18 to 108 pA, 1 second duration) for VIP+/CR+ in red and VIP+/CR- in blue (C) Log ratio of local variation at high currents over local variation at low currents (VIP+/CR+, -0.7080 ± 0.2631, n=4 mean±SEM and VIP+/CR-, 0.3661 ± 0.3289, n=4, mean±SEM). Lv was selected from low (VIP+/CR+, 39±8 pA; VIP+/CR-, 44 ±6 pA) and high currents (VIP+/CR+, 86±27 pA; VIP+/CR-, 86±8 pA). Data are presented as mean ±SEM. For the log ratio of local variation plot, statistical significance is labeled as p value after student t-test *p < 0.05 Abbreviations: Lv, local variation in ISI, ISI interspike interval, VIP+ vasoactive intestinal peptide positive, CR+, calretinin positive.

Table 2.1. Electrophysiological Properties of VIP interneuron subtypes. Shown are mean ± SEM. For AP amplitude, AP rise rate, AP decay rate and Log-ratio (Lv) for VIP+/CR+, n=4 for VIP+/CR-, n=5. For Input resistance, for VIP+/CR+, n=3 for VIP+/CR-, n=3. Data are shown as mean±SEM. For statistical comparison, unpaired parametric t-test was used. $*p < 0.05$.

	VIP+/CR+	VIP+/CR-	Statistical Comparisons
Rin (MΩ)	195.4 ± 56.64	262.8 ± 77.92	ns
AP Amplitude (mV)	48.19 ± 5.046	46.49 ± 4.420	ns
AP rise rate (mV/sec)	153.6 ± 25.99	129.0 ± 13.70	ns
AP decay rate (mV/sec)	(-)90.86 ± 17.22	(-)64.14 ± 10.76	ns
Log ratio (Lv_H/Lv_L)*	(-)0.7080 ± 0.2631	0.3661 ± 0.3289	* p<0.05 student t-test

Pyramidal neuron responses are more frequent when stimulating VIP+/CR+ than VIP+/CR- neurons

To assess possible differences in connectivity of VIP interneuron subtypes onto pyramidal neurons in layer 2/3, we examined inputs to pyramidal neurons in all our paired recording experiments of which pyramidal neurons were used as a reference. Following photo-activation of VIP+/CR+ neurons, light-evoked IPSCs were detected in 6 out of 17 patched reference pyramidal cells (average IPSC 27±6pA, n=6 mean±SEM) (Figure 2.2C). However, following photo-activation of VIP+/CR- cells only 4 out of 35 patched referenced pyramidal cells had IPSCs above spontaneous background levels (average IPSC 57±25pA, n=4 mean±SEM) (Figure 2.2C).

We considered the possibility that recording inhibitory currents under depolarizing conditions (at ~0mV) might induce depolarization induced suppression of inhibition (DSI) (insert references), preventing the detection of inhibitory inputs following activiation of VIP+/CR- neurons. To determine if the VIP+CR- neuronal population exhibits depolarization induced suppression of inhibition (DSI) mediated by endocannabinoid receptors (CB1R), pyramidal cell recordings were conducted at -70 mV holding potential using a high chloride internal solution with an inhibitory reversal potential of 0 mV (n=4) (See Methods). Post-synaptic pyramidal cells were recorded while photo-activating VIP+/CR- cells expressing ChR2 at 5 Hz and responses were assessed before, and after depolarization from -70 mV to 0 mV holding potential for two seconds. There were no light-evoked IPSCs detected in patched pyramidal cells (5/5) at any time during the DSI protocol, suggesting that decreased response rate may reflect low connection probability (VIP+/CR- to

pyramidal cell) rather than suppressed synaptic release of inhibitory transmitter (Gamma-Aminobutyric Acid, GABA). Although it is possible that we may be underestimating the probability of connection for VIP+/CR-, it is unlikely given the high sample (n=35). Paired recordings between VIP+/CR- cells and nearby pyramidal cells would likely show similar probability of connection (Jiang et al. 2015).

VIP+/CR+ interneurons preferentially inhibit SOM+ cells but VIP+/CR- do not

Photostimulation of VIP+/CR+ neurons while recording simultaneously from a layer 2/3 pyramidal neuron and a layer 2/3 SOM+ neuron reveals much stronger connections to SOM+ neurons relative to neighboring pyramidal cells; similar to the bias previously shown for CR+ neurons (Caputi et al. 2009) or VIP+ neurons in cortical layer 2/3 (Pfeffer et al. 2013; X. Jiang et al. 2015; Karnani et al. 2016). In the 6 SOM+/pyramidal neuron pairs recorded in layer 2/3 of V1 the evoked IPSCs in the reference pyramidal cell, there were far stronger (about 5 to 10-fold) in the SOM+ cells (151±13pA, n=6 mean±SEM) than pyramidal cells (27±3pA, n=4 mean±SEM) (Figure 2.5A). In strong contrast, following photo-activation of VIP+/CR- cells no detectable IPSCs in SOM+ cells were evoked above background spontaneous levels for four SOM+/pyramidal pairs (Figure 2.5B). To measure the relative synaptic strength of these connections, we calculated inhibitory postsynaptic charge (IPSQ, picoCoulombs pC) transferred, by taking the area under the inhibitory postsynaptic current (IPSC, pA) and tracing in the time window from the start of the 4 ms duration blue-light stimulus to 100 ms post-stimulus. The relative synaptic strength of VIP+/CR+ to SOM+ cells was significantly larger (IPSQ$_{som}$ is 1.96 ± 0.17 pC and IPSQ$_{pyr}$ is 0.46 ± 0.03 pC, mean±SEM, ratio of 4.26) than VIP+/CR- to SOM+ cells

(IPSQ$_{som}$ is 0.25 ± 0.04 pC and IPSQ$_{pyr}$ is 1.56 ± 0.57 pC, mean±SEM, ratio of 0.16) (Figure 2.5C). Note that VIP+/CR- to SOM+ cells IPSQ$_{som}$ reflects spontaneous background activity rather than evoked release of inhibitory current. These results indicate far stronger relative input to SOM+ neurons from VIP+/CR+ than from VIP+/CR- neurons suggesting that VIP interneuron subtypes defined by presence or absence of CR expression differ in relative innervation of SOM+ cells in mouse visual cortex.

The lack of response in SOM+ neurons cannot be attributed to failure to express sufficient levels of ChR2, as we observed high expression level of ChR2YFP with an expression rate of ~18% in post-fixed recorded slices. Neither can it be attributed to failure to activate ChR2+ cells as we demonstrated reliable single action potential in VIP+/CR- ChR2YFP expressing cells (Figure S2.1B) upon photostimulation. Furthermore, in 4 cell pairs, evoked responses were detected in the pyramidal cell, indicating successful photoactivation, but no response was evoked in the SOM Cell. We also detected evoked IPSCs in one SOM+ cell in a slice with no reference pyramidal (Figure 2.5C, pair 5). This suggests that VIP+/CR- neurons might make weak connections to both pyramidal neurons, and SOM+ cells and instead favor some other inhibitory cell type. To target recording in Parvalbumin (PV) expressing interneurons, we crossed VIP-Flp:CR-cre mouse line with the G42 line (GFP expressed in subpopulation of PV+ cells) (Chattopadhyaya et al. 2004). We found no detectable evoked IPSCs in PV+ cell and in ChR2YFP-negative VIP+ cells following photo-activation of VIP+/CR- cells.
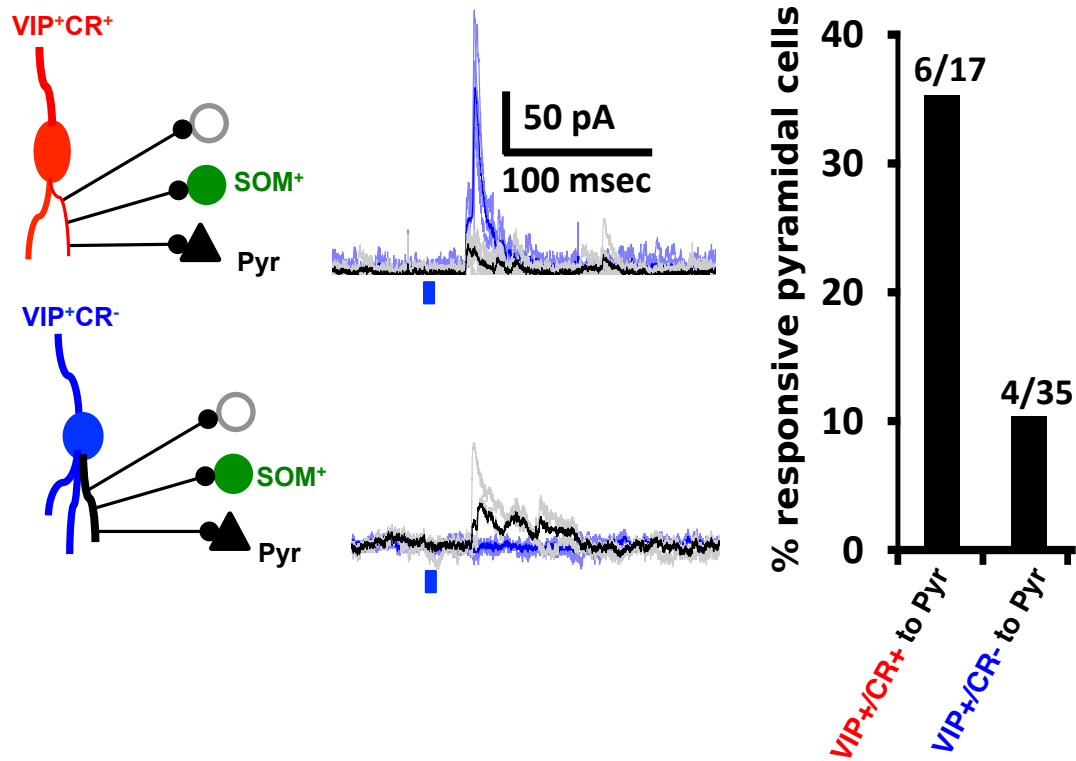
Figure 2.4. Inhibitory postsynaptic current recorded in referenced pyramidal cells (A) Schematics of recording condition. (B) Example inhibitory postsynaptic currents (IPSCs) measured in the referenced pyramidal (Pyr) cell (black and gray) and in somatostatin (SOM+) cell (blue and light blue), following a 4 ms blue light pulse photo-activation of ChR2 expressed in either VIP+/CR+ neurons (A1, B1) or VIP+/CR- neurons (A2, B2). (C) Percent of patched pyramidal cells with evoked IPSC following activation of VIP+/CR+ or VIP+/CR-.
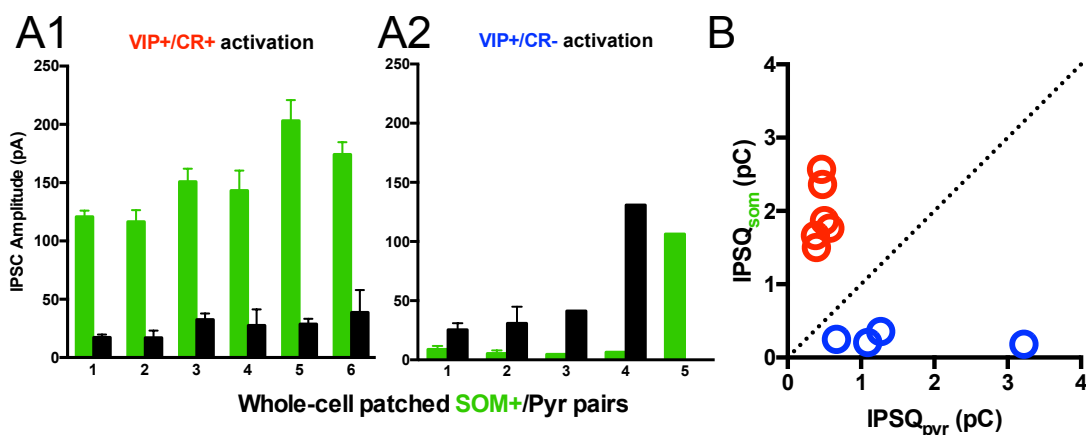
Figure 2.5. VIP+/CR+ preferentially inhibit SOM not VIP+/CR- A) Inhibitory post-synaptic current amplitudes from each pyramidal cell (black) and paired SOM+ interneuron (green) following activation of VIP+/CR+ (A1) or VIP+/CR- neurons (A2) Only pairs with evoked IPSC in the reference pyramidal cell were included. (A2) Responses recorded in the SOM+ neurons do not exceed mean spontaneous activity values measured during a pre-stimulus interval except for pair 5, which is from a slice with no paired pyramidal cell with an evoked IPSC. (B) Comparisons of input strength (expressed as IPSC charge transfer (pA x s) from VIP+/CR+ (blue circles) or VIP+/CR- (red circles) neurons onto post-synaptic pyramidal neurons (x-axis) versus simultaneously recorded post synaptic SOM+ inhibitory neurons (y-axis). The dotted line indicates the unity line. Statistics were calculated from Wilcoxon matched-pairs signed rank test to compare IPSC in SOM+ cells and pyramidal cell in each pair. Values are reported as means ± SEM. Significant differences was observed for VIP+/CR+ with $p < 0.05$ mean±SEM.

DISCUSSION

Using intersectional optogenetic strategies, this study demonstrates distinct differences in intrinsic firing properties and connectivity of VIP interneuron subtypes, suggesting that VIP interneuron can be split into two populations based on CR coexpression. The strong connectivity to SOM+ cells observed in the VIP+/CR+ subtypes is consistent with observations seen for VIP interneurons in multiple cortical areas (Pfeffer et al. 2013; Lee et al. 2013; Pi et al. 2013a). The low evoked IPSC rates observed in the VIP+/CR- group to all postsynaptic cell types sampled (pyramidal, PV, and other VIP cells) suggests VIP+/CR+ cells may have an alternative mechanism of modulating and recruiting postsynaptic cells. Although we normalized recording to nearby pyramidal cells, paired recording experiments similar to (Jiang et al. 2015) may be warranted to determine absolute probability of connection and unitary synaptic strength for VIP+/CR-. Based on this study, we can predict that VIP+/CR- population will have diminished inhibitory synaptic strength and low probability of connection to majority of post-synaptic cells in layer 2/3 compared to VIP+/CR+ cells.

VIP subtypes distinguished based on spiking variability

It has been suggested that VIP interneurons can be split into two distinguishing subtypes based on somata location (layer 2/3 vs. layer 4/5/6 cells). The majority of layer 2/3 VIP neurons have axon boutons terminating in layer 2/3 and layer 5a. In contrast, VIP neurons with somata residing outside of layer 2/3 were found to have axons terminating in layer 5b and layer 6. Although there was no difference in the basic membrane properties between VIP interneurons, (Prönneke et al. 2015) noted differences in the afterhyperpolarization (AHP) which have been shown to regulate

spike timing (Dumenieu et al. 2015; Saito et al. 2008). Neurons exhibiting the slow component of AHP and prominent afterdepolarization potential (ADP) show greater variability in spike discharge pattern and are more irregular spiking than those without ADP. In this study we demonstrate changes in the spike timing variability between VIP subtypes delineated by the expression of CR. Similar to (Prönneke et al. 2015), we see no differences in basic electrophysiological parameters but observe differences in irregularity of spiking and connectivity of SOM+ cells in layer 2/3.

Data from chapter 2 suggest that the dynamic range of interspike interval variability of VIP interneurons can be used to distinguish VIP subtypes. Rather than maintaining one distribution probability function and simply increasing spike rates, VIP interneurons change their interspike interval distribution as a function of input current amplitude. The variability of spiking between VIP subtypes may not only serve as a diagnostic tool to distinguish the two populations electrophysiologically, but may also play a functional role in temporal code and rate coding of sensory information. In particular, behaviorally relevant processing requires robust changes in spiking variability as shown in somatosensory cortex (Hires et al. 2015) and during motor learning (Peters et al. 2014). Recruitment of VIP+/CR+ cells may drive cells to become more reliable with increasing input strength, thus increasing cortical synchrony. However, recruitment of VIP+/CR- cells may lead to increased cortical asynchrony. Each subtype may act as a high pass filter and low pass filter respectively.
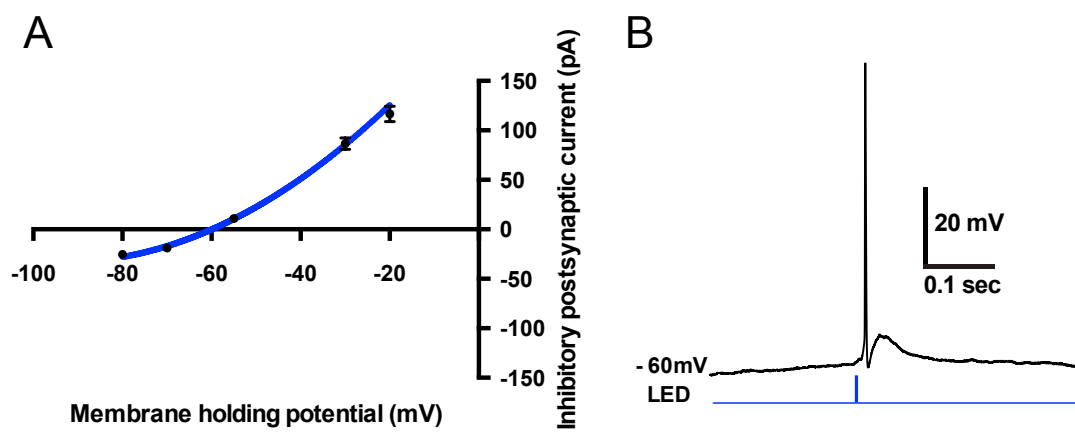
Figure S2.1. Inhibitory reversal potential and photo-activation of ChR2 expressing cell (A) Voltage-current relation showing inhibitory reversal potential of -60 mV potential (B) Current clamp recording from ChR2 expressing cell photoactivated with a 4 ms duration blue light calibrated to produce a single action potential.

ACKNOWLEDGEMENTS

Chapter 2, in full, is a manuscript in preparation as: Espoir M. Kyubwa, and Edward M. Callaway. "Intrinsic properties and local connectivity of vasoactive intestinal peptide expressing inhibitory interneuron subtypes in mouse visual cortex" The dissertation author is the principle author of the paper.

CHAPTER 3:

Layer and cell type specific dissection of cortical inhibitory circuit using laser-scanning photostimulation

INTRODUCTION

The cortex is not a uniform mass of randomly connected, generic neurons, but rather a collection of specific cell types integrated in a precise circuit network. Inhibitory cells comprise 20% of the entire cortical neuronal population, which can be classified by morphology, intrinsic membrane properties, expression of chemical markers and connectivity patterns (Gupta, Wang, and Markram 2000; DeFelipe et al. 2013). Connectivity can be defined at different scales. For example Chapter 2 addressed cell type specific local connectivity that was restricted within 50 um distance, while Appendix A defines cell type based on long-range connectivity. The aim of this chapter is to identify layer specific connectivity for SOM+ and CCK+ cells. SOM+ have been shown to mediate strong disynaptic inhibition between pyramidal cells in layer 5, however, a subset of SOM+ cells extend their axons up to layer 1 and are thus positioned to enervate dendrites of pyramidal cells from all layers. It remains unclear whether SOM+ cells preferentially provide intra-laminar or inter-laminar inhibitory input (Silberberg and Markram 2007; Krishnamurthy, Silberberg, and Lansner 2012). CCK+ cells discharge irregular action potentials similar to VIP cells discussed in Chapter 2.These cells also express cannabinoid receptors (CB1) on their axon terminals, making them subject to depolarization-induced suppression of inhibition (DSI) and neuromodulatory control of excitatory cortical neurons (Galarreta

et al. 2004; Bodor et al. 2005; Galarreta et al. 2008). The role of CCK+ cells irregulating output from different types of cortical pyramidal neurons in different cortical layers remains to be elucidated.

To address these questions we expressed ChR2 in SOM+ cells or CCK+ cells using a reporter mouse line and photostimulate ChR2 expressing cells with fine special resolution laser scanning. We found that laser-scanning photostimulation activates both cell body and axon passage providing an input map that is contaminated with presynaptic axons and presynaptic cell bodies. This result led us to develop a virus that expresses ChR2 in somatodendritic regions and avoids axons. With the somatodendritic targeted ChR2 virus and laser scanning photostimulation, future studies will be able to map cell type specific inhibitory input with single cell resolution.

METHODS AND PROCEDURES

Transgenic mice

All animal use and procedures were approved by the Institute Animal Care and Use Committee at the Salk Institute. Ai32 mice (Express channelrhodopsin-2 YFP under the control of Cre-recombinase) (https://www.jax.org/strain/024109; Madisen et al. 2012) were crossed with either Somatostain-ires-Cre (Jackson Laboratory (https://www.jax.org/strain/013044; Taniguchi et al. 2011) or Cholecystokinin-ires-Cre (https://www.jax.org/strain/012706; Taniguchi et al. 2011) mice from Jackson Laboratory.

Electrophysiology and photostimulation

Preparations for harvesting acute coronal brain slices are described in (Kim et al. 2015; Appendix A) and in chapter 2. Postsynaptic cells were held at − 0 mV and -70 mV with high chloride internal solution for assessing DSI at room temperature in artificial cortical-spinal fluid (ACSF) as described in Chapter 2 and in the Appendix A). Note, we blocked excitatory currents with 10 uM CNQX and 20 uM AP-5. We used laser scanning photostimulation methods (Katz and Dalva 1994; Shepherd, Pologruto, and Svoboda 2003; Petreanu et al. 2009) to photoactivate ChR2 expressing interneurons to map input onto pyramidal cells in different layer.

A blue laser (473 nm, Laserglow Technologies) was scanned at the objective lens focal plane with translating galvanometer scan mirrors (Cambridge Technology). 4 ms duration light pulses were controlled with a shutter (Uniblitz T132; Vincent, Rochester, NY), and power was adjust such that one 4 ms pulse generated a single action potential in ChR2 expressing neurons as done in Chapter 2 (Figure 3.1). The beam diameter was adjusted to slightly under fill the back aperture of the 4x objective lens 0.16 NA (UplanApo, Olympus) to allow for a two-dimensional mapping in the plane of the brain slice. During photostimulation, laser onset and power was recorded with a photodiode connected to an amplifier. Three pulses were delivered at 5 Hz in a 16x16 grid pattern or 16x8 grid pattern with 50 um spacing aligned with the pia and centered vertically over the recorded neuron. We repeated each map 2-3 times and averaged across trials. Recordings were made using MultiClamp 700B amplifier (Molecular Devices) digitized at 10 kHz and filtered at 4 kHz. Signal was acquired with open-source software *Ephus* (http://www.ephus.org; Suter 2010), and analyzed off-line with MATLAB (The Mathworks, Natick, MA) script.

RESULTS AND DISCUSSION

Laser scanning photostimulation evokes reliable IPSCs in postsynaptic neurons from axons of passage.

Unlike in virus mediated ChR2 expression, Ai32 ChR2 reporter lines, which are highly efficient in expressing ChR2 in all Cre expressing cells, were crossed with CCK-Cre mice or SOM-Cre mouse. Photoactivation of ChR2 expressing SOM+ cells evoked reliable monosynaptic inhibitory postsynaptic currents with onset delays consistent with ChR2 dynamics (Boyden et al. 2005) (Figure 3.2). Pyramidal cells in layer 2/3 received upwards of 600 pA of current when SOM cells are within 50 uM diameter (Figure 3.4 left panel). Although responses for layer for layer 5 pyramidal cells are weaker, the input map seems to trace the dendritic morphology of layer 5 (Hooks et al. 2013), which is know to have dendritic shafts that extends up to layer 1 (Figure 3.4 right panel). From this result, we learned that laser scanning photostimulation of ChR2, which is unrestricted from the axon, cannot be used to accurately locate input cells as the map also includes axons of passage. This led us develop a Cre dependent virus that expresses ChR2 in somatodendritic regions of the cell. After doing a little literature search, we found a somatodendritic targeted ChR2 virus that was developed by K. Svoboda lab. This CHR2-MBD virus expressed ChR2 tagged to a myosin-binding domain (MBD) as allow the shuttling of ChR2 to the membrane and not the axon. This is due to the mixed orientation direction of microtubules at the axon hillock that prevents myosin from traveling through this segment. We cloned the Cre lox sites in the plasmid to restrict expression to specific cell type. Figure 3.6 shows a fluorescent image of layer 5 pyramidal neuron (Cre line)

expressing ChR2YFP in only dendrites and not cell axon as evidence by the lack of YFP expression in the white matter. Photostimulation of sparsely labeled cells would allow single cell resolution mapping as long as the dendritic barbarization are non-overlapping or the power is sufficiently low to separate two near by presynaptic cells.

Activation of CCK expressing cells in a 16x16 grid pattern also mapped dendritic shafts of layer 4 and layer 5 pyramidal neurons (Figure 3.5). This was quantified as the relative inhibitory input histogram across cortical height. In layer 2/3 pyramidal cells, we confirmed the presence of DSI indicating that majority of the cells activated had endocannabinoid receptor 1b on the axon terminals (Figure 3.6 left panel). There was a 30% reduction in IPSC following depolarization of postsynaptic pyramidal cells (n=2). The recovery curve of the IPSC to near baseline amplitude follows a characteristic receptor-ligand pharmacokinetics seen in DSI (Figure 3.5 left panel) (Bodor et al. 2005; Galarreta et al. 2008).

ACKNOWLEDGEMENTS

Figure 3.1. Schematic of photostimulation setup. The laser beam is guided successively as an open beam system through a shutter, a neutral density (N.D.) filter and a beam splitter which reflects 30 % of the light to a photodiode connected to an amplifier to record laser power and onset during photostimulation. Galvanometer mirrors are positioned in the beam path and controlled by Ephus software to photostimulate in a grid like pattern in the Cartesian coordinate of the slice. Two scan lens are positioned away from the dichroic mirror such that the beam under fills the back aperture of the 40x objective with a diameter of 50 um at the focal point (Ikrar et al. 2011; C. C. Lee et al. 2013)
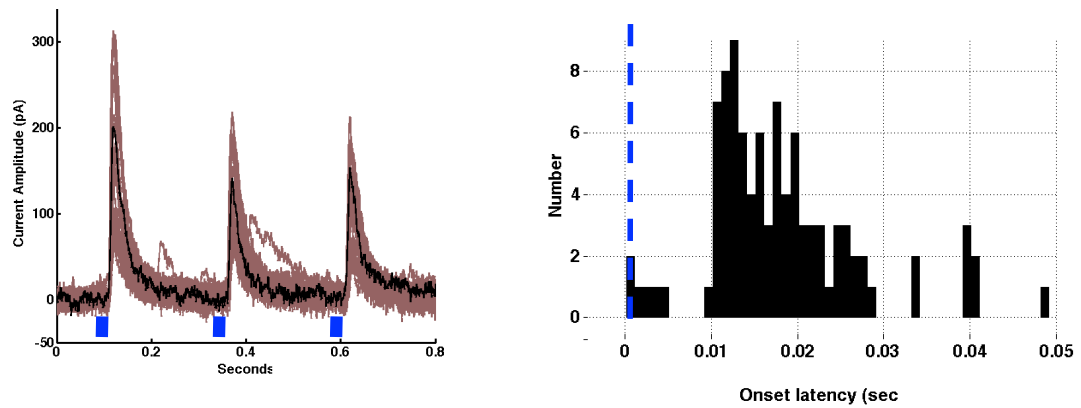
Figure 3.2. **Photostimulation of ChR2 expressing SOM+ cells evokes reliable IPSC in postsynaptic pyramidal neuron.** Left panel shows reliable evoked IPSC in postsynaptic pyramidal neuron stimulated with a 4 ms blue light. The middle panels are average IPSCs amplitudes for two pyramidal neurons. Right panel is a histogram of the onset latency consistent with ChR2 temporal dynamics.
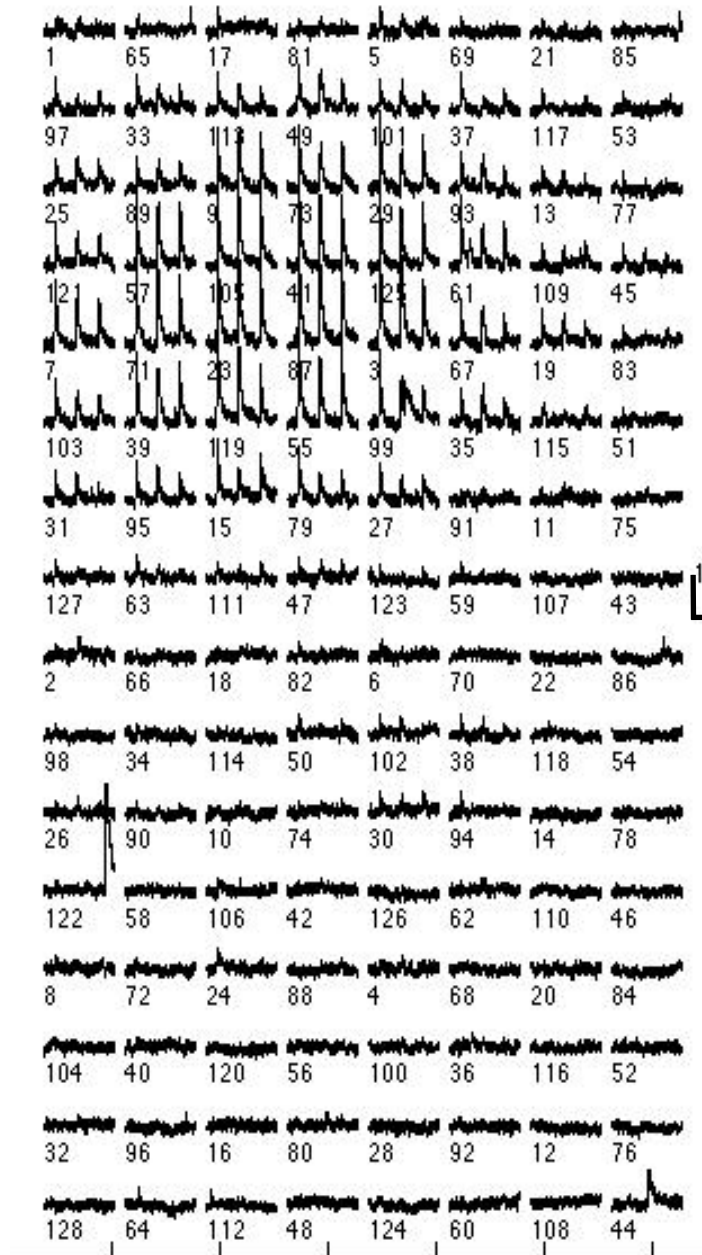
Figure 3.3. 16x8 photostimulation grid. This is an example map from patching layer 2/3 pyramidal cell while stimulating ChR2 expressing SOM+ cells in mouse visual cortex. Numbers indicate the photostimulation sequence. Each position contains a 1 sec inhibitory postsynaptic potential trace. The scale bar is 100 pA vertical and 0.5 sec horizontal.
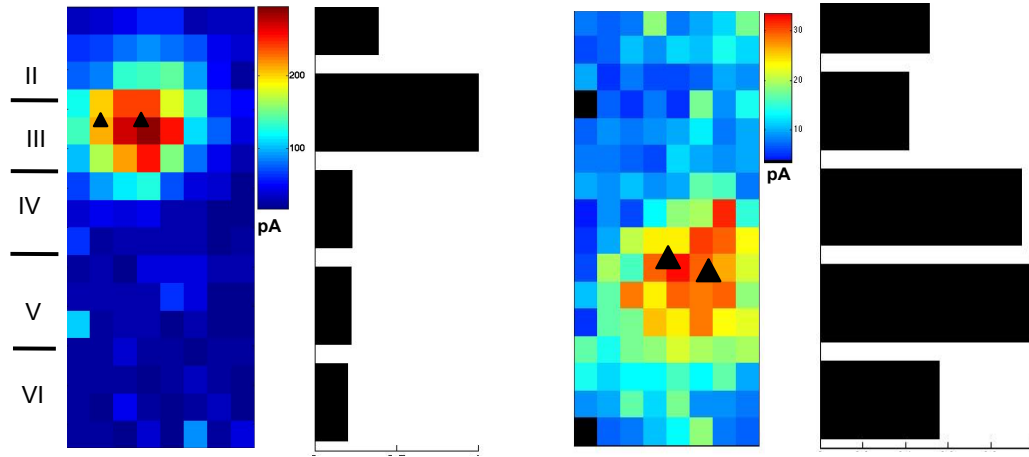
Figure 3.4 Somatostatin-positive (SOM+) provides intra-laminar input to pyramidal cells. In the both panel IPSCs were measured in pyramidal cells voltage clamped at 0 mV while photostimulating ChR2 expressing SOM+ neurons in a 16x 8 grid pattern with 60 um spacing. Heat maps are average maximum amplitude input maps for pyramidal cells (n=2). Histograms are the normalized laminar distribution normalized to the maximum IPSC amplitude (600 pA for left panel and 35 pA for right panel)
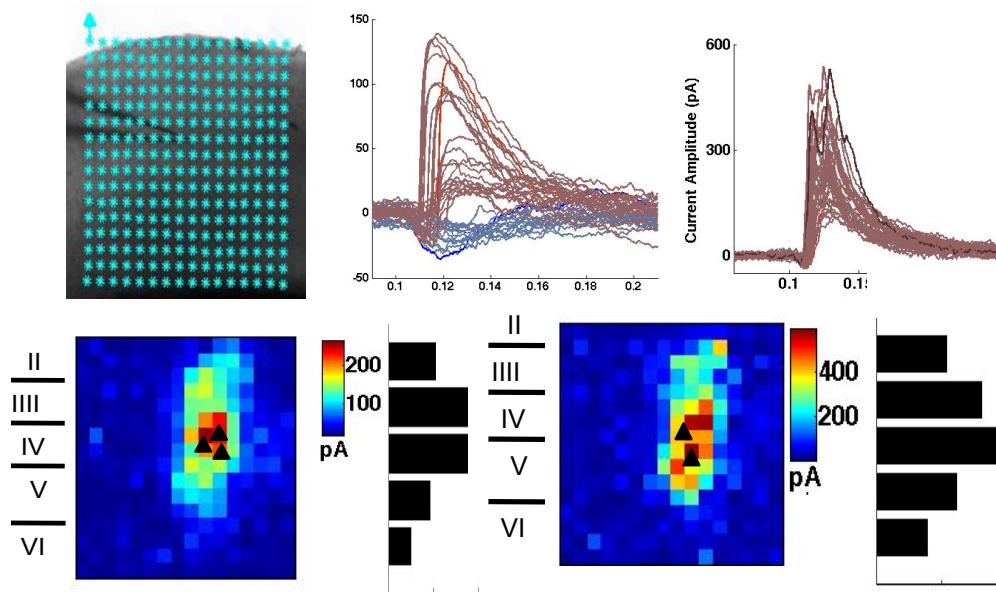
Figure 3.5 Cholecystokinin-expressing neurons provide inter-laminar input to layer 5 pyramidal cell. Upper Left panel is an image of a 16x16 laser scanning photostimulation grid with 60 um spacing overlay on top of an acute coronal cortical slice. Upper middle panel is an example postsynaptic current trials in a layer 5 pyramidal cell held at 0 mV. The brown traces are inhibitory currents from activating presynaptic CCK cells and the blue traces are direct activation of channelrhodopsin currents in the recorded cell. Note, CCK is expressed in some pyramidal cells and thus in an Ai27:CCK-cre mouse line, ChR2 would be expressed in pyramidal cells. Upper right panel is an example where inhibitory current dominates channelrhodopsin currents. Bottom two panels is an average input maps for CCK cells to pyramidal cells in layer four (middle panel, two three pyramidal cells) and in layer 5 (bottom panel, two pyramidal cell) and their corresponding normalized laminar distribution on two right panel.
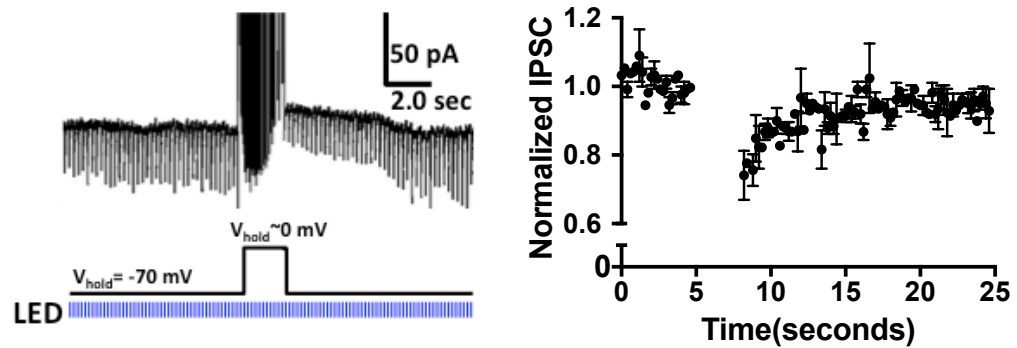
Figure 3.6. Layer 2/3 pyramidal cells exhibit depolarization suppression of inhibition (DSI) following photostimulation of cholecystokinin (CCK) expressing cell. Upper Left panel shows inhibitory postsynaptic currents measured during DSI protocol. Lower left panel depicts DSI protocol in which a postsynaptic pyramidal cell is voltage clamped at -70mV and depolarized to 0 mV for 2 seconds while photostimulating ChR2 expressing CCK cells with a 4 msec laser pulse at 5 Hz. Excitatory currents were blocked with (10 uM CNQX and 20 uM AP-5). Right panel shows normalized IPSC for two layer 2/3 pyramidal cells during DSI protocol. IPSCs were normalized to the average IPSC before pyramidal cell depolarization for each cell. mean±SEM.

CONCLUDING REMARKS

In the last three decades, we have learned a tremendous amount about circuit and function of cortical inhibitory cells using genetically defined cell types. However, during this same time we have also learned that no single trait can accurately define all cell types. More recently, studies have begun to use combinatorial strategies to define cell types based on their gene expression (Tasic et al. 2016), axon morphology (Jiang et al. 2015), electrophysiology and unique connectivity (Kim et al. 2015; Allen and Luo 2015; W. A. Lee et al. 2016). We have learned that there are likely more cell types with unique functional properties and connectivity than previously predicted. The study presented in this dissertation used a novel approach to identify new cell types based on the co-express of two gene products (VIP and CR). We have also introduced technology that has the potential of revealing single cell resolution connectivity maps using Cre-dependent somatodendritic expression of ChR2 and laser scanning photostimulation. The combination of intersectional optogenetics strategies and single cell resolution photostimulation will likely reveal circuits and function of novel cell types with higher specificity and precision.

Future studies

To fully characterize VIP interneuron subtypes identified in Chapter 2, we need to take a similar approach that we took in Appendix A. We should identify higher cortical areas that selectively recruit VIP+/CR+ or VIP+/CR- cells differentially using intersectional rabies virus and ChR2 photostimulation. We can also observe the effect VIP subtypes on cortical function by photoactivating or silencing them during visual stimulation. Understanding the cell type specific

connectivity and function will help reverse engineer the brain to its basic components.

Three years ago president Barack Obama announced a Brain Initiative project stating

that,

> Now, as humans, we can identify galaxies light years away. We can study particles smaller than an atom, but we still haven't unlocked the mystery of the three pounds of matter that sits between our ears. But today, scientists possess the capability to study individual neurons and figure out the main functions of certain areas of the brain. But a human brain contains almost 100 billion neurons, making trillions of connections.

How has the community answered this calling? By bringing together neuroscientist,

engineers, and physicians to develop technology that will push the boundaries of

discovery and allow for the formulation of new hypothesis. This is more evidenced by

the work presented in this dissertation.

APPENDIX A:

Genetic Targeting Reveals Three Types of Cortical L5 Neurons that Differ in Brain-Wide Connectivity and Function

PREFACE TO APPENDIX A

Appendix A. fits well with the overall dissertation as it describes the electrophysiology, function and connectivity of layer 5 excitatory cell types in mouse visual cortex. Until recently, layer 5 pyramidal neurons in the visual cortex were thought to be composed of only two distinct excitatory cell types, thin-tufted, cortico-cortical pyramidal cells and thick-tufted, cortico-subcortical pyramidal cells. Results presented in Appendix A suggest that there are in fact, three distinct layer 5 pyramidal cell types in mouse visual cortex that differ in their long distance projection pattern, visual response, and intrinsic electrophysiology. Similar to Chapter 2, the work in Appendix A describes how a correlation between connectivity and genetic profiling may reveal novel cell types in mouse visual cortex.

The *in vitro* electrophysiology findings demonstrate that the thin-tufted, cortico-cortical layer 5 pyramidal neuron can be subdivided into two subtypes that differ in membrane voltage dynamics in response to hyperpolarizing current injection, and within group variation in input-resistance and firing pattern. Both subtype of L5-CC thin tufted cells are regular spiking neurons with relatively small soma size, as indicated by the low soma surface area and capacitance (Figure A.2A, Figure A.2D, Table SA.1). However, a subtype of L5-CC cells that do not project to striatum exhibits high percent sag and amplitude, similar to thick-tufted layer 5 cortical-

subcortical (CS) pyramidal neuron. Close inspection of other electrophysiological parameters reveals large cell-to-cell variability in input-resistance and in firing pattern for L5 CC-NS measured the by coefficient of variation (CV, defined as standard deviation divided by the mean). CV in input-resistance among L5 CC-NS cells was 2 fold larger than L5-CS and L5-CC (0.60 L5-CC-NS, 0.33 L5-CS, 0.23 L5-CC calculated from Table SA.1). Furthermore, the spike train pattern (ratio of initial interspike interval to mean interspike interval) following injection of depolarizing current is also largely variable within the L5-CC-NS population with CV (0.58 L5-CC-NS, 0.40 L5-CS, 0.17 L5-CC). The results suggest that these two subtypes of L5-CC (L5-CC vs. L5 CC-NS) may have distinct functional role in processing sensory information in mouse visual cortex. The (Kim et al. 2015) study further characterizes *in vivo* physiology and long range input to these three distinct cells types using rabies viral tracing (Wall et al. 2010; Wickersham et al. 2007).

SUMMARY

Cortical layer 5 (L5) pyramidal neurons integrate inputs from many sources and distribute outputs to cortical and subcortical structures. Previous studies demonstrate two L5 pyramid types: cortico-cortical (CC) and cortico-subcortical (CS). We characterize connectivity and function of these cell types in mouse primary visual cortex and reveal a new subtype. Unlike previously described L5 CC and CS neurons, this new subtype does not project to striatum [cortico-cortical, non-striatal (CC-NS)] and has distinct morphology, physiology and visual responses. Monosynaptic rabies tracing reveals that CC neurons preferentially receive input from higher visual areas, while CS neurons receive more input from structures implicated in top-down

modulation of brain states. CS neurons are also more direction-selective and prefer faster stimuli than CC neurons. These differences suggest distinct roles as specialized output channels, with CS neurons integrating information and generating responses more relevant to movement control and CC neurons being more important in visual perception.

INTRODUCTION

The cerebral cortex is populated by numerous types of excitatory and inhibitory neurons. Excitatory pyramidal neurons (PNs) are the source of nearly all cortical outputs and thus play an essential role in mediating interactions between brain areas. In contrast, cortical inhibitory neurons make primarily local connections and modulate cortical outputs. Many studies have capitalized on cell type specific mouse lines to explore the diversity of inhibitory neuron types and their unique roles in cortical computations (Adesnik et al., 2012; Fu et al., 2014; Lee et al., 2013; Lee et al., 2012; Nienborg et al., 2013; Taniguchi et al., 2011; Wilson et al., 2012). In contrast, mouse lines for exploring the diverse contributions of different types of cortical PNs have only recently become available (Gerfen et al., 2013; Gong et al., 2007; Li et al., 2015; Olsen et al., 2012). These lines have been used to investigate the functional properties and connections of layer 6 PN types (Kim et al., 2014; Olsen et al., 2012; Vélez-Fort et al., 2014), but most previous studies of layer 5 (L5) PN types have relied on more conventional cell targeting approaches (but see Li et al., 2015). Here we identify and use mouse lines expressing Cre recombinase selectively in subtypes of L5 PNs to facilitate experiments using modern molecular, genetic, and viral tools to link distinct cell types to brain-wide connectivity and function in the visual cortex.

Previous studies of L5 PNs have revealed key details about the long-distance projections, morphology, intrinsic physiological properties, and local inputs of two major cell classes: Cortico-cortical (CC) and cortico-subcortical (CS). Importantly, CC PNs (often referred to as L5A or intratelencephalic) project to other cortical areas whereas CS neurons (L5B or pyramidal tract) project to subcortical structures including superior colliculus, thalamus, and brainstem (Bourassa and Deschenes, 1995; Groh et al., 2010; Hallman et al., 1988; Hattox and Nelson, 2007; Hubener and Bolz, 1988; Hubener et al., 1990; Kasper et al., 1994; Tsiola et al., 2003; Zarrinpar and Callaway, 2014). Both CC and CS L5 neurons project to the striatum (Cowan and Wilson, 1994; Levesque et al., 1996). L5 CC PNs have a relatively simple apical dendritic tuft, thin apical dendrite and fire action potentials in regular trains (regular spiking, RS) following somatic current injections (Groh et al., 2010; Larsen, 2008). In contrast, L5 CS PNs have a complex apical dendritic tuft, thick apical dendrite, and are burst spiking (BS) (Groh et al., 2010). These differences suggest that CC and CS neurons likely function as distinct information channels for mediating different perceptual and behavioral demands.

In this study, we take advantage of bacterial artificial chromosome (BAC) Cre-expressing transgenic mouse lines, *in vitro* whole cell recording and dye-filling, viral tracers, and two-photon calcium imaging of visual responses to define and characterize distinct types of layer 5 output neurons in mouse V1. In addition to CC and CS L5 pyramidal neurons, we identify and characterize a third type of L5 pyramidal neuron, which makes some cortico-cortical connections but does not project to striatum (CC-NS). We show that each cell class has unique *in vitro*

electrophysiological and morphological properties. Furthermore, using monosynaptic rabies virus-based tracing methods, we show that CC neurons receive more of their synaptic inputs from higher order visual cortical areas specialized for visual image perception. CS neurons, on the other hand, receive more inputs from structures such as retrosplenial/cingulate cortex and basal forebrain, which are implicated in top-down modulation of brain states. These differences suggest possible functional differences *in vivo* which we evaluated using two-photon calcium imaging to assess visual responses to drifting sine wave gratings. We find that CS neurons are more direction-selective and prefer higher temporal frequency than CC neurons. Furthermore, CC-NS neurons prefer higher spatial frequencies. Our results show that each L5 projection neuron type receives differential brain-wide inputs and extracts different visual information to mediate its specialized functions.

RESULTS

Three classes of layer 5 pyramidal neurons in mouse V1 defined by distinct BAC Cre transgenic mice display different axonal projection patterns

To label distinct layer 5 pyramidal neuron subpopulations in the mouse cortex, we have identified and characterized three BAC Cre transgenic mouse lines obtained from the GENSAT project (Gerfen et al., 2013) (http://www.gensat.org/cre.jsp): Tlx3-Cre PL56, Glt25d2-Cre NF107, and Efr3a-Cre NO108. Cre recombinase expression in adult cortices of these transgenic mice is restricted to subsets of deep layer cortical neurons (Gerfen et al., 2013), consistent with results in the Allen Brain Institute transgenic atlas (http://connectivity.brain-map.org/transgenic).

To investigate the location of Cre expressing neurons in the adult visual cortex and long-distance axonal projections of cortical neurons in each transgenic line, we injected Cre-dependent adeno-associated virus (AAV) that expresses eGFP or tdTomato (AAV-FLEX-eGFP (or tdTomato)) into the primary visual cortex (V1) of Tlx3-Cre, Glt25d2-Cre, or Efr3a-Cre mice at post-natal day 60 (P60) and harvested brains at post-injection day 21. Cell bodies expressing eGFP (or tdTomato) are located exclusively in subsets of L5 PNs in Tlx3-Cre and Glt25d2-Cre lines; in the Efr3a-Cre line cell bodies are located in both layer 5 and 6 (Figure A.1A), confirming that these three mouse lines express Cre in subsets of deep layer cortical neurons. eGFP$^+$ Tlx3-Cre$^+$ neurons in V1 project their axons densely and predominantly to adjacent visual cortical areas such as V2L, V2ML and V2MM, as well as further cortical regions including other sensory cortices, frontal cortices, and contralateral visual cortex (Figures 1A,B and S1A-C). This suggests that Tlx3-Cre selectively labels L5 CC PNs. eGFP$^+$ axons from Tlx3-Cre$^+$ neurons were not found in any subcortical structures with the exception of the striatum, a known target of axon collaterals from CC neurons (Figure A.1B) (Levesque et al., 1996). In contrast, eGFP$^+$ axons from Glt25d2-Cre$^+$ neurons in V1 do not project to other cortical areas (Figures 1A,B). Instead, their axons enter white matter and travel to target subcortical structures including the superior colliculus, lateral posterior (LP) and lateral dorsal (LD) nuclei of thalamus, pons, and ipsilateral striatum (Figures 1B and S1D-O). These axonal projections suggest Glt25d2-Cre selectively labels L5 CS PNs. We also labeled L5 CS PNs in V1 by injecting retrogradely infecting Cav2-Cre virus into the superior colliculus and AAV-FLEX-eGFP into V1. Layer 5 neurons labeled by Cre expression in the

Glt25d2-Cre mouse line and those labeled following Cav2-Cre injection to superior colliculus exhibit similar cell body locations and axon target profiles (Figures 1A,B). We conclude that although Glt25d2-Cre^{+} neurons are sparse, they are a representative sample of CS neurons.

Notably, Efr3a-Cre[+] layer 5 (L5) V1 neurons lack projections to known axonal targets of layer 5 CC and CS neurons such as: superior colliculus, thalamus, brainstem, and striatum (Figure A.1B). Efr3a-Cre^{+} neurons do project to other adjacent cortical areas, a target they share in common with layer 5 CC neurons. Dense eGFP[+] labeled long distance axons are also found in known layer 6 neuron targets, including the dorsal lateral geniculate nucleus (dLGN), LD, and LP of thalamus (Figures 1B and S1J-O). In LP, a shared target region of layer 5 and 6 neurons, axon terminals of Efr3a-Cre^{+} neurons are thin and small type I morphology, distinct from the thick and large type II morphology of Glt25d2-Cre^{+} neurons (Figures S1P,Q) (Li et al., 2003). The presence of labeled neurons in both layer 5 and 6 of Efr3a-Cre mice makes it less straightforward to study the projections of L5 Efr3a-Cre^{+} neurons in isolation. However, several lines of evidence detailed below indicate that L5 Efr3a-Cre^{+} neurons do not project to the thalamus and that they include both local pyramids (not projecting out of V1) and projection neurons. Since the only targets of Efr3a-Cre^{+} neurons that are known to receive input from L5 rather than L6 are adjacent cortical areas (see above), L5 Efr3a-Cre^{+} neurons must include CC projection neurons and might therefore represent a sub-group of CC neurons. Despite the fact that both L5 Efr3a-Cre^{+} neurons and Tlx3-Cre^{+} CC cells share a common extrinsic target (adjacent cortical areas), they are clearly distinct and non-overlapping groups. In addition to

differences in projections to striatum, as described in further detail below, the morphology and intrinsic physiology of L5 Efr3a-Cre^{+} neurons further distinguish them from Tlx3-Cre^{+} CC cells.

To determine whether LP projecting Efr3a-Cre^{+} V1 neurons are in L5, cholera toxin subunit B conjugated to Alexa Fluor 594 (a retrograde tracer) was injected into LP of Efr3a-Cre mice (Figure SA.1R), while AAV-FLEX-eGFP was injected in V1. Although many Alexa Flour 594 labeled neurons were found in L5, none were eGFP[+] L5 Efr3a-Cre^{+} neurons, indicating an absence of projections to LP (Figures S1S,T). Further, in line with a previous study demonstrating that L5 neurons in mouse primary visual cortex do not project to dLGN (Bortone et al., 2014), L5 Efr3a-Cre^{+} neurons do not project to thalamus. To trace the axons of single L5 Efr3a-Cre^{+} neurons, we partially reconstructed sparsely labeled neurons (see Experimental Procedures, Figure SA.2B). The main descending axons of all cells were reconstructed far enough to unambiguously determine whether they extended into the white matter or clearly ended before reaching the white matter. Results from axonal reconstructions demonstrate that 8 of 15 L5 Efr3a-Cre^{+} neurons are local pyramids (Figure A.1C, left panel), whereas 7 of 15 neurons project out of V1 (Figure A.1C, right panel) and presumably continue to nearby cortical areas, as these are the only regions other than the thalamus in which axons are seen following bulk labeling (Figure A.1A). Note that the long distance projections of Efr3a-Cre^{+} neurons also differ from both Tlx3-Cre[+] and Glt25d2-Cre^{+} neurons in that no eGFP labeling is seen in the striatum (Figure A.1B). These results are consistent with evidence for three distinct classes of L5 PNs (Figure A.1D)

Morphological and electrophysiological characterization indicates labeling of three distinct layer 5 pyramidal neuron populations

We further investigated whether L5 PNs defined by Tlx3-Cre, Glt25d2-Cre, and Efr3a-Cre are distinct morphologically and/or physiologically. First, we characterized their soma and proximal dendrite morphology using confocal microscopy after AAV-FLEX-eGFP injection into V1 (Figure A.2A). In terms of both soma size and apical dendrite diameter, Tlx3-Cre^{+} neurons (n=16) are significantly smaller than Glt25d2-Cre^{+} neurons (n=39) (soma size (μm^2): 68.60 ± 2.72 versus 124.0 ± 4.67, respectively, apical dendrite diameter (μm): 1.40 ± 0.14 versus 2.67 ± 0.18, respectively; mean ± SEM, one-way ANOVA with Tukey's post-hoc test, $p<0.0001$, Figures 2A,B). The soma size and apical dendrite diameter of L5 Efr3a-Cre^{+} neurons (n=97, soma size: 64.29 ± 1.58 μm^2, apical dendrite diameter: 1.43 ±

. Despite these similarities between Tlx3-Cre[+] and Efr3a-Cre^{+} neurons, other morphological features clearly distinguished the two populations. Upon careful visual inspection, L5 Efr3a-Cre^{+} cells have a different soma shape from Tlx3-Cre[+] or Glt25d2-Cre^{+} cells: Efr3a-Cre[+] cell somata (n=21) have an oval appearance whereas0.16 μm) are also significantly smaller than Glt25d2-Cre^{+} neurons (one-way ANOVA with Tukey's post-hoc test, $p<0.0001$). These differences between Glt25d2-Cre^{+} neurons and both Tlx3-Cre[+] and Efr3a-Cre^{+} neurons were expected based on previous comparisons of CC and CS cells (Groh et al., 2010; Kasper et al., 1994; Larkman et al., 1988). In contrast, there was no difference between soma sizes and
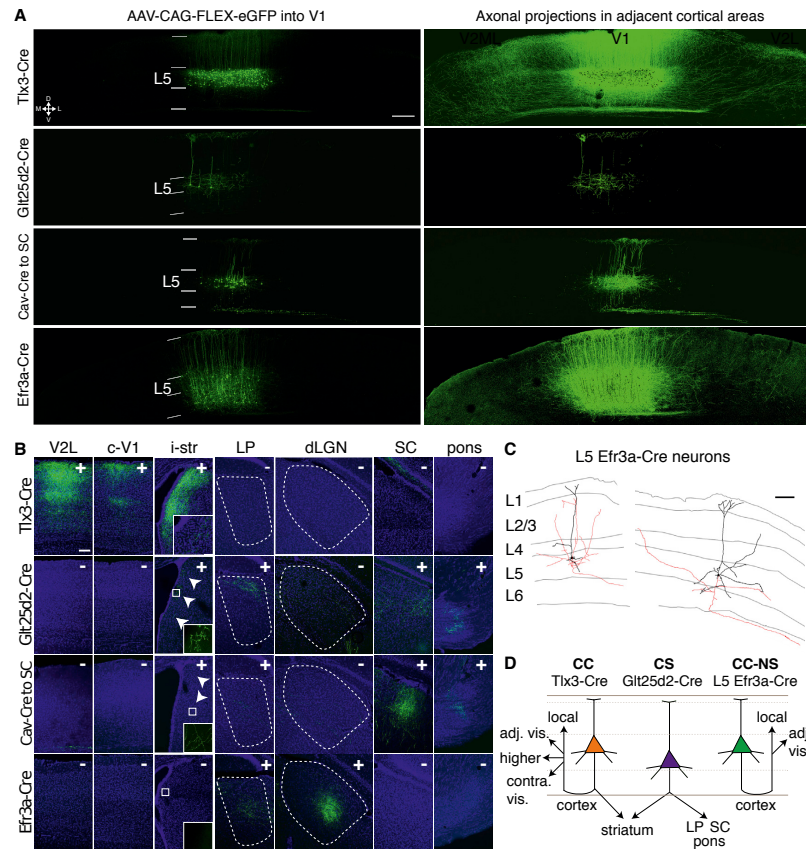
Figure A.1. Three Distinct Classes of Layer 5 Pyramidal Neurons Defined by BAC Cre Transgenic Lines Exhibit Distinct Long Distance Axonal Projection Patterns. (A) Coronal sections showing eGFP labeled neurons after AAV-FLEX-eGFP (or tdTomato) injection into the primary visual cortex of three BAC transgenic Cre mice, Tlx3-Cre PL56, Glt25d2-Cre NF107, Efr3a-Cre NO108 or C57BL/6 mouse injected with Cav2-Cre virus into the superior colliculus (SC). Left and right panels for each condition correspond to photographs of the same fields of view but with the panels to the left imaged at lower brightness to illustrate dendritic morphology and cell body locations and right panels at higher brightness to better reveal axonal projections. (B) Axonal projections of eGFP[+] labeled V1 Cre^{+} neurons to V2L, contralateral V1, ipsilateral striatum (i-str), thalamic nuclei LP and dLGN, superior colliculus (SC), and pons. Inset in i-str panel of Tlx3-Cre: contralateral striatum. Insets in i-str panels of Glt25d2-Cre and Cav2-Cre to SC: magnified images. '+' or '-' indicates presence or absence of GFP[+] axons in each panel. (C) Partial reconstructions of L5 Efr3a-Cre^{+} neurons using Neurolucida. Dendrites: black; axons: red. (D) Schematic representation illustrating three different Cre[+] subpopulations of layer 5 neurons projecting their axons to different structures. Abbreviations: CC, cortico-cortical; CC-NS, cortico-cortical non-striatal; CS, cortico-subcortical; dLGN, dorsal lateral geniculate nucleus; i-str, ipsilateral striatum; L5, layer 5; LP, lateral posterior thalamic nucleus; SC, superior colliculus; V1, primary visual cortex; V2L, secondary visual cortex, lateral area. Scale bars = 200 μm (A), 100 μm (B, C).

apical dendrite diameters between Tlx3-Cre[+] and Efr3a-Cre^{+} neurons (Figures 2A,B). Tlx3-Cre[+]and Glt25d2-Cre[+] cell somata (n=13 and n=15, respectively) appear more pyramidal (Figure A.2A).We quantified this by measuring the height and width of each cell and determining the height over width ratio (H/W) as a parameter of cell body shape. L5 Efr3a-Cre^{+} neurons have significantly higher H/W ratios than Tlx3-Cre^{+} neurons (1.20 ± 0.06 and 0.83 ± 0.04, respectively, one-way ANOVA with Tukey's post-hoc test, p<0.001, Figure A.2B), indicating that Tlx3-Cre[+] and L5 Efr3a-Cre^{+} neurons are morphologically different. Furthermore, the greatest H/W ratio for the Tlx3-Cre^{+} neurons was 1.03, while 15 of 21 (71.43%) of the L5 Efr3a-Cre^{+} neurons had larger ratios indicating that there is less than 30% overlap between these distributions and that the two populations are largely distinct based solely on this single morphological feature.

Next, we measured intrinsic membrane properties of the three L5 PN populations to test whether they exhibit distinct electrophysiological characteristics. To perform whole-cell patch-clamp analysis, we prepared acute brain slices of P28-P50 visual cortex from Tlx3-Cre, Glt25d2-Cre, and Efr3a-Cre mice after they were either crossed with Ai14 (Cre reporter line expressing tdTomato upon Cre-mediated recombination; Madisen et al., 2012) or injected with AAV-FLEX-eGFP (or tdTomato). Near threshold depolarizing current pulses injected to the cell bodies under current clamp conditions revealed that all Tlx3-Cre^{+} neurons (17 of 17) and most L5 Efr3a-Cre^{+} neurons (7 of 9) are regular spiking, while all Glt25d2-Cre^{+} neurons (11 of 11) are intrinsically bursting (see Experimental Procedures), as expected from previous desc-

Figure A.2. Morphological and Electrophysiological Properties of Three Types of Layer 5 Pyramidal Neurons. (A) Confocal images displaying soma and proximal dendrites of eGFP[+] Tlx3-Cre[+], Glt25d2-Cre[+] and L5 Efr3a-Cre^{+} neurons. (B) Dendritic and cell body morphologies of Tlx3-Cre[+], Glt25d2-Cre[+] and L5 Efr3a-Cre^{+} neurons differ in cell soma size (μm^2), apical dendrite diameter (μm) at the base, and height over width (H/W) ratio. (C) Examples of action potential trains evoked by 200 pA current injections into Tlx3-Cre[+], Glt25d2-Cre[+], and L5 Efr3a-Cre^{+} neurons. (D) Intrinsic electrical property differences in (left) percent sag (%), (middle) input resistance (MΩ) and (right) interspike interval at initial over interspike interval at steady state phase of Tlx3-Cre[+], Glt25d2-Cre[+] and L5 Efr3a-Cre^{+} neurons. Values are reported as means ± SEM for each class of neurons. Statistics were calculated from one-way ANOVAs followed by Tukey's post-hoc tests to compare means of pairs of each L5 class. Significant differences between pairs are indicated by the *P* value. *p < 0.05, **p < 0.01, ***p < 0.001, ****p<0.0001. Scale bar = 10 μm (A).

riptions of CC thin-tufted and CS thick-tufted neurons, respectively (Figure A.2C) (Groh et al., 2010; Kasper et al., 1994; Larkman et al., 1988).

Despite the fact that both Tlx3-Cre[+] and L5 Efr3a-Cre^{+} neurons are regular spiking, further analyses revealed that the intrinsic electrical properties of L5 Efr3a-Cre^{+} neurons are distinct from both Tlx3-Cre[+] and Glt25d2-Cre^{+} neurons (Figure A.2D). Analysis of interspike intervals (ISIs) at the onset of current injection divided by the interval at steady state yielded similar values for Tlx3-Cre[+] and L5 Efr3a-Cre^{+} neurons (0.57 ± 0.02 and 0.44 ± 0.09, respectively; mean $\pm$ SEM) both of which are distinct from Glt25d2-Cre^{+} neurons (0.20 ± 0.02, one-way ANOVA with Tukey's post-hoc test, $p<0.0001$ and $p<0.01$ respectively). Input resistance (MΩ) for Tlx3-Cre[+] and Glt25d2-Cre^{+} neurons are similar (120.91 ± 6.68 and 146.37 ± 14.53, respectively). However, L5 Efr3a-Cre^{+} neurons exhibit significantly higher input resistances than the other two cell types (263.37 ± 52.72, one-way ANOVA with Tukey's post-hoc test, $p<0.05$ to Glt25d2-Cre[+] and $p<0.001$ to Tlx3-Cre^{+} neurons). Although differences in the mean values were observed between cell types for both ISIs and input resistance, there was considerable overlap in the distributions between L5 Efr3a-Cre^{+} neurons and both of the other groups (Figure A.2D).

However, a third measure of intrinsic electrical properties clearly distinguished L5 Efr3a-Cre^{+} neurons from Tlx3-Cre^{+} neurons. Notably, L5 Efr3a-Cre^{+} neurons exhibited significantly higher percent sag (%) than Tlx3-Cre^{+} neurons (20.93 ± 2.05 and 6.57 ± 0.88, respectively. One-way ANOVA with Tukey's post-hoc test, $p<0.0001$), while percent sags for L5 Efr3a-Cre[+] and Glt25d2-Cre^{+} neurons are similar (20.93 ± 2.05 and 22.19 ± 1.34, respectively). Sag amplitudes were also significantly

larger for L5 Efr3a-Cre$^+$ and Glt25d2-Cre$^+$ neurons than for Tlx3-Cre$^+$ neurons (Figure SA.3D). Further details of percent sag measurements can be found in Figure SA.3. Note that there is little overlap in the distributions of percent sag values between L5 Efr3a-Cre$^+$ neurons and Tlx3-Cre$^+$ neurons (Figure A.2D), and no overlap in sag amplitudes (Figure SA.3D), indicating that they are distinct populations. Furthermore, the lack of bursting in both Efr3a-Cre$^+$ and Tlx3-Cre$^+$ neurons distinguishes them from Glt25d2-Cre$^+$ neurons. These physiological features, along with the morphological features described above, indicate that these three mouse lines label three distinct and non-overlapping L5 neuronal populations that must correspond to distinct cell types. Additional electrophysiological characterization, including adaptation indexes and capacitance were also evaluated for all three Cre$^+$ cell groups and can be found in Table SA.1.

Altogether, extensive comparisons among three genotypically defined layer 5 PN populations demonstrate distinct morphological and physiological properties. While the classical measures of intrinsic physiology (RS versus BS) and morphology (thin-tufted versus thick-tufted) are as expected from the distant projections (CC versus CS) of each cell group, L5 Efr3a-Cre$^+$ neurons are clearly distinct from both Tlx3-Cre$^+$ L5 CC PNs and Glt25d2-Cre$^+$ L5 CS PNs. The soma shapes of L5 Efr3a-Cre$^+$ neurons in V1 are more oval, they have 3-fold greater electrical sag than Tlx3-Cre$^+$ CC PNs (with no overlap in their distributions), and they lack projections to the striatum. Furthermore, both Tlx3-Cre$^+$ CC PNs and L5 Efr3a-Cre$^+$ neurons are distinct from Glt25d2-Cre$^+$ L5 CS PNs based on their classical intrinsic firing and dendritic morphological features.

Brain-wide inputs to genetically defined layer 5 pyramidal neurons using monosynaptic rabies virus

To profile brain-wide distributions of neurons directly presynaptic to Tlx3-Cre[+], Glt25d2-Cre[+] and Efr3a-Cre^{+} neurons in V1, we used Cre-dependent tracing with G-deleted rabies virus (RV*dG*) (Figures 3A,B) (Wall et al., 2010; Wickersham et al., 2007). To restrict initial RV*dG* infection to Cre expressing starter neurons in a given region and label monosynaptic input neurons specifically, we used Cre-dependent AAV vectors to express TVA, rabies glycoprotein (G), and GFP selectively in Cre^{+} neurons. TVA is a receptor for the avian sarcoma leucosis virus envelope protein, EnvA, and allows selective infection of Cre[+] "starter" cells with EnvA-pseudotyped RV*dG* (EnvA+RV*dG*). Expression of G in Cre^{+} neurons allows for *trans*-complementation in neurons infected with RV*dG* such that rabies particles can be produced in starter cells and spread to their direct presynaptic inputs. GFP is used to mark cells expressing TVA, facilitating later quantitative analyses. In these experiments, we expressed these three genes in two separate AAV vectors in conjunction with a novel chimeric rabies glycoprotein that mediates more efficient *trans*-complementation and trans-synaptic spread than previous versions (see Experimental Procedures). Furthermore, one of the AAV vectors (AAV-FLEX-G) expresses G alone in order to maximize G expression, further improving *trans*-complementation, and trans-synaptic spread of RV. The second AAV vector (AAV-FLEX-GFP-TVA) expresses both TVA and GFP.

Tlx3-Cre[+], Glt25d2-Cre[+] and Efr3a-Cre[+] mice (>42 days old at the onset of experiments) were first injected at day 0 with a mixture of AAV-FLEX-G and AAV-

FLEX-GFP-TVA into V1. At day 21, EnvA+RV*dG* expressing dsRed (EnvA+RV*dG*-dsRed) was injected at the same location. This resulted in expression of GFP, TVA, G, and dsRed in "starter" cells that were directly infected with EnvA+RV*dG*-dsRed in V1 and expression of only dsRed in distant neurons providing direct monosynaptic input to the starter cells (Figure A.3). At day 28-29, animals were sacrificed, their brains sectioned and stained, and labeling patterns across the whole brain were reconstructed to create maps of the locations of dsRed^{+} input neurons for analysis.

To assess long distance presynaptic neurons to L5 Tlx3-Cre[+], Glt25d2-Cre[+] and L5/6 Efr3a-Cre^{+} neurons of V1, we analyzed every other coronal section of the whole brains from Bregma 2.50 mm to -5.00 mm. Three factors should be considered before analyzing and interpreting long distance presynaptic cells correctly in our paradigm. First, it should be noted that since it was not possible to selectively infect L5 Cre^{+} neurons in Efr3a-Cre mice (unlike Tlx3-Cre and Glt25d2-Cre mice), both L5 and L6 neurons serve as starter neurons (Figure A.3C). Second, low levels of leaky TVA expression are sufficient to mediate direct infection with EnvA+RV*dG*-dsRed and dsRed expression in non-Cre^{+} neurons close to the injection site, however, leak expression of G is not sufficient to mediate *trans*-complementation and trans-synaptic labeling in distant neurons (Figure SA.4) (Miyamichi et al., 2013; Wall et al., 2010). Our virus injection sites were in the center of V1, from -3.3 to -3.5 mm along anterior-posterior axis, and from 2.4 to 2.7 mm along medial-lateral axis from bregma (Figure
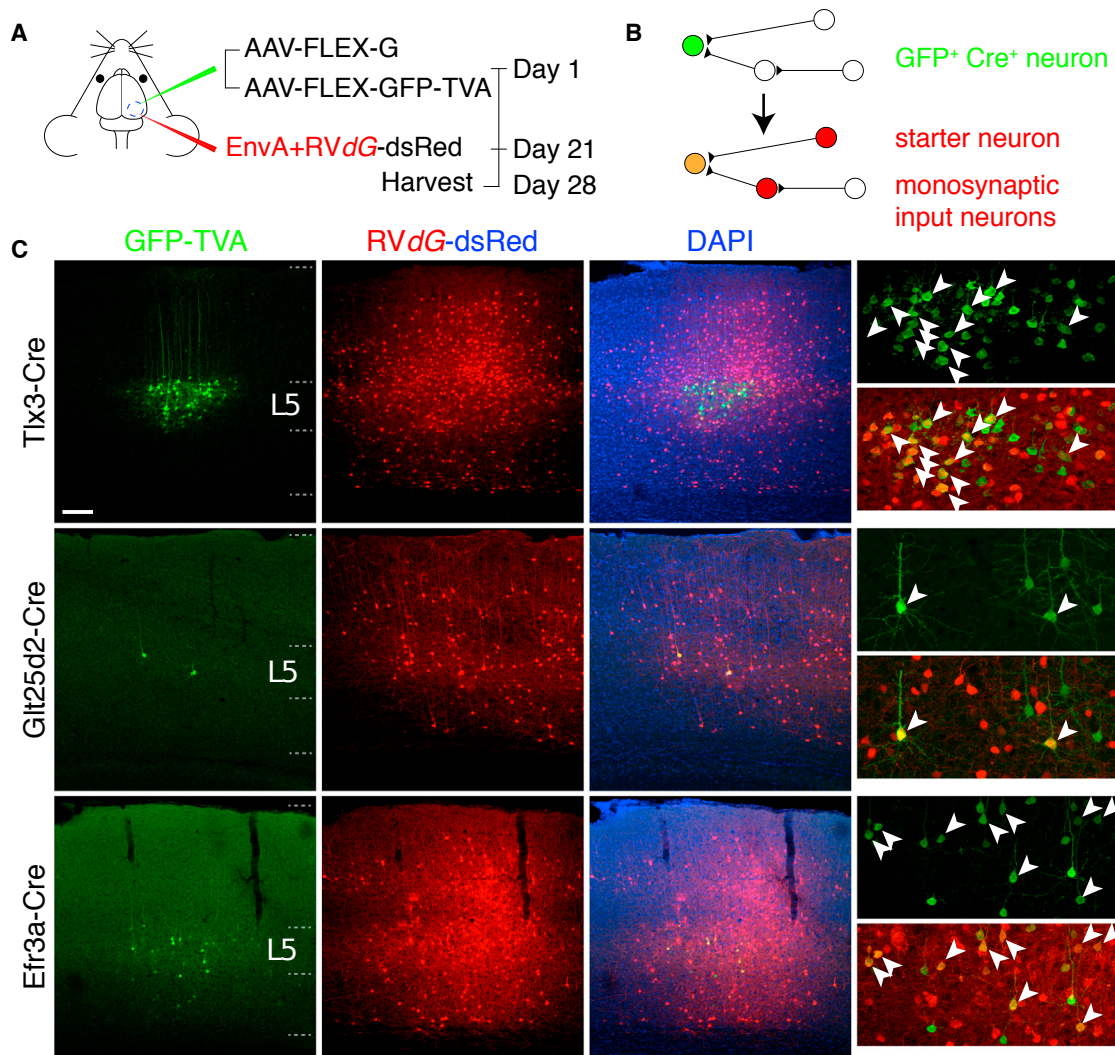
Figure A.3. Monosynaptic Rabies Virus Tracing of Inputs to Layer 5 Pyramidal Neurons. (A) Schematic illustrating virus injection schemes for monosynaptic rabies virus tracing. (B) Schematic illustrating labeling of various neuronal populations following rabies virus-mediated monosynaptic input labeling. (C) Coronal sections of visual cortices of Tlx3-Cre, Glt25d2-Cre, Efr3a-Cre mice showing GFP-TVA[+], dsRed[+] starter neuron locations. Scale bar = 100 μm (C).

A.4A). The adjacent visual cortical areas closest to these injections are more than 1mm away and beyond the zone where direct infection of neurons with leaky TVA expression could confound results (Figures 4A and S4A). Therefore, this caveat should not affect our long-distance monosynaptic input mapping.

Third, each brain in each transgenic mouse group has different starter cell numbers and differs in total numbers of input neurons (Figure SA.4B). In order to make direct statistical comparisons between experiments and between transgenic lines, here we report the percentage of input in any given region over total number of input neurons across the entire brain (excluding local input neurons in V1). We counted and registered dsRed$^+$ input neurons to the smallest possible subregion referenced in the Paxinos mouse atlas (Paxinos et al., 2001). We also used nuclear DAPI (4',6-diamidino-2-phenylindole) counterstaining and autofluorescence background to identify various anatomical boundaries to ensure input neurons were assigned to the correct structures (see Experimental Procedures). To directly compare the proportions of inputs from each area across mouse lines, we assigned input neurons to 16 regions. These include 10 cortical subdivisions: visual (including V2L, V2ML and V2MM), retrosplenial/cingulate, auditory, somatosensory, motor, parietal, orbital, ventral-associated cortical areas, para-hippocampal area; 4 thalamic subdivisions: dLGN, LP, LD, other thalamic areas; and the basal forebrain and other areas including striatum, amygdala and hypothalamus (See Table SA.2). Neurons in visual cortical areas were assigned to V2L, V2ML and V2MM rather than their smaller subdivisions (e.g. P, POR, LM, AL, RL, AM, PM, M) because only the larger regions can be reliably identified using postmortem anatomical criteria. Smaller subdivisions encompassed by

V2L are likely to include RL, AL, LI, LM, P and POR. Similarly, V2ML and V2MM likely include AM, PM and M (Garrett et al., 2014).

Cortical inputs to CC and CS PNs in V1

Figure A.4N summarizes long range input profiles onto Tlx3-Cre[+], Glt25d2-Cre[+] and Efr3a-Cre^{+} V1 neurons. All three Cre[+] populations in V1 received more input from extrastriate visual areas than any other structure (Figures 4A,N). Other relatively strong long-range cortical inputs were found in retrosplenial, cingulate, auditory and somatosensory cortices (both primary and secondary regions; Figures 4A-C,N). There were smaller numbers of input neurons found in higher cortices such as parietal, orbital, motor and ventral associational cortex (including temporal association cortex, entorhinal, ectorhinal, perirhinal cortex) and para-hippocampal areas (Figures 4D-E, N). These results indicate the presence of direct feedback from many higher association areas to V1 in the mouse, without the necessity for transfer through intermediate higher sensory cortical areas.

Although these overall input trends were similar across Tlx3-Cre[+], Glt25d2-Cre[+] and Efr3a-Cre[+] mice, there were significant differences between mouse lines. Extrastriate visual areas provide a significantly higher proportion of the inputs to Tlx3-Cre[+] and Efr3a-Cre^{+} neurons ($54.65 \pm 1.48\%$ and $51.50 \pm 3.16\%$ respectively) than to Glt25d2-Cre^{+} neurons ($35.94 \pm 1.21\%$, two-way ANOVA with Tukey's post-hoc test, $p<0.0001$) (Figure A.4N). In contrast, Glt25d2-Cre^{+} V1 neurons receive a higher proportion of their inputs from retrosplenial and cingulate cortices than do Tlx3-Cre[+] and Efr3a-Cre^{+} V1 neurons ($23.59 \pm 3.49\%$, $13.38 \pm 1.29\%$ and $16.33 \pm 2.90\%$ respectively, two-way ANOVA with Tukey's post-hoc test, $p<0.0001$

(Glt25d2-Cre$^+$ vs. Tlx3-Cre$^+$) and p<0.01 (Glt25d2-Cre$^+$ vs. Efr3a-Cre$^+$) (Figure A.4N).

Thalamic inputs to CC and CS PNs in V1

We next examined long-range inputs from thalamic areas, the most prominent subcortical input source to all three Cre$^+$ L5 neuronal populations in V1, ranging from 12% to 30% of total inputs (Figures 4H-J, N and S5D-G). Among thalamic areas, dLGN functions as the primary relay from the retina to V1 (Grubb and Thompson, 2003). While the axons of LGN neurons primarily target cortical layer 4, there are also substantial projections to layers 1 and 5, and L5 PNs have dendritic branches in all of these locations. hus, it is not surprising that previous physiological and anatomical Thus , it is not surprising that previous physiological and anatomical studies have demonstrated direct dLGN input to L5 PNs (Constantinople and Bruno, 2013; Ferster and Lindstrom, 1983). To our knowledge, it is not known whether different types of L5 V1 neurons receive different proportions of dLGN inputs. Our trans-synaptic rabies tracing showed that Glt25d2-Cre$^+$ neurons receive a much higher proportion of dLGN input (21.57 ± 4.81%) compared to Tlx3-Cre$^+$ and Efr3a-Cre$^+$ neurons (8.85 ± 0.67% and 10.32 ± 2.39% respectively, two-way ANOVA with Tukey's post-hoc test, p<0.0001). Rabies tracing data for Tlx3-Cre$^+$ and Glt25d2-Cre$^+$ neurons also showed that both CC and CS L5 neurons receive substantial proportions of their direct input from secondary visual thalamic nuclei, LD and LP. In addition, all three Cre$^+$ L5 PN groups in V1 reliably receive small numbers of labeled inputs from various epithalamic nuclei as well as secondary thalamic nuclei for other sensory modalities, such as Po (Figures S5D-G).
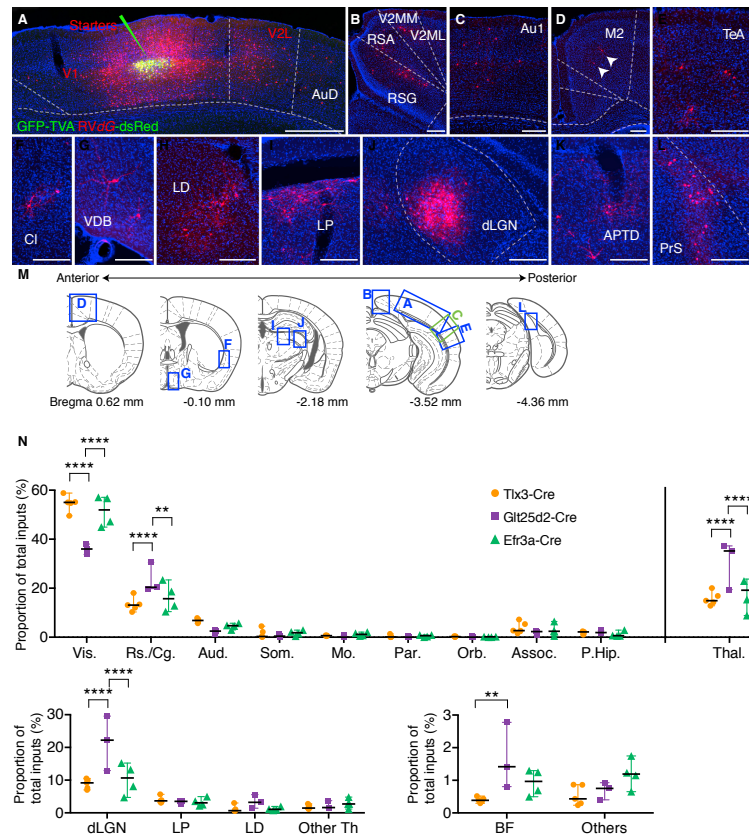
Figure A.4. Brain-Wide Monosynaptic Input to Layer 5 Pyramidal Neurons Revealed by Monosynaptic Rabies Virus Tracing. (A-L) Coronal sections of a rabies virus labeling in Tlx3-Cre[+] mice showing GFP-TVA[+], dsRed^{+} starter neurons and local inputs in V1 (A) and long-distance inputs from V2L and AuD (A), V2MM, V2ML, RSA, and RSG (B), Au1 (C), M2 (D), TeA (E), Cl (F), VDB (G), LD (H), LP (I), dLGN (J), APTD (K) and PrS (L). (M) Coronal section diagrams along the anterior-posterior axis illustrating locations of anatomical regions shown in A-L. Note that the diagrams were chosen for illustration purposes and do not necessarily correspond exactly to figures. (N) Summary of long-range monosynaptic inputs onto Tlx3-Cre[+], Glt25d2-Cre[+], Efr3a-Cre^{+} neurons in the primary visual cortex. Statistics were calculated from two-way ANOVAs with Tukey's post-hoc tests. Significant differences between pairs are indicated by the *P* value. *p < 0.05, **p < 0.01, ***p < 0.001, ****p<0.0001. Abbreviations are: APTD, anterior pretectal nucleus, dorsal part; Au1, primary auditory cortex; AuD, secondary auditory cortex, dorsal area; BF, basal forebrain; Cl, claustrum; dLGN, dorsal lateral geniculate nucleus; LD, laterodorsal thalamic nucleus; LP, lateral posterior thalamic nucleus; M2, secondary motor cortex; PrS, presubiculum; RSA, retrosplenial agranular cortex; RSG, retrosplenial granular cortex; V1, primary visual cortex; VDB, nucleus of the vertical limb of the diagonal band; V2L, secondary visual cortex, lateral; V2ML, secondary visual cortex, mediolateral area; V2MM, secondary visual cortex, mediomedial area; TeA, temporal association cortex. Scale bars = 500 μm (A), 200 μm (B-L).

Other subcortical inputs to CC and CS PNs in V1

In addition to cortical and thalamic inputs, L5 PNs in V1 received direct long-range inputs from basal forebrain (Figures 4G,N). The basal forebrain is composed of diverse neuronal types including cholinergic neurons that project to cortex to modulate brain states such as arousal and wakefulness. Interestingly, Glt25d2-Cre$^+$ neurons receive a significantly higher proportion of their inputs from the basal forebrain compared to Tlx3-Cre$^+$ neurons (1.67 ± 0.58% and 0.40 ± 0.04% respectively, two-way ANOVA with Tukey's post-hoc test, p<0.01).

By examining direct presynaptic neurons throughout the whole brain, we have also observed monosynaptic inputs to V1 from various unexpected anatomical structures, which have not been described in previous studies. These structures include caudate putamen and lateral globus pallidus in the striatum, the medial amygdaloid nucleus, and posterior or lateral hypothalamic areas (Figures S5A-C).

Most cortical inputs to V1 L5 CC and CS PNs originate from other L5 PNs

We next investigated the laminar distributions of long-range cortical input neurons to L5 V1 neurons. While many previous studies have investigated the laminar locations of neurons making feedforward or feedback cortical connections, and other studies have documented the laminar termination patterns of cortical projections, we are not aware of any studies investigating the laminar sources of inputs to neurons located in a particular cortical layer or of a particular PN type. We therefore analyzed the laminar locations of rabies-labeled cortical neurons in Tlx3-Cre, Glt25d2-Cre and Efr3a-Cre mice. Figure A.5A shows the laminar pattern of input neurons in visual cortical area V2ML following rabies virus injections into V1 of a Tlx3-Cre$^+$ mouse.

We found dsRed[+] rabies-labeled neurons in all layers except L1. Across the three Cre[+] lines, for cortical neurons pooled from all cortical areas, the majority of long-range input neurons are located in L5 (53.05 ± 1.47% for Tlx3-Cre[+], 65.93 ± 0.74 % for Glt25d2-Cre[+] and 56.46 ± 1.46% for Efr3a-Cre^{+} neurons; mean ± SEM, Figure A.5B). Laminar bias of input neurons to L5 is even more striking in retrosplenial and cingulate cortices that modulate top-down processes; 69.31 ± 5.91% of input neurons from medial cortices such as retrosplenial and cingulate cortices to Tlx3-Cre^{+} V1 neurons are located in L5, whereas few L2/3 neurons in retrosplenial and cingulate cortices make monosynaptic connections to L5 neurons in V1 (10.06 ± 4.09%, Figure A.5E). It is also notable that 8.64 ± 1.63% of long-range input neurons are from L4 (Figures 5B-D). Studies of L4 excitatory neurons in primary sensory cortices have emphasized their roles as recipients of thalamocortical inputs, and in projecting locally to layer 2/3 without providing long-distance outputs (Douglas and Martin, 2004). This result reveals that at least some L4 neurons participate in long-range cortical-cortical connections. All three Cre[+] neuronal populations show considerable similarities in terms of laminar distribution of long-range input neurons. This suggests that cell-type specific connectivity between long-range connections might be based on soma locations along layers rather than their axonal projection specificity. Together, our findings provide anatomical evidence for layer-specific long distance connection specificity at a cellular level.
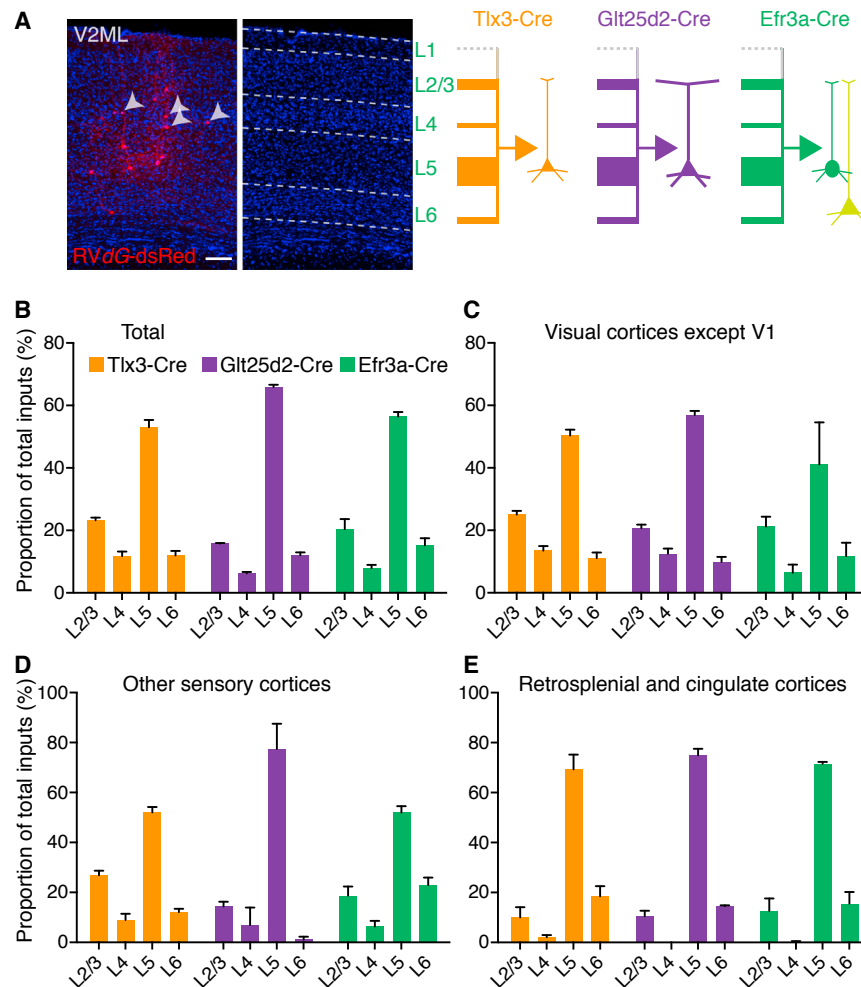
Figure A.5. Laminar Distributions Long-Range Cortical Inputs onto Layer 5 Pyramidal Neurons. (A) An example coronal section showing laminar distribution of dsRed[+] rabies traced input neurons in V2ML onto Tlx3-Cre^{+} V1 neurons. Arrowheads indicate dsRed^{+} presynaptic neurons in L4. (A, right panel) Schematic illustrating relative proportions of input neurons from each layer as thickness of arrows for Tlx3-Cre[+], Glt25d2-Cre[+] and Efr3a-Cre[+] mice. (B-E) Laminar distributions of long-range cortical inputs onto Tlx3-Cre[+], Glt25d2-Cre[+], Efr3a-Cre^{+} V1 neurons as proportions of total cortical inputs (%) for all cortical areas (B), visual cortices except V1 (C), other sensory cortices (D) and retrosplenial and cingulate cortices (E). Abbreviations are V1, primary visual cortex; V2ML, secondary visual cortex, mediolateral area. Scale bar = 100 μm (A).

Visual response properties of cortical versus subcortical projecting layer 5 neurons

Because L5 CC, CC-NS and CS PNs send their outputs to different structures it is likely that they process different types of visual information. We therefore took advantage of the Tlx3-Cre, Glt25d2-Cre, and Efr3a-Cre mouse lines to investigate *in vivo* functional properties of L5 CC. CC-NS and CS PNs in V1. Visual response properties were characterized based on two-photon imaging of calcium dynamics in stationary, awake mice (Figure A.6A). We expressed the calcium indicator GCaMP6 and tdTomato in subsets of CC, CC-NS or CS L5 PNs by injecting a 2:1 mixture of AAV-FLEX-GCaMP6 and AAV-FLEX-tdTomato in V1 of each Cre transgenic mouse (Figures 6B-C). Figure A.6B displays a z-stack of two-photon microscope images from GCaMP6 and TdTomato expressing L5 CS PNs in V1 of a Glt25d2-Cre mouse; cell bodies can be clearly distinguished as well as their apical dendrites extending through the cortical depth up to the pia
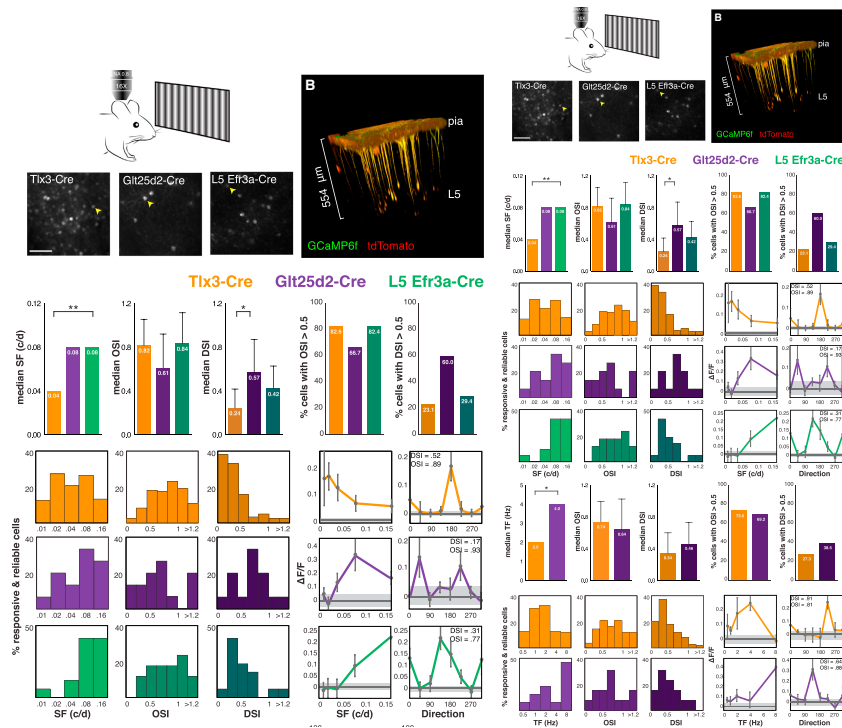
Figure A.6. Visual Responses of Layer 5 Pyramidal Neurons Assayed with Two-Photon Calcium Imaging. (A) Schematic illustration of two-photon in vivo calcium imaging set up for awake and head-fixed stationary mouse. (B) Two-photon microscope z-stack projection of Glt25d2-Cre[+] mouse V1 after AAV-FLEX-GCaMP6 and AAV-FLEX-tdTomato injection. (C) Representative images of single cells expressing GCaMP6 in V1 of Tlx3-Cre[+], Glt25d2-Cre[+], Efr3a-Cre[+] mice. Arrowheads indicate cells plotted in (D) and (E). Scale bar = 100 μm. (D) Spatial Frequency (SF) Experiments. Top: Medians for preferred SF, OSI and DSI (with interquartile ranges for OSI and DSI, at the preferred SF) for Tlx3-Cre[+], Glt25d2-Cre[+], L5 Efr3a-Cre^{+} neurons, as well as the percentage of cells with OSI or DSI > 0.5. Bottom left: Distributions of preferred SF, OSI and DSI (at the preferred SF) for Tlx3-Cre[+], Glt25d2-Cre[+], and L5 Efr3a-Cre^{+} neurons. Bottom right: SF and orientation tuning curve examples for each cell type. Values plotted as means ± SEM. Gray lines indicate average responses during blank stimulus; shading is ± SEM. (E) Temporal Frequency (TF) Experiments. Top: Medians with interquartile ranges for preferred TF, OSI and DSI (at the preferred TF) for Tlx3-Cre[+] and Glt25d2-Cre^{+} neurons, as well as the percentage of cells with OSI or DSI > 0.5. Bottom left: Distributions of preferred TF, OSI and DSI (at the preferred TF) for Tlx3-Cre[+] and Glt25d2-Cre^{+} neurons. Bottom right: Temporal frequency (TF) and orientation tuning curve examples for each cell type. Values plotted as means ± SEM. Gray lines indicate average responses during blank stimulus; shading is ± SEM. For median plots, statistical significances are labeled as p values after Wilcoxon rank-sum test (TF experiments) or Kruskal-Wallis test with Dunn's multiple comparisons test as post-hoc (SF experiments). *p < 0.05 and **p < 0.01. Abbreviations: c/d, cycle per degree; Hz, Hertz.

To assess tuning properties, two different stimulation paradigms were used. To quantify spatial frequency (SF) tuning, drifting sine wave gratings were varied over five different SFs (0.01 to 0.16 c/d) and eight different directions while temporal frequency (TF) was kept constant at 1 Hz. To quantify TF tuning, gratings were presented at five different TFs (0.05 to 8 Hz) and eight directions while SF was kept constant at 0.04 cycles per degree (c/d). Using these paradigms, we generated tuning curves for SF, TF, and orientation/direction (at best SF or TF) for Tlx3-Cre[+], Glt25d2-Cre[+] and L5 Efr3a-Cre^{+} neurons (Figures 6D-E, right panels).

For neurons that were visually responsive and reliable (see Experimental Procedures), various indices were calculated: orientation selectivity (OSI), direction selectivity (DSI), preferred SF, and preferred TF (Figures 6D-E). We present data for both SF and TF paradigms for Tlx3-Cre[+] and Glt25d2-Cre^{+} neurons but only for the SF paradigm for L5 Efr3a-Cre^{+} neurons. This is because L5 Efr3a-Cre^{+} neurons tend to prefer very high SF and were therefore rarely responsive to the lower SF gratings used in the TF paradigm (see details below).

To compare visual response properties between the L5 cell types in V1, we characterized the visual responses (OSI, DSI, TF, and SF) of more than 110 Tlx3-Cre[+], 13 Glt25d2-Cre[+] and 17 L5 Efr3a-Cre^{+} neurons (Figures 6D-E, Table SA.2). Comparisons of the distributions of preferred SF between the three cell types (Figure A.6D) showed that both L5 Efr3a-Cre[+] and Glt25d2-Cre^{+} cells tended to prefer higher SF than Tlx3-Cre^{+} cells (median 0.04 c/d for Tlx3-Cre[+] and 0.08 c/d for both Glt25d2-Cre[+] and L5 Efr3a-Cre[+]) but only the distribution for L5 Efr3a-Cre^{+} cells differed significantly from Tlx3-Cre^{+} cells (Kruskal-Wallis test, $p = 0.0015$, with Dunn's

multiple comparisons L5 Efr3a-Cre[+] versus Tlx3-Cre[+], p=0.0019). The distributions for Tlx3-Cre[+] and Glt25d2-Cre^{+} cells appear similar to previous reports for mouse V1 L2/3 neurons (Marshel et al., 2011; Niell and Stryker, 2008). However, L5 Efr3a-Cre^{+} neurons appear unique in that the great majority of cells (14/17, 82%) prefer SF of 0.08 or higher. While Glt25d2-Cre[+] and Tlx3-Cre^{+} neurons did not differ significantly in their SF tuning, these populations did differ significantly in TF tuning (Figure A.6E), with Glt25d2-Cre^{+} neurons preferring TFs that were nearly twice as fast as for Tlx3-Cre^{+} neurons (median 4.0 Hz and 2.0 Hz respectively, Wilcoxon rank-sum test, p = 0.0242). All three cell types were highly orientation tuned. Across SF and TF experiments, Glt25d2-Cre[+] were the least tuned, yet still had median OSI values >0.61, and over two-thirds of cells had an OSI > 0.5. (See Figure A.6D-E for values for all cell types.)

Using the varied SF paradigm with TF held constant at 1 Hz, L5 CS PNs were remarkably direction selective and non-parametric statistical tests showed that Glt25d2-Cre^{+} neurons have higher DSI (median 0.57) than Tlx3-Cre[+] (median 0.24, Kruskal-Wallis test p=0.0024, with Dunn's multiple comparisons, Tlx3-Cre[+] versus Glt25d2-Cre[+], p = 0.0135). 60% of Glt25d2-Cre^{+} cells were very sharply tuned for direction (DSI > 0.5) while less than 30% of Tlx3-Cre[+] or L5 Efr3a-Cre^{+} cells had DSI > 0.5 (Figure A.6D, top, right panel). Interestingly, when TF was varied and SF was held constant at 0.04 c/d, the DSI values for Glt25d2-Cre^{+} neurons were lower than in the SF paradigm (median 0.46) while the DSI values were similar for Tlx3-Cre^{+} neurons regardless of the stimulation paradigm (median 0.34) and differences between the distributions were not statistically significant. In summary, L5 Efr3a-Cre^{+} neurons

prefer higher SFs than Tlx3-Cre[+], Glt25d2-Cre^{+} neurons prefer higher TFs than Tlx3-Cre[+], and Glt25d2-Cre[+] are more direction selective than Tlx3-Cre^{+} cells.

DISCUSSION

While previous *in vitro* studies have provided extensive information about the intrinsic physiology and local connectivity of specific cortical cell types, information about brain-wide connectivity and *in vivo* function has been more elusive. Here we took advantage of innovative molecular, viral and genetic tools to study subtypes of layer 5 (L5) pyramidal neurons in the mouse primary visual cortex. First, we identified a Cre-driver mouse line (Efr3a-Cre) that distinguishes a distinct subtype of L5 cortico-cortical, non-striatal (CC-NS)/local pyramidal neurons and used *in vitro* physiological and anatomical approaches to characterize the intrinsic physiology and morphology of these cells, in comparison to L5 CC (Tlx3-Cre) and cortical-subcortical (CS; Glt25d2-Cre) pyramidal neurons. We then employed targeted monosynaptic rabies tracing of brain-wide inputs and GCaMP-based two-photon calcium imaging to characterize the *in vivo* visual function and connectivity of genetically-defined L5 CC, CC-NS and CS pyramidal neurons. Our observations reveal novel insights into the diversity of L5 pyramidal neurons, demonstrating differences in connectivity and physiology that may underlie the unique contributions of each cell type to cortico-cortical versus subcortical computations (Figure A.7).
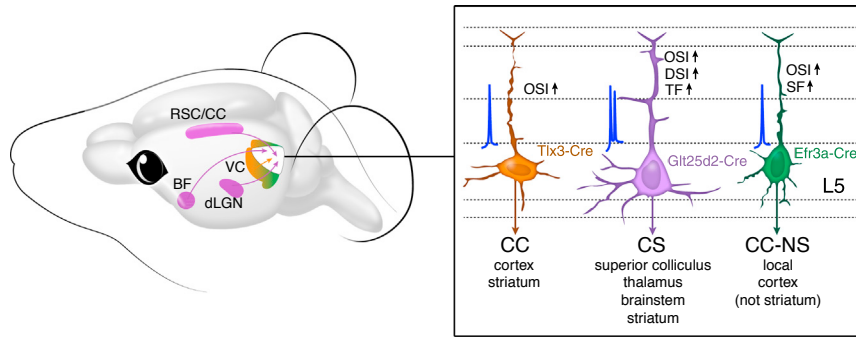
Figure A.7. Connectivity and Function of Three Types of L5 Pyramidal Neurons. Three genetically-identified populations of layer 5 pyramidal neurons in V1 of Tlx3-Cre[+], Glt25d2-Cre[+], and Efr3a-Cre[+] mice were characterized based on monosynaptic rabies tracing of brain-wide inputs (left) and their morphologies, axonal projections, intrinsic electrophysiology and *in vivo* responses to drifting gratings (right). (Left) Tlx3-Cre[+] and Efr3a-Cre^{+} V1 neurons receive preferential long-range inputs from the extrastriate visual areas (orange/green), whereas Glt25d2-Cre^{+} V1 neurons receive preferential inputs from the retrosplenial cortex, the basal forebrain, and dLGN (purple). (Right) CC Tlx3-Cre[+], CS Glt25d2-Cre[+], CC-NS Efr3a-Cre[+] V1 L5 pyramidal neurons exhibit distinct axonal projections, cell morphology, electrical properties and visual responses. Abbreviations: BF, basal forebrain; CC, cortico-cortical; CC-NS, cortico-cortical non-striatal; CS, cortico-subcortical; dLGN, dorsal lateral geniculate nucleus; RSC/CC, retrosplenial and cingulate cortex; VC, visual cortex.

Heterogeneity of L5 PNs and their functions

Historically, cortical layer 5 pyramidal neurons have been classified into two types, originally defined by their distinct projections to subcortical versus cortical

targets (CS and CC, respectively) (O'Leary and Koester, 1993). Since that time there have been innumerable studies of the intrinsic physiology, connectivity and function of these neuronal populations, as well as evolving nomenclature and definitions. Typically the definition used depends on the measurement methods being employed; because these diagnostic features have been well documented and are highly correlated, measurement of a single property generally allows other features to be unambiguously inferred. For example, CS neurons are invariably intrinsically bursting while CC neurons are regular spiking (Groh et al., 2010; Kasper et al., 1994), and CS neurons have a larger cell body, thicker apical dendrite and more extensive apical dendritic tuft than CC cells, leading to names such as thick- or thin-tufted, and tall- or slender-tufted (Groh et al., 2010; Kasper et al., 1994; Larkman et al., 1988). In the S1 barrel cortex, CC and CS neurons are largely confined to layers 5A and 5B, respectively (Groh et al., 2010), leading to a 5A versus 5B nomenclature. In motor cortex, CS neurons project to the pyramidal tract and have been termed PT while the CC cells are called intratelencephalic (IT) (Gerfen et al., 2013). These distinctions, however, cannot be universally applied across cortical areas or species as seen here in mouse V1 (Zarrinpar and Callaway, 2014).

Our observations comparing Efr3a-Cre^{+} neurons to Tlx3-Cre[+] and Glt25d2-Cre^{+} cells reveal that L5 CC neurons in mouse V1 can be further subdivided into at least two distinct groups. Using conventional features to distinguish CC from CS cells, Efr3a-Cre^{+} neurons share the typical diagnostic features of CC cells, including regular spiking physiology, a relatively small cell body, and a thin-tufted morphology. However, with more ovoid cell bodies, higher input resistance, greater percent sag, a

lack of projections to the striatum, and a preference for higher spatial frequency visual stimuli, Efr3a-Cre[+] CC-NS cells differ in several ways from Tlx3-Cre^{+} CC cells. Across our measurements, percent sag, sag amplitude, and absence of a striatal projection most clearly distinguish Efr3a-Cre[+] from Tlx3-Cre^{+} cells and can therefore be considered as diagnostic of the cell type: the percent sag and sag amplitude measures are both more than 3-fold greater on average for the Efr3a-Cre^{+} cells and there is very little overlap in the percent sag distributions and no overlap in the sag amplitudes. Another diagnostic feature of Efr3a-Cre^{+} cells in V1 is a lack of projections to the striatum; while axons projecting to the ipsilateral striatum are clearly seen from both Tlx3-Cre[+] and Glt25d2-Cre^{+} neurons, they are not present in Efr3a-Cre[+] mice. Previous studies have shown a strong correlation between percent sag and hyperpolarization-activated cyclic nucleotide gated cation channel (HCN1) and Trip8b expression in L5 projection neurons (Day et al., 2005; Sheets et al., 2011). In future studies, it would be interesting to investigate whether L5 Efr3a-Cre^{+} cells may also differ from Tlx3-Cre^{+} neurons in the expression levels of HCN1.

Previous single cell tracing and genomic profiling studies have shown that both CC and CS L5 neurons can be divided into subgroups projecting only to subsets of their multiple targets or having distinct somato-dendritic morphology, or expressing specific combinations of genes (Bourassa and Deschenes, 1995; Molyneaux et al., 2007; Sorensen et al., 2013). A population of CC neurons in the primary somatosensory cortex can consist of cells projecting to the contralateral cortex, to the contralateral cortex and striatum, or to both the contralateral and ipsilateral frontal cortex (Molyneaux et al., 2007; Sorensen et al., 2013). Individual CS neurons in the

primary visual cortex can also project to different subsets of known targets of the population, including superior colliculus, ventral LGN, LD/LP, pretectum and pons (Bourassa and Deschenes, 1995). Despite the diversity of projections, these differences have not been correlated with other anatomical or physiological features as we have demonstrated for Tlx3-Cre[+] versus Efr3a-Cre[+] L5 PNs. It is also possible that L5 Efr3a-Cre^{+} neurons could comprise more than one type. For example, we have observed that some project to the white matter (and presumably to adjacent cortical areas) while others are strictly local (Figures 1C and S2B). Whether these are truly different types depends on the definition of cell type and whether future studies might correlate these anatomical features with other properties. Such identification of further subdivisions based on distinct genetic, physiological, and anatomical properties will be important to further understanding how separate groups of neurons can function as distinct channels of cortical output to other structures.

It is also important to note that, unlike Efr3a-Cre^{+} L5 neurons in V1, Efr3a-Cre^{+} neurons in other cortical areas, including extrastriate visual areas but not S1 and Au1, appear to include typical CS neurons; they have large pyramidal cell bodies and thick apical dendrites and project axons to subcortical structures (Figure SA.2B). There are several possible explanations for this observation: the cell group distinguished by Cre expression in V1 of Efr3a-Cre mice might be unique to primary sensory cortical areas; Efr3a-Cre expression is present in CS neurons in other cortical areas but not in primary sensory cortex; the expression of Cre does not fully recapitulate the expression pattern of Efr3a and differs between cortical areas. While the possibility that primary sensory cortices possess a cell type not present in other

cortical areas is at odds with the notion of a universal cortical laminar and cellular architecture, this would certainly not be the first such observation. In the future it will be important to search for cells like the V1 Efr3a-Cre^{+} cells in other cortical areas and, if they are present, to identify methods to distinguish them. For example, gene expression profiling comparing Efr3a-Cre^{+} neurons to Tlx3-Cre^{+} neurons in mouse V1 might reveal differences in gene expression that more universally distinguishes the cell type across all cortical regions.

In vivo physiology and monosynaptic long distance inputs to layer 5 neurons

Our data show that L5 neurons exhibit diverse *in vivo* visual receptive fields. Glt25d2-Cre^{+} V1 neurons display higher DSI and prefer higher temporal frequencies compared to Tlx3-Cre^{+} V1 neurons. This indicates that Glt25d2-Cre^{+} neurons and Tlx3-Cre^{+} neurons integrate and convey different visual information to downstream target regions. Furthermore, Efr3a-Cre^{+} neurons prefer higher SFs than both Tlx3-Cre^{+} neurons, suggesting that these cells are involved in pathways requiring higher visual acuity. Lastly, we found that each of these cell types were highly orientation tuned, more so than those reported in previous studies using single-unit electrical recordings in L5 of anesthetized or awake mice (Niell and Stryker, 2008; Niell and Stryker, 2010).

As L5 neurons are long distance output neurons, it is particularly interesting to correlate their stimulus selectivity to the projection targets. L5 CC PNs may convey visual information necessary for object recognition to higher visual areas in a feedforward manner. In contrast, L5 CS PNs may convey visual motion-related information to the superior colliculus. Previous studies of functional properties and

connections in primate, cat, and rodent V1 also suggest that CC PNs process and convey image-forming visual information to higher visual cortices, whereas CS PNs are involved in sensory gating associated with movement (Finlay et al., 1976; Palmer and Rosenquist, 1974; Van Essen, 2005).

We find that different types of L5 projection neurons receive different proportions of input from the many cell populations that project to mouse V1. This contrasts with previous studies, which found no difference in the laminar sources of local inputs to L5 CC and CS PNs (Schubert et al., 2001; Zarrinpar and Callaway, 2014). Nevertheless, the differences in visual receptive fields described here suggest that these two populations integrate inputs from populations of neurons that impart different functional properties. Such differences might include local inputs in addition to the differences that we have observed in long-distance inputs.

It is noteworthy that L5 CC Tlx3-Cre[+] PNs that provide direct feedforward input to higher visual areas receive a higher proportion of feedback inputs from those same areas when compared to L5 CS Glt25d2-Cre[+] PNs. This is consistent with the potential importance of feedback in regulating levels of feedforward input. Feedback might also play a more important role in high-resolution image formation than in the generation of signals that are conveyed subcortically. In contrast, Glt25d2-Cre^{+} neurons receive a higher proportion of their inputs from retrosplenial and cingulate cortical areas, and cingulate cortex has recently been implicated in direct top-down attentional modulation of mouse V1 (Zhang et al., 2014). Together these observations suggest an important role for top-down modulation of V1 neurons projecting to the superior colliculus and other subcortical regions. Such an influence on neurons that

project to superior colliculus is consistent with its role in regulation of spatial attention (Krauzlis et al., 2013).

Using recently available Cre driver lines, we have defined and characterized subtypes of L5 PNs in mouse V1 based on their morphology, axonal projections, and intrinsic electrophysiology, and we have correlated these features with differences in visual responses and brain-wide monosynaptic input networks. Altogether these observations provide insight into potential mechanisms by which differential inputs and integrative mechanisms create functionally distinct outputs that are specialized for the roles of each cell type. This work can serve as a foundation for future studies that are likely to further subdivide L5 PN types and probe their contributions to perception and behavior by manipulating their activity and that of their various inputs.

EXPERIMENTAL PROCEDURES

Transgenic mice

All experimental procedures followed procedures approved by the Salk Institute Animal Care and Use Committee. Tlx3-Cre PL56, Glt25d2-Cre (or Colgalt2-Cre) NF107 and Efr3a-Cre NO108 mice are GENSAT BAC transgenic lines and have been previously described (Gerfen et al., 2013; Gong et al., 2007). Mouse strains were maintained on mixed genetic backgrounds (129/C57BL6).

Virus preparation

For Cre-dependent fluorescent labeling, we used AAV1.CAG.Flex.eGFP.WPRE.bGH (AAV-FLEX-eGFP), AAV8.CAG.Flex.tdTomato.WPRE.SV40 (AAV-FLEX-tdTomato) and Cav2-Cre. AAV1.CAG.Flex.eGFP.WPRE.bGH was purchased from Penn Vector Core.

AAV8.CAG.Flex.tdTomato.WPRE.SV40 ($8.6X10^{12}$ GC/ml) was produced by the Salk Viral Vector Core after obtaining pAAV-FLEX-tdTomato, a gift from Edward Boyden (Addgene plasmid #28306). Cav2-Cre virus with physical particle (pp)/ml of $6.2X10^{12}$ was purchased from EJ Kremer at the Institute of Molecular Genetics of Montpellier. For two-photon imaging, we used a 2:1 mixture of AAV1.CAG.Flex.GCaMP6f.WPRE.SV40 ($3.06X10^{13}$ GC/ml) or AAV1.hSyn.Flex.GCaMP6s.WPRE.SV40 ($3.63X10^{13}$ GC/ml) from Penn Vector Core and AAV-FLEX-tdTomato.

For rabies virus tracing, two Cre-dependent helper viruses, AAV8.EF1α.FLEX.eGFP-T2A-TVA.WPRE.hGH ($3.5X10^{13}$ GC/ml) (Wall et al., 2010) (referred to in the text as AAV-FLEX-GFP-TVA) and AAV8.EF1α.FLEX.G.WPRE.hGH ($7.6X10^{13}$ GC/ml) expressing chimeric rabies glycoprotein (PBG) (referred to in the text as AAV-FLEX-G), were produced by the Salk Viral Vector Core. PBG is a chimeric glycoprotein consisting cytoplasmic domain of SAD B19 strain glycoprotein and extracellular domain of Pasteur virus strain glycoprotein. This plasmid will be deposited in Addgene. A 3:7 mixture of AAV-FLEX-GFP-TVA and AAV-FLEX-G was used for viral injections. EnvA-pseudotyped G-deleted rabies virus, EnvA+RV*dG*-dsRed with the titer of $3.6X10^{7}$ infectious units (IU/ml), was produced following the published protocol (Osakada and Callaway, 2013).

Animal surgery for virus injection

Transgenic or C57BL/6 mice received viral injections when they were at P42-60 for virus tracing, P22-28 for slice preparation and electrophysiology, and at P60-90

for imaging experiments. Mice were anaesthetized with 100 mg/kg of ketamine and 10 mg/kg xylazine cocktail via intra-peritoneal injections and mounted in a stereotax (David Kopf Instruments Model 940 series, Tujunga, CA) for surgery and stereotaxic injections. Virus was injected into the center of V1, using the following coordinates: 3.4 mm rostral, 2.6 mm lateral relative to bregma and 0.5-0.7 mm ventral from the pia. We injected 100nl of AAVs using either air pressure by picospritzer (General Valve Corp, Fairfield, NJ) or performed iontophoresis (Precision Current Source, Stoelting Co., Wood Dale, IL) at +3-5 μA set to alternate on for 7 second and off for 7 second for 5 minutes. For Cav2-Cre injection into the superior colliculus, 100 nl of virus were injected with stereotaxic coordinates: 3.5 mm rostral, 0.5 mm lateral to bregma and 1.35 mm ventral from the pia. For cholera toxin subunit B injection to LP, we injected at -1.82 mm along anterior-posterior axis, 1.25 mm medial-lateral axis from bregma, and 2.70 mm ventral from the pia. To prevent virus backflow, the pipette was left in the brain for 5-10 minutes after completion of injection. After recovery, mice were housed with ibuprofen medicated water for 3 weeks before tissue harvest to allow transgene expression. For rabies virus experiments, 3 weeks after AAV helper injection, 200 nl of five-fold diluted EnvA+RVdG-dsRed ($7.2X10^6$ IU/ml) were injected into the same site in V1 using picospritzer-mediated air pressure. Mice were housed for 7-8 days to allow for trans-synaptic rabies spread and dsRed expression.

Histology and image analysis

Brains were harvested after transcardial perfusion using phosphate-buffered saline (PBS) followed by 4% paraformaldehyde (PFA). Brains were dissected out from skulls and post-fixed with 2% PFA and 15% sucrose in PBS at 4°C for 16-20

hours, then immersed in 30% sucrose in PBS at 4°C before sectioning. 50 μm coronal brain sections were prepared using a freezing microtome and stored in PBS with 0.01% sodium azide at 4°C. To enhance eGFP and dsRed signals, free-floating sections were incubated at 4°C for 16-48 hours with goat anti-GFP (1:1000; Rockland 600-101-215) and rabbit anti-dsRed (1:500; Clontech 632496) primary antibodies in PBX/0.5% normal donkey serum/0.1% Triton-X 100, followed by the appropriate secondary antibodies conjugated with Alexa 488 or 594 (Molecular Probes). Sections were counterstained with 10 μM DAPI in PBS for 30 min to visualize cell nuclei. Immunostained tissue sections were mounted on slides with Polyvinyl alcohol mounting medium containing DABCO and allowed to air-dry overnight. Confocal imaging was performed with Zeiss LSM710 or LSM780 confocal microscope. For anatomical experiments, multiple sections from at least three mice were analyzed. Confocal images were processed and analyzed in NIH ImageJ software (FIJI). For neuronal reconstructions, dendritic arbors, soma, and axons were drawn using an Olympus fluorescence microscope with a Neurolucida reconstruction system (MicroBrightField, Williston, VT).

For rabies tracing analysis, every other 50 μm coronal section from bregma 2.50 mm to -5.00 mm were collected. Individual tissue sections were scanned with a 10X objective using Olympus VS120 slide scanner. Cell counts and registrations were acquired using OlyVIA 2.6 software provided by Olympus. Cortical regions of each scanned section were registered manually by using the nuclear counterstain (DAPI) channel to visualize layer 4 laminar width. The section was then registered again using The Mouse Brain in Stereotaxic Coordinates atlas (Paxinos et al., 2001) fit to the

scanned image using the first registration as a guide to adjust for minor tissue variation or deformation. Borders were then added to denote layer boundaries; these were based on nuclear counterstain density. Lastly, dsRed and GFP channels were turned on and cell counts were recorded for each brain region.

Slice preparation for electrophysiology

Mice (P28-50) were deeply anesthetized with Euthasol (100 mg/kg, intraperitoneally), and transcardially perfused with ice-cold sucrose artificial cerebral spinal fluid (ACSF) containing (in mM) 87 NaCl, 2.5 KCl, 26 $NaHCO_3$, 1.25 NaH_2PO_4, 1 $MgSO_4$, 10 D-(+)-glucose, 75 Sucrose, 2 $CaCl_2$. Following decapitation, coronal brain slices (300 μm thick) were cut (VF-300 Compresstome™, Precisionary Instruments, Greenville, NC) from the primary visual cortex in the same ice-cold sucrose ACSF bubbled with 95% O_2/5% CO_2. Slices were then incubated at 34°C for at least 30 minutes and remained submerged in a holding chamber at room temperature in sucrose ACSF bubbled with 95% O_2/5% CO_2 until recording.

Basic electrophysiology

Slices were transferred to a recording chamber where they were submerged in oxygenated ACSF containing (in mM) 125 NaCl, 2.5 KCl, 25 $NaHCO_3$, 1.25 KH_2PO_4, 1 $MgSO_4$, 20 D-(+)-glucose, 2 $CaCl_2$ and containing the following synaptic blockers (in μM): 50 DL-2-amino-5-phosphonopentanoic acid (DL-AP5, Tocris Bioscience), 20 6-cyano-7-nitroquinoxaline-2,3-dione disodium (CNQX, Tocris Bioscience). Glass recording electrode (3-5 MΩ resistances) was filled with intracellular solution containing (in mM) 130 K-gluconate, 7 KCl, 0.5 EGTA, 5 Tris-Phosphocreatine, 4 Mg-ATP, 0.3 Na-GTP, 10 HEPES, and 0.3% biocytin (pH 7.3). Whole cell recordings

were made from fluorescently labeled pyramidal cells in layer 5 primary visual cortex selected under visual control using differential interference contrast (DIC) optics/fluorescent Olympus microscope and Retiga 2000R camera (Qimaging). All recordings were performed in current-clamp mode with a MultiClamp 700B amplifier (Molecular Devices) at room temperature. Signals were acquired using open-source software application *Ephus* (http://www.ephus.org), sampled at 10 kHz, filtered at 4 kHz and analyzed off-line with MATLAB (The Mathworks, Natick, MA). Only recordings that showed a stable resting membrane potential below −50 mV and access resistance (<20 MΩ) were included in the intrinsic electrophysiology data analysis. Input resistance was calculated as the slope of the linear fit to the current-voltage (I-V) relationship using current pulses of -100 pA to -500 pA with -100 pA current steps and 0.5 sec duration. Percent sag during hyperpolarizing current pulses was calculated as the difference of the peak response amplitude and the steady state response amplitude divided by the peak response amplitude multiplied by 100 (Angelo and Margrie, 2011; Mason and Larkman, 1990; Stafstrom et al., 1984).

$$\% \text{ sag} = 100 \times (V_{peak} - V_{steady\ state})/V_{peak}$$

We calculated percent sag from the hyperpolarizing current pulses that generated steady state potentials closest to -100 mV. There was no significant difference in the steady state potential used to calculate percent sag for Tlx3-Cre[+], Glt25d2-Cre[+], L5 Efr3a-Cre^{+} neurons (-101.30 ± 0.95 mV, -97.95.3 ± 2.87 mV, -102.1 ± 3.45 mV respectively, Figure SA.3B). Percent sag did not vary significantly with resting membrane potential for the hyperpolarizing current pulses used (-100 pA to -500 pA, 0.5 sec duration, Figure SA.3C). Measure of spike frequency adaptation from

the first interspike interval (ISI) to the steady was computed as the initial over the steady state ISI ratios (Mason and Larkman, 1990). "Stead state" interspike ISI was calculated as the average ISI after the third action potential in a pulse train. Interspike interval ratios were examined for pulse trains with mean steady state frequency (reciprocal of the interspike interval) high enough to observe spike frequency adaptation. For comparison, we chose pulse trains with steady state frequency that were similar in values with a range of 10 spikes/sec to 20 spikes/sec. Pulse trains were evoked with one second duration current pulses ranging from 50 pA to 800 pA amplitude in 50 pA current increments. Burst-spiking cells (BS) were defined as cells that fired burst (doublet or triplet) spikes near threshold currents, while regular spiking (RS) cells fired single spikes.

Two-photon calcium imaging

Experiments were performed on 2-4 month old transgenic mice (male and female) approximately 7-15 days after GCaMP6 virus injection. Animals were anesthetized with inhaled isoflurane (0.5-1.2% in oxygen) and carprofen (5 mg/kg SC) and custom circular head frames were mounted to the skull with dental acrylic (C&B-Metabond®). Eyes were kept moist with ointment during surgeries. A 5-6mm diameter craniotomy was made over V1 and the dura was also removed. Dura removal proved necessary for clear imaging in layer 5 (475-620 μm deep, Figure A.6B). The brain was covered with a cranial window, consisting of a 4 or 5 mm coverslip and a metal ring designed to fit within the headframe. Pressure was gently applied to the brain upon placement of the window. After implantation of the window, the mouse was allowed to wake up, and imaging began when the mouse was fully awake. For

several mice, imaging was performed over multiple days. These mice were housed with ibuprofen medicated water. During imaging, mice were stationary and positioned in a plastic cylinder to restrict movement. Imaging was done with a custom-made scope (Marshel et al., 2011) and ScanImage 3.8 with scan parameters 256x256 lines/frame at 2 msec/line. GCaMP6 was excited at 920 or 940 nm at high power of Ti:Sapphire laser (Coherent), and emission was collected with a green (535 ± 50 nm or 525 ± 50 nm) and a red (610 ± 75 nm or 610 ± 60 nm) filter (Chroma).

Visual stimuli for two-photon imaging

Mice were positioned 13 cm from a video monitor, which was centered on their eye and pointed towards their nose at a 30° angle. Stimuli were 4 sec duration, 100% contrast sine wave grating moving in 8 different directions. For each population of neurons (a single 16x imaging plane, with 1-2.5x digital zoom), we presented two sets of stimuli: a temporal frequency (TF) varying experiment (0.5, 1, 2, 4, and 8 Hz, 8 directions plus blank, 0.04 c/d, 5 repeats pseudorandomized), and a spatial frequency (SF) varying experiment (0.01, 0.02, 0.04, 0.08, and 0.16 c/d, 8 directions plus blank, 1 Hz, 5 repeats pseudorandomized) The stimulus was spherically corrected to account for distortions in size and spatial frequency at the periphery, effectively keeping SF and TF constant throughout the visual field (Marshel et al., 2011). Stimuli were generated by a customized PsychToolbox interface in MATLAB (Marshel et al., 2011).

Analysis of calcium imaging data

Regions of interest (ROIs) around each cell were created using a semi-automatic cell segmentation method (Marshel et al., 2011). To account for movement-

related image shifts as well as drifts in the image over time, we used a procedure involving multiple movement correction algorithms both in ImageJ (using StackReg and Template Matching plugin) and a customized movement correction algorithm in MATLAB (Marshel et al., 2011) that aligned each trial of the experiment to the average image of the first trial by determining the highest cross-correlation between images. The type of motion correction algorithm used depended on the severity of motion. Each experiment was manually checked to ensure motion had been effectively corrected. Any field of view with uncorrectable x-y shifts or evidence of z-motion was discarded. Baseline fluorescence (F_B) was averaged within each cell ROI for each trial during a 2 sec prestimulus period during which a gray screen (mean luminance of gratings) was presented. The stimulus-evoked time course was converted from absolute to relative fluorescence by computing $\Delta F/F = (F_I-F_B)/F_B$, where F_I is the average instantaneous, stimulus-evoked fluorescence signal over the duration of the stimulus (4 sec).

Identification of responsive and reliable cells

The population analysis was restricted to cells that were both responsive ($\Delta F/F$ > 6%) and reliable as determined by a D-prime metric, defined as $\delta=(\mu_{max}-\mu_{blank})/(\sigma_{max}+\sigma_{blank})$ where μ_{max} and σ_{max} are the mean and standard deviation of the response to the preferred stimulus, and μ_{blank} and σ_{blank} are the mean and standard deviation to the blank stimulus. Neurons were deemed reliable for $\delta>1$. The neurons that met these criteria were used as the denominator in all subsequent analyses. Any field of view that did not have at least one cell meeting the criteria was discarded. Due to a slow decay in the fluorescence over the 4 second imaging period, even during the

blank screen (Figure SA.6), we baseline corrected the $\Delta F/F$ by subtracting the mean $\Delta F/F$ during the blank stimulus. This assures that stimulus-evoked values are in relation to a proper baseline corrected for bleaching of the fluorescence, likely due to the higher laser power necessary for deep imaging. These corrected $\Delta F/F$ values were used to construct tuning curves and derive cell metrics, but did not contribute to the identification of responsive and reliable cells. The indices (OSI and DSI) were defined as $SI = (\mu_{max} - \mu_{null}) / (\mu_{max} + \mu_{null})$ where μ_{max} is the mean response to the preferred direction and μ_{null} is the mean response to the opposite direction for DSI, and the average of the two orthogonal directions for OSI. As some cells suppressed their response below the blank baseline response for null orientations (Figure SA.7D), the OS and DS indices were occasionally above 1.0.
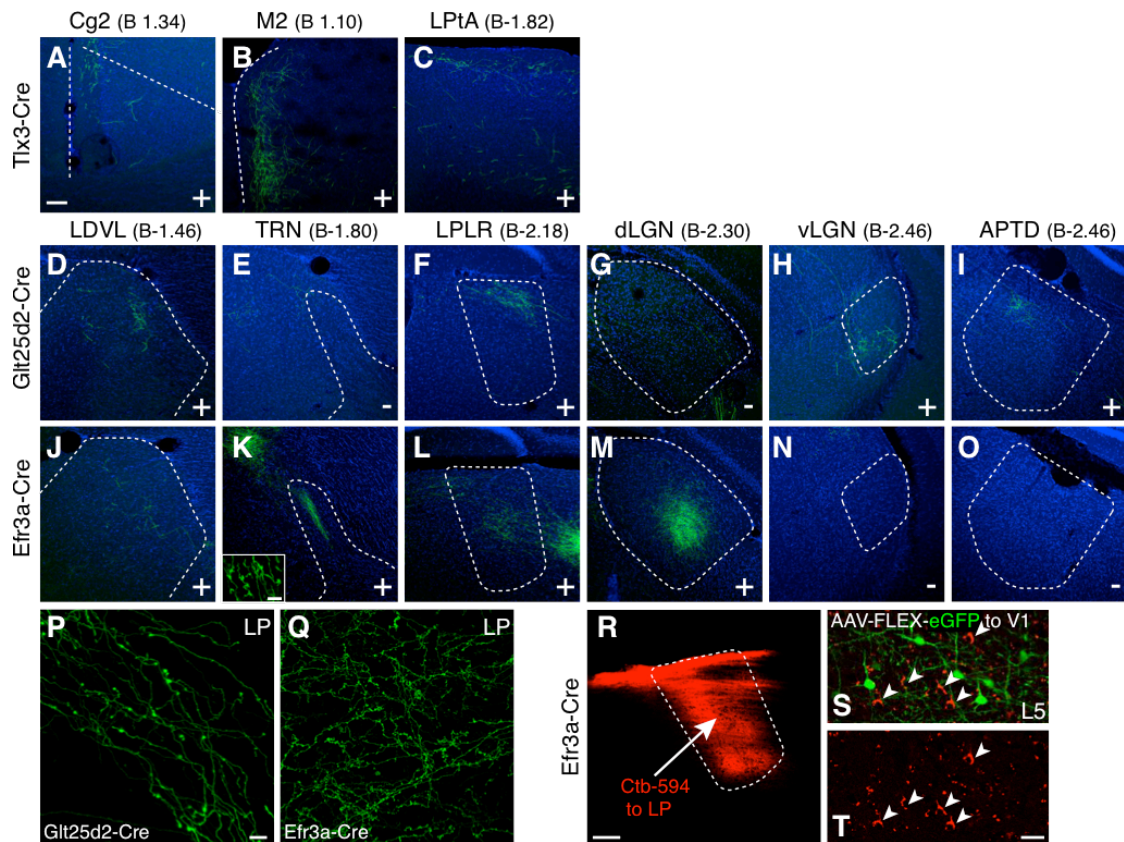
SUPPLEMENTAL FIGURES

Figure SA.1. Axon Targets of Tlx3-Cre+, Glt25d2-Cre+ and Efr3a-Cre+ Neurons, related to Figure A.1. (A-C) eGFP+ axons of Tlx3-Cre+ V1 neurons in distant cortical areas. (D-O) eGFP+ axons of Glt25d2-Cre+ or Efr3a-Cre+ V1 neurons in various subcortical structures. (P-Q) Type I axon terminals from Efr3a-Cre+ V1 neurons (Q) and Type II axon terminals from Glt25d2-Cre+ V1 neurons (P) in LP. (R) Cholera toxin subunit B conjugated to Alexa 594 injection in LP. (S) AAV-FLEX-eGFP injection to V1 of Efr3a-Cre+ mouse brain. (S-T) eGFP+ L5 Efr3a-Cre+ neurons are not retrogradely labeled by Ctb-594. Abbreviations: APTD, anterior pretectal nucleus, dorsal part; Cg2, cingulate cortex, area 2; dLGN, dorsal nucleus of the lateral lemniscus; LDVL, laterodorsal thalamic nucleus, ventrolateral part; LPLR, lateral posterior thalamic nucleus, laterorostral part; LPtA, lateral parietal association cortex; M2, secondary motor cortex; TRN, thalamic reticular nucleus; vLGN, ventral lateral geniculate nucleus. Scale bars = 100 μm (A-O, R), 5 μm (inset in K), 10 μm (P-Q), 20 μm (T).
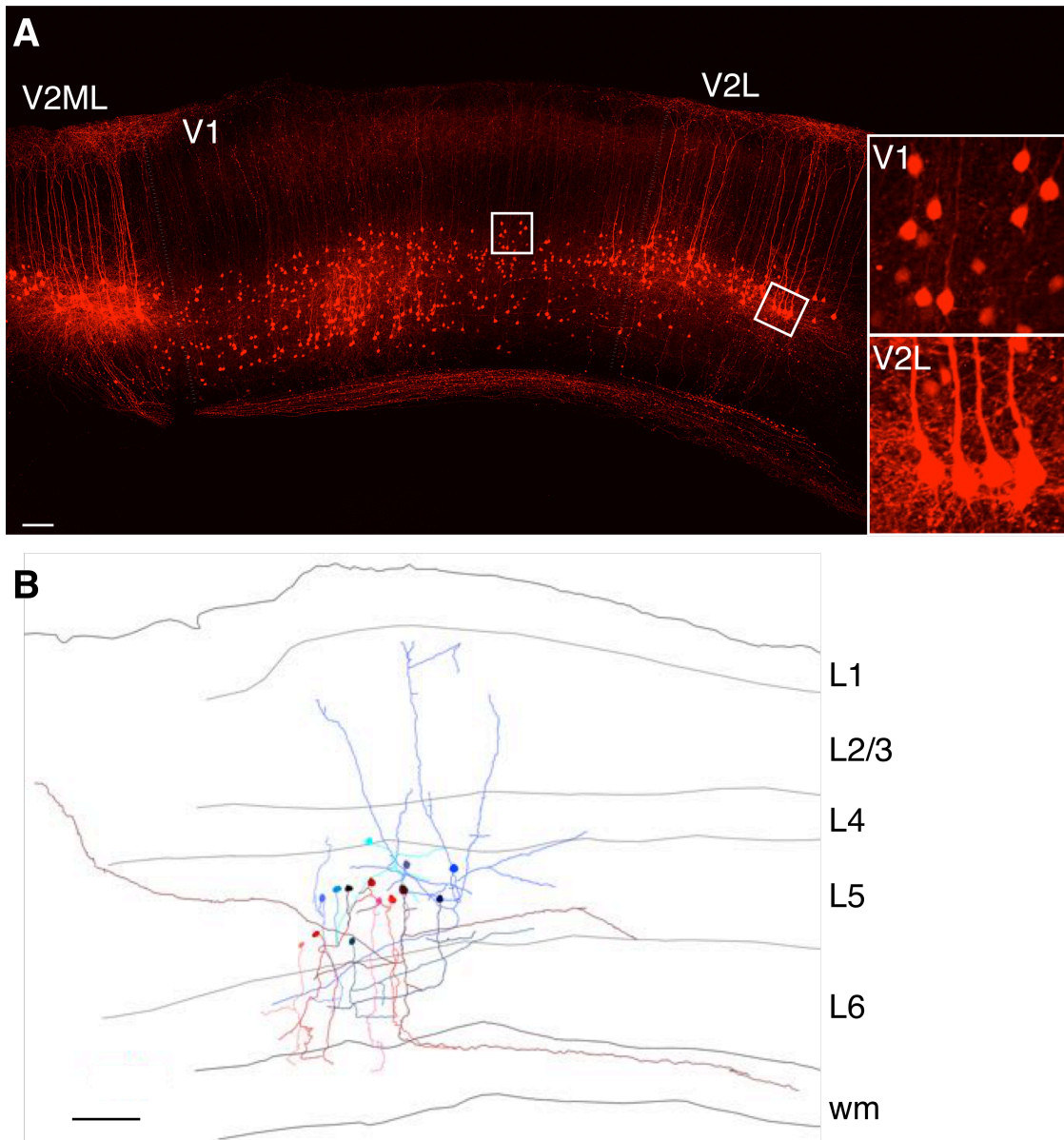
Figure SA.2. Efr3a-Cre+ Cell Morphology and Axonal Projections in Visual Cortex, related to Figure A.1. (A) Difference in morphologies of L5 Efr3a-Cre+ neurons labeled by AAV-FLEX-tdTomato in V1 versus V2L or V2ML. (B) Neurolucida reconstruction of the axons of L5 Efr3a-Cre+ neurons that were sparsely labeled in V1 (see Experimental Procedures). Blue hued neuron reconstructions are local pyramids, whereas red hued neuron reconstructions are CC-NS neurons. Scale bars = 100 μm.

Figure SA.3. Sag Parameters of Three Types of Layer 5 Pyramidal Neurons, related to Figure A.2. (A) Correlation between peak membrane potential (mV, maximum negative value) and steady state membrane potential (mV) evoked by injection of hyperpolarizin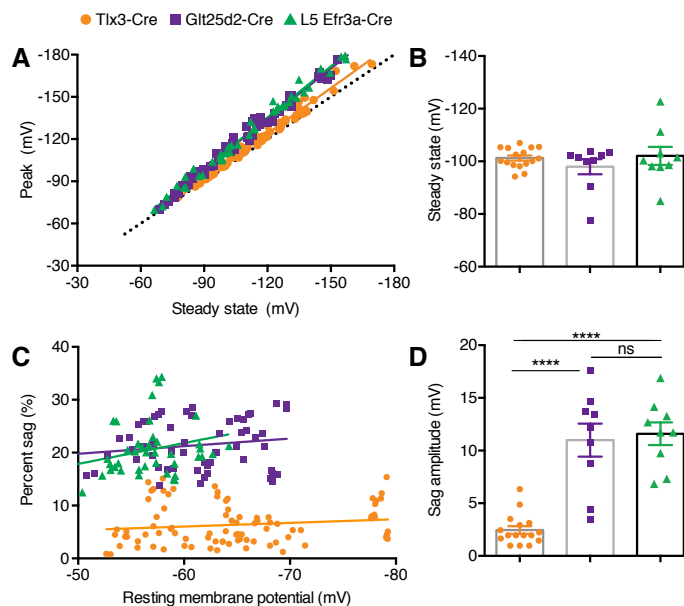g current steps (5 steps for each cell ranging from -100 pA to -500 pA, 500 msec duration). Data for points for all current step amplitudes for all cells are indicated. Slopes fit to data from each cell type depict voltage dependency and variability of sag between cell types. Dotted line indicates the unity line. Slopes of the linear regression line were significantly different for Tlx3-Cre+ vs. Glt25d2-Cre+ ****p<0.0001, Tlx3-Cre+ vs. L5 Efr3a-Cre+ ****p<0.0001, but not Glt25d2-Cre+ vs. L5 Efr3a-Cre+ p=0.5578). Statistics were calculated from analysis of covariance. These data indicate that sag is significantly more prominent for Glt25d2-Cre+ and L5 Efr3a-Cre+ neurons than Tlx3-Cre+ neurons. (B) Percent sag was calculated from the current injection condition that resulted in steady state Vm closest to -100mV. Plots illustrate mean steady state membrane potentials (mV) used to compute percent sag (%) and sag amplitude (mV) for each cell type. Each cell in the population is also indicated by an individual data point. Values are reported as means ± SEM. n = 16 cells for Tlx3-Cre+, 9 for 3 Glt25d2-Cre+ and 9 for L5 Efr3a-Cre+. (C) Percent sag (%) plotted against resting membrane potential (mV) for all current injection trials from all cells. Lines indicate linear fit for each cell type. Note that percent sag is not dependent on resting membrane potential. (D) Sag amplitude (mV) for Tlx3-Cre+, Glt25d2-Cre+ and L5 Efr3a-Cre+ neurons. Values are reported as means ± SEM for each cell type. n = 16 cells for Tlx3-Cre+, 9 for Glt25d2-Cre+ and 9 for L5 Efr3a-Cre+. P values were calculated from one-way ANOVAs followed by Tukey's post-hoc tests to compare means of pairs of each cell type. Significant differences between cell types are indicated by ****p<0.0001. ns=not significant

Figure SA.4. Starter Neuron Analysis and Control Experiments for Rabies Trans-Synaptic Tracing, related to Figure A.3. (A) Coronal sections of Tlx3-Cre+ mouse brain after AAV-FLEX-GFP-TVA and EnvA+RVdG-dsRed injection into V1 (AAV-FLEX-G was not injected). dsRed expression from EnvA+RVdG-dsRed due to leak expression of TVA in non-Cre+ neurons is observed locally, but not in distant regions more than 1mm from the injection site. (B) Numbers of starter neurons (left panel) and long-range input neurons (middle panel) for each mouse analyzed. (right panel) Proportion of L5 or L6 starter neurons for each Efr3a-Cre+ mouse. (bottom panel) Relationships between input neuron and starter neuron numbers for each mouse analyzed. Scale bars = 1 mm (large panel) and 100 μm (small panels).
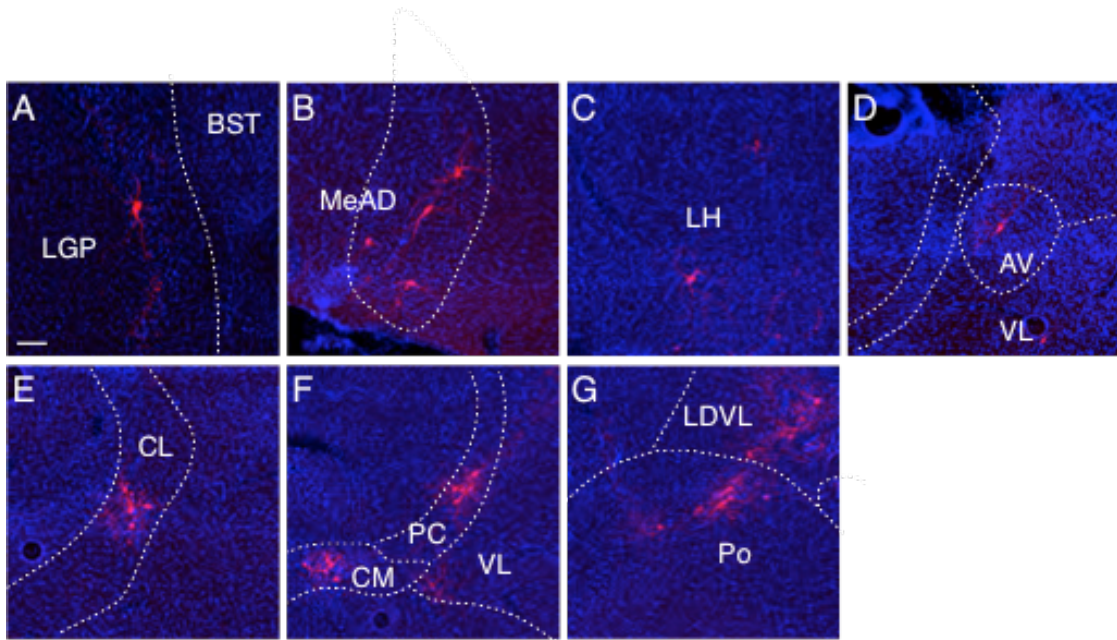
Figure SA.5. Examples of Brain-Wide Monosynaptic Inputs to Layer 5 Pyramidal Neurons Revealed by Monosynaptic Rabies Virus Tracing, related to Figure A.4.(A-G) Coronal sections of rabies virus labeling long-distance inputs in Tlx3-Cre+ mice from LGP (A), MeAD (B), LH (C), AV and VL (D), CL (E), CM and PC (F) and Po (G). Abbreviations: AV, anteroventral thalamic nucleus; CL, centrolateral thalamic nucleus; CM, central medial thalamic nucleus; LGP, lateral globus pallidus; LH, lateral hypothalamic area; MeAD, medial amygdaloid nucleus, anterior dorsal; PC, paracentral thalamic nucleus; Po, posterior thalamic nuclear group; VL, ventrolateral thalamic nucleus. Scale bar = 100 μm.
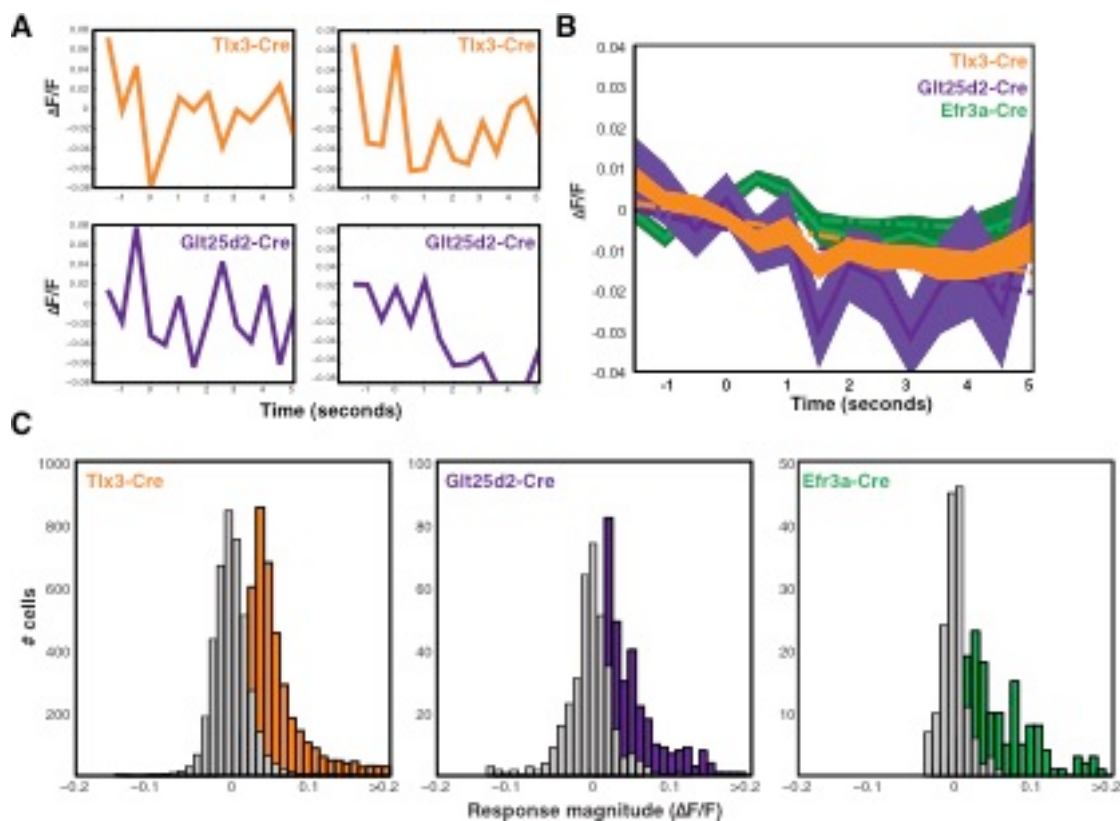
Figure SA.6. Blank and Preferred Responses for Each Cell Type During Two-Photon Calcium Imaging, related to Figure A.6. (A) Sample average time courses for 4 selected cells with particularly severe bleaching during blank stimulus. (B) Average time courses during blank/gray stimuli. Baseline corrected fluorescence values were averaged across all responsive and reliable cells to give an average time course by cell type. Dashed lines are linear fits to the data. Shaded area for each curve is standard error. (C) Response magnitude histograms for all imaged cells by cell type (includes both responsive and non-responsive cells). Gray bars show fluorescence changes during blank trials, colored bars are fluorescence changes to preferred stimulus (or maximum stimulus condition for unresponsive cells). $\Delta F/F$ values plot changes in fluorescence relative to the pre-stimulus baseline, without subtraction of $\Delta F/F$ during blank stimulus. The cutoff for responsive cells was $\Delta F/F > 0.06$.
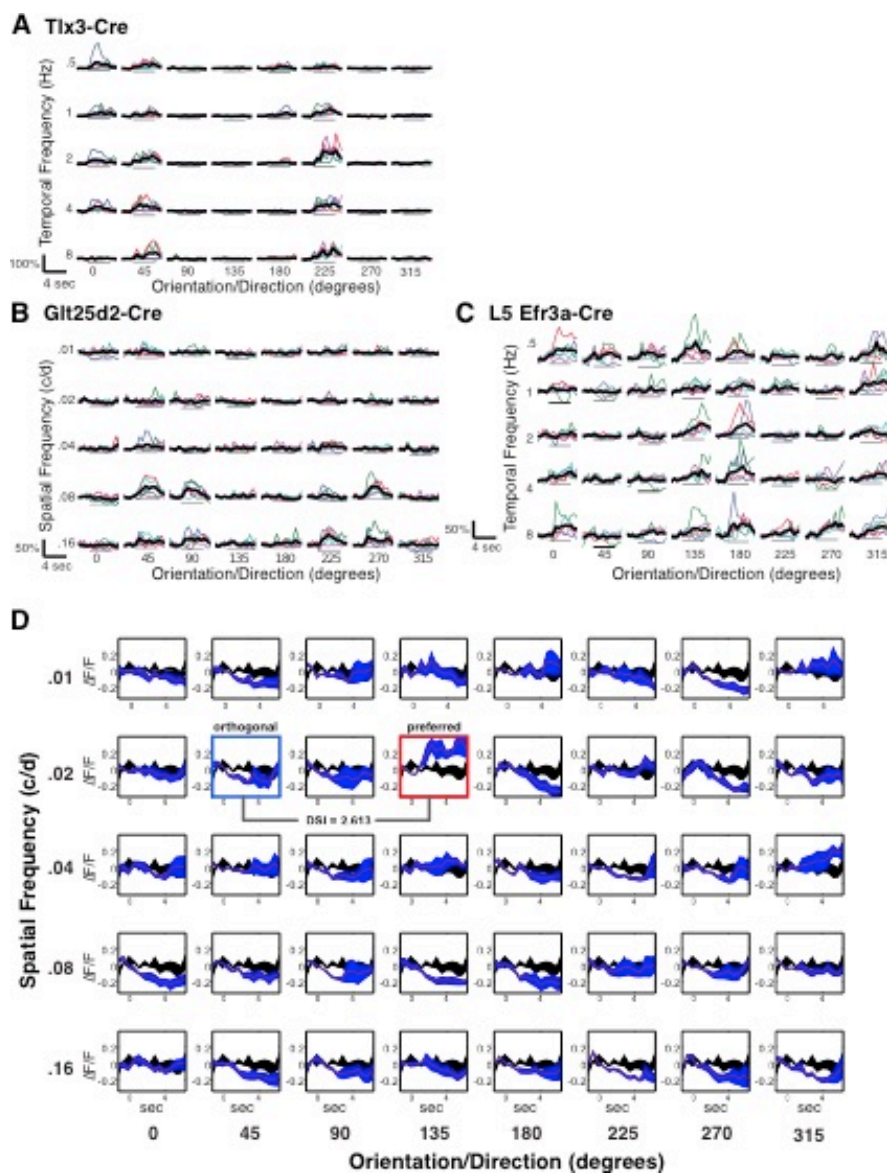
Figure SA.7. Example Visual Responses During Two-Photon Calcium Imaging, related to Figure A.6. (A-C) Fluorescence changes in response to drifting gratings in 8 different directions. Each panel shows all of the responses (5 repeats) for a single neuron to a specific direction and spatial or temporal frequency. Gray lines under each trace indicate duration of stimulus. Thick black traces indicate averaged responses across five repeats. (A) Fluorescence traces for a V1 Tlx3-Cre+ cell at five different temporal frequencies (TFs). (B) Fluorescence traces for Glt25d2-Cre+ cell at 5 different spatial frequencies (SFs). (C) Fluorescence traces for L5 Efr3a-Cre+ cell at 5 different TFs. (D) Example responses of Glt25d2-Cre+ neuron with a DSI > 1.0. Purple traces are average responses across five trials to a given direction and spatial frequency (shading is ± SEM). Black traces are average responses to the blank trials (four repeats, identical in each panel, shading is ± SEM

Table SA.1. Electrophysiological Properties of Three Classes of Layer 5 Neurons, related to Figure A.2. Shown are mean ± SEM. For percent sag, sag amplitude, and RMP,n=16 for Tlx3-Cre, n=9 for Glt25d2-Cre, n=9 for L5 Efr3a-Cre. For capacitance, n=6 for Tlx3-Cre, n=5 for Glt25d2-Cre, n=7 for L5 Efr3a-Cre. For remaining measures, n=17 for Tlx3-Cre, n=11 for Glt25d2-Cre, n=9 for L5 Efr3a-Cre. For multiple comparisons, one-way ANOVA with Tukey post-hoc test was used. $*p < 0.05$; $**p < 0.01$; $****p < 0.0001$. Abbreviations: AP, action potential; ISI, interspike interval; RMP, resting membrane potential.

	Tlx3-Cre	Glt25d2-Cre	L5 Efr3a-Cre	Statistical Comparisons
Input resistance (MΩ)	120.908 ± 6.678	146.365 ± 14.527	263.372 ± 52.722	Efr3a>Glt25d2*, Efr3a>Tlx3*
Percent sag (%)	6.57 ± 0.88	22.19 ± 1.34	20.93 ± 2.05	Efr3a>Tlx3****, Glt25d2>Tlx3****
Sag amplitude (mV)	2.46 ± 0.37	10.99 ± 1.57	11.60 ± 1.07	Efr3a>Tlx3****, Glt25d2>Tlx3****
ISI_1/ISI_mean	0.568 ± 0.024	0.197 ± 0.024	0.443 ± 0.086	Efr3a>Glt25d2**, Tlx3>Glt25d2****
Adaptation index	0.026 ± 0.003	0.036 ± 0.007	0.030 ± 0.009	
Capacitance (pF)	26.30 ± 1.907	159.4 ± 18.49	19.77 ± 3.348	Glt25d2>Tlx3****, Glt25d2>Efr3a****
AP amplitude (mV)	74.52 ± 2.96	73.22 ± 2.32	68.32 ± 3.89	
AP half-width (ms)	2.80 ± 0.47	2.48 ± 0.22	2.35 ± 0.25	
AP rise rate (mV/s)	162.40 ± 14.35	123.54 ± 8.46	119.50 ± 19.24	
AP decay rate (mV/s)	(-)35.25 ± 3.11	(-)29.92 ± 2.28	(-)32.14 ± 6.57	
RMP (mV)	(-)65.67 ± 2.02	(-)60.68 ± 1.55	(-)57.29 ± 1.38	

Table SA.2. Summary of in vivo Two-Photon Imaging Experiments, related to Figure A.6. Total cells are total counted cells in all fields of view. Responsive cells are cells with response magnitudes greater than 6% ΔF/F. Reliable cells are cells with D-prime metric. > 1 (see Experimental Procedures). Responsive & reliable meet both of these criteria.

	Mice	Fields of View	Total Cells	Responsive Cells	Reliable Cells	Responsive & Reliable Cells
SF Experiments						
Tlx3-Cre	5	10	1805	582(32.2%)	211(11.7%)	121(6.7%)
Glt25d2-Cre	8	12	196	61(31.1%)	25(12.8%)	15(7.65%)
Efr3a-Cre	3	4	79	36(45.6%)	23(29.1%)	17(21.5%)
TF Experiments						
Tlx3-Cre	3	10	2328	788(33.8%)	251(10.8%)	110(4.73%)
Glt25d2-Cre	6	8	163	44(27.0%)	24(14.7%)	13(7.98%)

ACKNOWLEDGEMENTS

Appendix A in full is an article published in *Neuron* (December 2015), Kim Euiseok J., Ashley L. Juavinett, Espoir M. Kyubwa, Matthew W. Jacobs, and Edward M. Callaway. 2015. "Three Types of Cortical Layer 5 Neurons That Differ in Brain-Wide Connectivity and Function." *Neuron* 88 (6): 1253–67. The dissertation author was the third author of this work. The dissertation author performed all *in vitro* electrophysiology experiments and analysis and wrote portion of the manuscript concerning *in vitro* electrophysiology. The full article and supplemental materials are

included in Appendix A for completeness. *In vitro* electrophysiology data are shown in Figure A.2(C, D), Figure SA.3 and Table SA.1 (Kim et al. 2015; Appendix A).

REFERENCES

Adesnik, Hillel, and Massimo Scanziani. 2010. "Lateral Competition for Cortical Space by Layer-Specific Horizontal Circuits." *Nature* 464 (7292): 1155–60. doi:10.1038/nature08935.

Alitto, Henry J., and Yang Dan. 2013. "Cell-Type-Specific Modulation of Neocortical Activity by Basal Forebrain Input." *Frontiers in Systems Neuroscience* 6 (January): 79. doi:10.3389/fnsys.2012.00079.

Allen, William E., and Liqun Luo. 2015. "Intersectional Illumination of Neural Circuit Function." *Neuron*. doi:10.1016/j.neuron.2015.02.032.

Ardid, Salva, Martin Vinck, Daniel Kaping, Susanna Marquez, Stefan Everling, and Thilo Womelsdorf. 2015. "Mapping of Functionally Characterized Cell Classes onto Canonical Circuit Operations in Primate Prefrontal Cortex." *Journal of Neuroscience* 35 (7): 2975–91. doi:10.1523/JNEUROSCI.2700-14.2015.

Atallah, Bassam V., William Bruns, Matteo Carandini, and Massimo Scanziani. 2012. "Parvalbumin-Expressing Interneurons Linearly Transform Cortical Responses to Visual Stimuli." *Neuron* 73 (1): 159–70. doi:10.1016/j.neuron.2011.12.013.

Barinka, Filip, Zsófia Maglóczky, and Nada Zecevic. 2015. "Editorial: At the Top of the Interneuronal Pyramid-Calretinin Expressing Cortical Interneurons." *Frontiers in Neuroanatomy* 9 (August): 108. doi:10.3389/fnana.2015.00108.

Bodor, A L, I Katona, G Nyiri, K Mackie, C Ledent, N Hajos, and T F Freund. 2005. "Endocannabinoid Signaling in Rat Somatosensory Cortex: Laminar Differences and Involvement of Specific Interneuron Types." *Journal of Neuroscience* 25 (29): 6845–56. doi:10.1523/JNEUROSCI.0442-05.2005.

Boyden, Edward S, Feng Zhang, Ernst Bamberg, Georg Nagel, and Karl Deisseroth. 2005. "Millisecond-Timescale, Genetically Targeted Optical Control of Neural Activity." *Nature Neuroscience* 8 (9): 1263–68. doi:10.1038/nn1525.

Butt, Simon J B, Marc Fuccillo, Susana Nery, Steven Noctor, Arnold Kriegstein, Joshua G. Corbin, and Gord Fishell. 2005. "The Temporal and Spatial Origins of Cortical Interneurons Predict Their Physiological Subtype." *Neuron* 48 (4): 591–604. doi:10.1016/j.neuron.2005.09.034.

Caputi, Antonio, Andrei Rozov, Maria Blatow, and Hannah Monyer. 2009. "Two Calretinin-Positive GABAergic Cell Types in Layer 2/3 of the Mouse Neocortex Provide Different Forms of Inhibition." *Cerebral Cortex* 19 (6): 1345–59. doi:10.1093/cercor/bhn175.

Chattopadhyaya, Bidisha, Graziella Di Cristo, Hiroyuki Higashiyama, Graham W Knott, Sandra J Kuhlman, Egbert Welker, and Z Josh Huang. 2004. "Experience and Activity-Dependent Maturation of Perisomatic GABAergic Innervation in Primary Visual Cortex during a Postnatal Critical Period." *The Journal of Neuroscience : The Official Journal of the Society for Neuroscience* 24 (43): 9598–9611. doi:10.1523/JNEUROSCI.1851-04.2004.

Curley, Allison A, and David A Lewis. 2012. "Cortical Basket Cell Dysfunction in Schizophrenia." *J Physiol The Journal of Physiology S* 5904: 715–24. doi:10.1113/jphysiol.2011.224659.

Javier DeFelipe, Pedro L López-Cruz, Ruth Benavides-Piccione, Concha Bielza, Pedro Larrañaga, Stewart Anderson, Andreas Burkhalter, Bruno Cauli, Alfonso Fairén, Dirk Feldmeyer, Gord Fishell, David Fitzpatrick, Tamás F Freund, Guillermo González-Burgos, Shaul Hestrin, Sean Hill, Patrick R Hof, Josh Huang, Edward G Jones, Yasuo Kawaguchi, Zoltán Kisvárday, Yoshiyuki Kubota, David A Lewis, Oscar Marín, Henry Markram, Chris J McBain, Hanno S Meyer, Hannah Monyer, Sacha B Nelson, Kathleen Rockland, Jean Rossier, John LR Rubenstein, Bernardo Rudy, Massimo Scanziani, Gordon M Shepherd, Chet C Sherwood, Jochen F Staiger, Gábor Tamás, Alex Thomson, Yun Wang, Rafael Yuste, Giorgio A Ascoli. 2013. "New Insights into the Classification and Nomenclature of Cortical GABAergic Interneurons." *Nature Reviews. Neuroscience* 14 (3): 202–16. doi:10.1038/nrn3444.

Dumenieu, M., N. Fourcaud-Trocme, S. Garcia, and N. Kuczewski. 2015. "Afterhyperpolarization (AHP) Regulates the Frequency and Timing of Action Potentials in the Mitral Cells of the Olfactory Bulb: Role of Olfactory Experience." *Physiological Reports* 3 (5): e12344–e12344. doi:10.14814/phy2.12344.

Džaja, Domagoj, Ana Hladnik, Ivana Bičanić, Marija Baković, and Zdravko Petanjek. 2014. "Neocortical Calretinin Neurons in Primates: Increase in Proportion and Microcircuitry Structure." *Frontiers in Neuroanatomy* 8: 103. doi:10.3389/fnana.2014.00103.

Fenno, L. E., Mattis, J., Ramakrishnan, C., Hyun, M., Lee, S. Y., He, M., Tucciarone, J., Selimbeyoglu, A., Berndt, A., Grosenick, L., Zalocusky, K. A., Bernstein, H., Swanson, H., Perry, C., Diester, I., Boyce, F. M., Bass, C. E., Neve, R., Huang, Z. J., Deisseroth, K. 2014. "Targeting Cells with Single Vectors Using Multiple-Feature Boolean Logic." *Nature Methods* 11 (7): 763–72. doi:10.1038/nmeth.2996.

Fu, Yu, Jason M. Tucciarone, J. Sebastian Espinosa, Nengyin Sheng, Daniel P. Darcy, Roger A. Nicoll, Z. Josh Huang, and Michael P. Stryker. 2014. "A Cortical Circuit for Gain Control by Behavioral State." *Cell* 156 (6): 1139–52.

doi:10.1016/j.cell.2014.01.050.

Fu, Yu, Megumi Kaneko, Yunshuo Tang, Arturo Alvarez-Buylla, and Michael P. Stryker. 2015. "A Cortical Disinhibitory Circuit for Enhancing Adult Plasticity." *eLife* 2015 (4). doi:10.7554/eLife.05558.

Gabbott, P.L.A, and S.J Bacon. 1997. "Vasoactive Intestinal Polypeptide Containing Neurones in Monkey Medial Prefrontal Cortex (mPFC): Colocalisation with Calretinin." *Brain Research* 744 (1): 179–84. doi:10.1016/S0006-8993(96)01232-2.

Galarreta, Mario, F. Erdelyi, G. Szabo, and Shaul Hestrin. 2008. "Cannabinoid Sensitivity and Synaptic Properties of 2 GABAergic Networks in the Neocortex." *Cerebral Cortex* 18 (10): 2296–2305. doi:10.1093/cercor/bhm253.

Galarreta, Mario, Ferenc Erdélyi, Gábor Szabó, and Shaul Hestrin. 2004. "Electrical Coupling among Irregular-Spiking GABAergic Interneurons Expressing Cannabinoid Receptors." *The Journal of Neuroscience* 24 (44): 9770–78. doi:10.1523/JNEUROSCI.3027-04.2004.

Gonchar, Y, and A Burkhalter. 1999. "Connectivity of GABAergic Calretinin-Immunoreactive Neurons in Rat Primary Visual Cortex." *Cerebral Cortex* 9 (7): 683–96. doi:10.1093/cercor/9.7.683.

Gonchar, Yuri, Quanxin Wang, and Andreas Burkhalter. 2007. "Multiple Distinct Subtypes of GABAergic Neurons in Mouse Visual Cortex Identified by Triple Immunostaining." *Frontiers in Neuroanatomy* 1: 3. doi:10.3389/neuro.05.003.2007.

Gupta, Anirudh, Y Wang, and H Markram. 2000. "Organizing Principles for a Diversity of GABAergic Interneurons and Synapses in the Neocortex." *Science* 287 (5451): 273–78. doi:10.1126/science.287.5451.273.

Hires, Samuel Andrew, Diego A. Gutnisky, Jianing Yu, Daniel H. O'Connor, and Karel Svoboda. 2015. "Low-Noise Encoding of Active Touch by Layer 4 in the Somatosensory Cortex." *eLife* 4 (AUGUST2015): 1–18. doi:10.7554/eLife.06619.

Hooks, Bryan M, Tianyi Mao, Diego A Gutnisky, Naoki Yamawaki, Karel Svoboda, and Gordon M G Shepherd. 2013. "Organization of Cortical and Thalamic Input to Pyramidal Neurons in Mouse Motor Cortex." *Journal of Neuroscience* 33 (2): 748–60. doi:10.1523/JNEUROSCI.4338-12.2013.

Huang, Z. Josh. 2014. "Toward a Genetic Dissection of Cortical Circuits in the Mouse." *Neuron*. doi:10.1016/j.neuron.2014.08.041.

Ikrar, Taruna, Nicholas D. Olivas, Yulin Shi, and Xiangmin Xu. 2011. "Mapping Inhibitory Neuronal Circuits by Laser Scanning Photostimulation." *Journal of Visualized Experiments*, no. 56: 5–9. doi:10.3791/3109.

Insel, Thomas R, and Bruce N Cuthbert. 2015. "Brain Disorders? Precisely." *Science* 348: 499–500. doi:10.1126/science.aab2358.

Insel, Thomas, Bruce Cuthbert, Marjorie Garvey, Robert Heinssen, Daniel S Pine, Kevin Quinn, Charles Sanislow, and Philip Wang. 2010. "Research Domain Criteria (RDoC): Toward a New Classification Framework for Research on Mental Disorders." *The American Journal of Psychiatry* 167 (7): 748–51. doi:10.1176/appi.ajp.2010.09091379.

Jiang, Xiaolong, Shan Shen, Cathryn R. Cadwell, Philipp Berens, Fabian Sinz, Alexander S. Ecker, Saumil Patel, and Andreas S. Tolias. 2015. "Principles of Connectivity among Morphologically Defined Cell Types in Adult Neocortex." *Science* 350 (6264): aac9462–aac9462. doi:10.1126/science.aac9462.

Karnani, Mahesh M., Jesse Jackson, Inbal Ayzenshtat, Jason Tucciarone, Kasra Manoocheri, William G. Snider, and Rafael Yuste. 2016. "Cooperative Subnetworks of Molecularly Similar Interneurons in Mouse Neocortex." *Neuron* 90 (1). Elsevier Inc.: 86–100. doi:10.1016/j.neuron.2016.02.037.

Katz, Lawrence C, and M B Dalva. 1994. "Scanning Laser Photostimulation: A New Approach for Analyzing Brain Circuits." *Journal of Neuroscience Methods* 54 (2): 205–18. doi:10.1016/0165-0270(94)90194-5.

Katz, Lawrence C, and M B Dalva. 1990. "VIP Neurons in the Cerebral Cortex." *Trends in Pharmacological Sciences* 11 (6): 250–54. doi:10.1016/0165-6147(90)90253-5.

Kawaguchi, Yasuo, and Satoru Kondo. 2002. "Parvalbumin, Somatostatin and Cholecystokinin as Chemical Markers for Specific GABAergic Interneuron Types in the Rat Frontal Cortex." *Journal of Neurocytology*. doi:10.1023/A:1024126110356.

Kawaguchi, Yasuo, and Yoshiyuki Kubota. 1997. "GABAergic Cell Subtypes and Their Synaptic Connections in Rat Frontal Cortex." *Cerebral Cortex* 7 (6): 476–86. doi:10.1093/cercor/7.6.476.

Kim, Euiseok J., Ashley L. Juavinett, Espoir M. Kyubwa, Matthew W. Jacobs, and Edward M. Callaway. 2015. "Three Types of Cortical Layer 5 Neurons That Differ in Brain-Wide Connectivity and Function." *Neuron* 88 (6): 1253–67. doi:10.1016/j.neuron.2015.11.002.

Kozak, Michael J, and Bruce N Cuthbert. 2016. "The NIMH Research Domain Criteria Initiative: Background, Issues, and Pragmatics." *Psychophysiology* 53: 286–97. doi:10.1111/psyp.12518.

Krishnamurthy, Pradeep, Gilad Silberberg, and Anders Lansner. 2012. "A Cortical Attractor Network with Martinotti Cells Driven by Facilitating Synapses." *PLoS ONE* 7 (4). doi:10.1371/journal.pone.0030752.

Kubota, Yoshiyuki. 2014. "Untangling GABAergic Wiring in the Cortical Microcircuit." *Current Opinion in Neurobiology* 26. Elsevier Ltd: 7–14. doi:10.1016/j.conb.2013.10.003.

Lee, A. Moses, Jennifer L. Hoy, Antonello Bonci, Linda Wilbrecht, Michael P. Stryker, and Cristopher M. Niell. 2014. "Identification of a Brainstem Circuit Regulating Visual Cortical State in Parallel with Locomotion." *Neuron* 83 (2): 455–66. doi:10.1016/j.neuron.2014.06.031.

Lee, Charles C, Ying-Wan Lam, Kazuo Imaizumi, and S Murray Sherman. 2013. "Laser-Scanning Photostimulation of Optogenetically Targeted Forebrain Circuits." *Journal of Visualized Experiments : JoVE*, no. 82: 50915. doi:10.3791/50915.

Lee, S, J Hjerling-Leffler, E Zagha, G Fishell, and B Rudy. 2010. "The Largest Group of Superficial Neocortical GABAergic Interneurons Expresses Ionotropic Serotonin Receptors." *J Neurosci* 30 (50): 16796–808. doi:10.1523/JNEUROSCI.1869-10.2010.

Lee, Soohyun, Illya Kruglikov, Z. Josh Huang, Gord Fishell, and Bernardo Rudy. 2013. "A Disinhibitory Circuit Mediates Motor Integration in the Somatosensory Cortex." *Nature Neuroscience* 16 (11): 1662–70. doi:10.1038/nn.3544.

Lee, Wei-chung Allen, Vincent Bonin, Michael Reed, Brett J Graham, and Greg Hood. 2016. "Anatomy and Function of an Excitatory Network in the Visual Cortex." *Nature*, no. Table 1. Nature Publishing Group: 1–18. doi:10.1038/nature17192.

Lewis, David A. 2014. "Inhibitory Neurons in Human Cortical Circuits: Substrate for Cognitive Dysfunction in Schizophrenia." *Current Opinion in Neurobiology*. doi:10.1016/j.conb.2013.11.003.

Luo, Liqun, Edward M Callaway, and Karel Svoboda. 2008. "Genetic Dissection of Neural Circuits." *Neuron* 57 (5): 634–60. doi:10.1016/j.neuron.2008.01.002.

Ma, Yunyong, Hang Hu, Albert S Berrebi, Peter H Mathers, and Ariel Agmon. 2006. "Distinct Subtypes of Somatostatin-Containing Neocortical Interneurons

Revealed in Transgenic Mice." *The Journal of Neuroscience* 26 (19): 5069–82. doi:10.1523/JNEUROSCI.0661-06.2006.

Madisen, L, Mao, T, Koch, H, Zhuo, JM, Berenyi, A, Fujisawa, S, Hsu, YWA, Garcia, AJ, Gu, X, Zanella, S, Kidney, J, Gu, H, Mao, Y, Hooks, BM, Boyden, ES, Buzsáki, G, Ramirez, JM, Jones, AR, Svoboda, K, Han, X, Turner, EE & Zeng, H 2012. "A Toolbox of Cre-Dependent Optogenetic Transgenic Mice for Light-Induced Activation and Silencing." *Nature Neuroscience* 15 (5): 793–802. doi:10.1038/nn.3078.

Magistretti, Pierre J, J H Morrison, W J Shoemaker, V Sapin, and F E Bloom. 1981. "Vasoactive Intestinal Polypeptide Induces Glycogenolysis in Mouse Cortical Slices: A Possible Regulatory Mechanism for the Local Control of Energy Metabolism." *Proceedings of the National Academy of Sciences of the United States of America* 78 (10): 6535–39. doi:10.1073/pnas.78.10.6535.

Magistretti, Pierre J. 1986. "Intercellular Communication Mediated by VIP in the Cerebral Cortex." *Peptides* 7 (SUPPL. 1): 169–73. doi:10.1016/0196-9781(86)90181-6.

Meskenaite, V. 1997. "Calreatinin-Immunoreactive Local Circuit Neurons in Area 17 of the Cynomolgus Monkey, Macaca Fascicularis." *J Comp Neurol* 379 (1): 113–32.

Miyoshi, G., Jens Hjerling-Leffler, T. Karayannis, V. H. Sousa, S. J. B. Butt, J. Battiste, J. E. Johnson, R. P. Machold, and G. Fishell. 2010. "Genetic Fate Mapping Reveals That the Caudal Ganglionic Eminence Produces a Large and Diverse Population of Superficial Cortical Interneurons." *Journal of Neuroscience* 30 (5): 1582–94. doi:10.1523/JNEUROSCI.4515-09.2010.

Moore, A K, and M Wehr. 2013. "Parvalbumin-Expressing Inhibitory Interneurons in Auditory Cortex Are Well-Tuned for Frequency." *Journal of Neuroscience* 33 (34): 13713–23. doi:10.1523/JNEUROSCI.0663-13.2013.

Niell, Cristopher M., and Michael P. Stryker. 2010. "Modulation of Visual Responses by Behavioral State in Mouse Visual Cortex." *Neuron* 65 (4). Elsevier Ltd: 472–79. doi:10.1016/j.neuron.2010.01.033.

Nienborg, Hendrikje, Andrea Hasenstaub, Ian Nauhaus, Hiroki Taniguchi, Z Josh Huang, and Edward M Callaway. 2013. "Contrast Dependence and Differential Contributions from Somatostatin- and Parvalbumin-Expressing Neurons to Spatial Integration in Mouse V1." *The Journal of Neuroscience : The Official Journal of the Society for Neuroscience* 33 (27): 11145–54. doi:10.1523/JNEUROSCI.5320-12.2013.

Oliva, a a, M Jiang, T Lam, K L Smith, and J W Swann. 2000. "Novel Hippocampal Interneuronal Subtypes Identified Using Transgenic Mice That Express Green Fluorescent Protein in GABAergic Interneurons." *The Journal of Neuroscience : The Official Journal of the Society for Neuroscience* 20 (9): 3354–68. doi:0270-6474/00/203354-15$15.00/0.

Peters, Andrew J, Simon X Chen, and Takaki Komiyama. 2014. "Emergence of Reproducible Spatiotemporal Activity during Motor Learning." *Nature* 510 (7504). Nature Publishing Group: 263–67. doi:10.1038/nature13235.

Petreanu, Leopoldo, Tianyi Mao, Scott M Sternson, and K Svoboda. 2009. "The Subcellular Organization of Neocortical Excitatory Connections." *Nature* 457 (7233). Nature Publishing Group: 1142–45. doi:10.1038/nature07709.

Pfeffer, Carsten K, Mingshan Xue, Miao He, Z. Josh Huang, and Massimo Scanziani. 2013. "Inhibition of Inhibition in Visual Cortex: The Logic of Connections between Molecularly Distinct Interneurons." *Nature Neuroscience*. doi:10.1038/nn.3446.

Pi, Hyun-Jae, Balázs Hangya, Duda Kvitsiani, Joshua I Sanders, Z Josh Huang, and Adam Kepecs. 2013a. "Cortical Interneurons That Specialize in Disinhibitory Control." *Nature* 503 (7477): 521–24. doi:10.1038/nature12676.

Pi, Hyun-Jae, Balázs Hangya, Duda Kvitsiani, Joshua I Sanders, Z. Josh Huang, and Adam Kepecs. 2013b. "Cortical Interneurons That Specialize in Disinhibitory Control." *Nature* 503 (7477): 521–24. doi:10.1038/nature12676.

Pinto, L, M J Goard, D Estandian, M Xu, A C Kwan, S H Lee, T C Harrison, G Feng, and Y Dan. 2013. "Fast Modulation of Visual Perception by Basal Forebrain Cholinergic Neurons." *Nat Neurosci* 16 (12): 1857–63. doi:10.1038/nn.3552\rnn.3552 [pii].

Porter, James T., Bruno Cauli, Jochen F. Staiger, Bertrand Lambolez, Jean Rossier, and Etienne Audinat. 1998. "Properties of Bipolar VIPergic Interneurons and Their Excitation by Pyramidal Neurons in the Rat Neocortex." *European Journal of Neuroscience* 10 (12): 3617–28. doi:10.1046/j.1460-9568.1998.00367.x.

Prönneke, Alvar, Bianca Scheuer, Robin J Wagener, Martin Möck, Mirko Witte, and Jochen F Staiger. 2015. "Characterizing VIP Neurons in the Barrel Cortex of VIPcre/tdTomato Mice Reveals Layer-Specific Differences." *Cerebral Cortex* 25 (12): 4854–68. doi:10.1093/cercor/bhv202.

Reynolds, John H., and David J. Heeger. 2009. "The Normalization Model of Attention." *Neuron*. doi:10.1016/j.neuron.2009.01.002.

Rudy, Bernardo, Gordon Fishell, SooHyun Lee, and Jens Hjerling-Leffler. 2011. "Three Groups of Interneurons Account for Nearly 100% of Neocortical GABAergic Neurons." *Developmental Neurobiology* 71 (1): 45–61. doi:10.1002/dneu.20853.

Saito, Yasuhiko, Tomonori Takazawa, and Seiji Ozawa. 2008. "Relationship between Afterhyperpolarization Profiles and the Regularity of Spontaneous Firings in Rat Medial Vestibular Nucleus Neurons." *European Journal of Neuroscience* 28 (2): 288–98. doi:10.1111/j.1460-9568.2008.06338.x.

Shepherd, Gordon M G, Thomas A. Pologruto, and Karel Svoboda. 2003. "Circuit Analysis of Experience-Dependent Plasticity in the Developing Rat Barrel Cortex." *Neuron* 38 (2): 277–89. doi:10.1016/S0896-6273(03)00152-1.

Shinomoto, Shigeru, Keiji Miura, and Shinsuke Koyama. 2005. "A Measure of Local Variation of Inter-Spike Intervals." *BioSystems* 79 (1-3 SPEC. ISS.): 67–72. doi:10.1016/j.biosystems.2004.09.023.

Shinomoto, Shigeru, Keisetsu Shima, and Jun Tanji. 2003. "Differences in Spiking Patterns among Cortical Neurons." *Neural Computation* 15 (12): 2823–42. doi:10.1162/089976603322518759.

Shinomoto, Shigeru, Youichi Miyazaki, Hiroshi Tamura, and Ichiro Fujita. 2005. "Regional and Laminar Differences in in Vivo Firing Patterns of Primate Cortical Neurons." *Journal of Neurophysiology* 94 (March 2005): 567–75. doi:10.1152/jn.00896.2004.

Silberberg, Gilad, and Henry Markram. 2007. "Disynaptic Inhibition between Neocortical Pyramidal Cells Mediated by Martinotti Cells." *Neuron* 53 (5): 735–46. doi:10.1016/j.neuron.2007.02.012.

Suter, Benjamin. 2010. "Ephus: Multipurpose Data Acquisition Software for Neuroscience Experiments." *Frontiers in Neural Circuits* 4 (August): 1–12. doi:10.3389/fncir.2010.00100.

Tamamaki, Nobuaki, Yuchio Yanagawa, Ryohei Tomioka, Jun Ichi Miyazaki, Kunihiko Obata, and Takeshi Kaneko. 2003. "Green Fluorescent Protein Expression and Colocalization with Calretinin, Parvalbumin, and Somatostatin in the GAD67-GFP Knock-In Mouse." *Journal of Comparative Neurology* 467 (1): 60–79. doi:10.1002/cne.10905.

Taniguchi, H., He, M., Wu, P., Kim, S., Paik, R., Sugino, K., Kvitsani, D., Fu, Y., Lu, J., Lin, Y., Miyoshi, G., Shima, Y., Fishell, G., Nelson, S. B., Huang, Z. J. 2011. "A Resource of Cre Driver Lines for Genetic Targeting of GABAergic Neurons in Cerebral Cortex." *Neuron* 71 (6): 995–1013.

doi:10.1016/j.neuron.2011.07.026.

Taniguchi, Hiroki. 2014. "Genetic Dissection of GABAergic Neural Circuits in Mouse Neocortex." *Frontiers in Cellular Neuroscience* 8 (January): 8. doi:10.3389/fncel.2014.00008.

Tasic B, Menon V, Nguyen TN, Kim TK, Jarsky T, Yao Z, Levi B, Gray LT, Sorensen SA, Dolbeare T, Bertagnolli D, Goldy J, Shapovalova N, Parry S, Lee C, Smith K, Bernard A, Madisen L, Sunkin SM, Hawrylycz M, Koch C, Zeng H. 2016. "Adult Mouse Cortical Cell Taxonomy Revealed by Single Cell Transcriptomics." *Nature Neuroscience* advance on (January): 1–37. doi:10.1038/nn.4216.

Wall, Nicholas R., Mauricio De La Parra, Jordan M. Sorokin, Hiroki Taniguchi, Z. Josh Huang, and Edward M. Callaway. 2016. "Brain-Wide Maps of Synaptic Input to Cortical Interneurons." *The Journal of Neuroscience* 36 (14): 4000–4009. doi:10.1523/jneurosci.3967-15.2016.

Wang, Yun, Maria Toledo-Rodriguez, Anirudh Gupta, Caizhi Wu, Gilad Silberberg, Junyi Luo, and Henry Markram. 2004. "Anatomical, Physiological and Molecular Properties of Martinotti Cells in the Somatosensory Cortex of the Juvenile Rat." *The Journal of Physiology* 561 (Pt 1): 65–90. doi:10.1113/jphysiol.2004.073353.

Wickersham, Ian R, Stefan Finke, Karl-Klaus Conzelmann, and Edward M Callaway. 2007. "Retrograde Neuronal Tracing with a Deletion-Mutant Rabies Virus." *Nature Methods* 4 (1): 47–49. doi:10.1038/nmeth999.

Wilson, Nathan R, Caroline A Runyan, Forea L Wang, and Mriganka Sur. 2012. "Division and Subtraction by Distinct Cortical Inhibitory Networks in Vivo." *Nature* 488 (7411): 343–48. doi:10.1038/nature11347.

Xu, Han, Hyo Young Jeong, Robin Tremblay, and Bernardo Rudy. 2013. "Neocortical Somatostatin-Expressing GABAergic Interneurons Disinhibit the Thalamorecipient Layer 4." *Neuron* 77 (1). Elsevier: 155–67. doi:10.1016/j.neuron.2012.11.004.

Xu, Xiangmin, Keith D. Roby, and Edward M. Callaway. 2006. "Mouse Cortical Inhibitory Neuron Type That Coexpresses Somatostatin and Calretinin." *Journal of Comparative Neurology* 499 (1): 144–60. doi:10.1002/cne.21101.

Xu, Xiangmin, Keith D. Roby, and Edward M. Callaway.. 2010. "Immunochemical Characterization of Inhibitory Mouse Cortical Neurons: Three Chemically Distinct Classes of Inhibitory Cells." *Journal of Comparative Neurology* 518 (3): 389–404. doi:10.1002/cne.22229.

Yoshimura, Yumiko, and Edward M Callaway. 2005. "Fine-Scale Specificity of Cortical Networks Depends on Inhibitory Cell Type and Connectivity." *Nature Neuroscience* 8 (11): 1552–59. doi:10.1038/nn1565.

Zhang, Siyu, Min Xu, Tsukasa Kamigaki, Johnny Phong Hoang Do, Wei-Cheng Chang, Sean Jenvay, Kazunari Miyamichi, Liqun Luo, and Yang Dan. 2014. "Selective Attention. Long-Range and Local Circuits for Top-down Modulation of Visual Cortex Processing." *Science* 345 (6197): 660–65. doi:10.1126/science.1254126.

Zikopoulos, Basilis, and Helen Barbas. 2013. "Altered Neural Connectivity in Excitatory and Inhibitory Cortical Circuits in Autism." *Frontiers in Human Neuroscience* 7 (September): 609. doi:10.3389/fnhum.2013.00609.